Spectroscopy of Currents and Forces of Single-Atom and Single-Molecule Junctions

DISSERTATION

zur Erlangung des akademischen Grades

Doctor rerum naturalium (Dr. rer. nat.)

der Fakultät für Mathematik und Naturwissenschaften

der Technischen Universität Ilmenau

vorgelegt von

Jonathan Brand

1. Gutachter: Prof. Dr. J. Kröger
2. Gutachter: Prof. Dr. S. Krischok
3. Gutachter: Prof. Dr. S. Kirchner

Tag der Einreichung: 13.11.2018
Tag der wissenschaftlichen Aussprache: 18.12.2018

urn:nbn:de:gbv:ilm1-2018000543

Abstract

In the present work, a combined scanning tunneling and atomic force microscope is optimized in order to examine currents and forces at the single–atom and single–molecule level. Substantial improvement of the microscope performance is achieved, in particular by reducing the base temperature and mechanical as well as electromagnetic disturbances.

First, contacts to single C_{60} molecules on a superconducting Nb(110) surface are established in order to verify the stable operation of the microscope with an energy resolution which corresponds to the thermal limit. Spectroscopy during the formation of such contacts reveals the gradual evolution of the depression caused by the superconducting energy gap into a zero-bias peak. The experimental observations are rationalized in terms of increasing Andreev reflection probability with decreasing tip–sample distance. Careful evaluation of the differential and total conductances exposes subtle variations attributed to the atomic-scale geometry. Analysis within a multi-channel extension of the Blonder-Tinkham-Klapwijk model corroborates the orientation-dependence of the transmission coefficients of single C_{60} molecules. A novel approach to extract the minimum number of transmission channels is presented.

Additionally, the correct operation of the atomic force microscope is validated by reproducing the force evolution during the formation of C_{60}–C_{60} contacts. The impact of the externally applied bias voltage on the vertical force during the formation of single–molecule contacts is reported for the first time. Considering conventional forces and rigid electrodes indicates the occurrence of hitherto unexplored phenomena.

Finally, the temperature-dependence of the lateral force required for the manipulation of single atoms is quantified. The detection of forces with piconewton resolution highlights the performance of the optimized microscope. The insensitivity of the density of states at the Fermi level on the lateral threshold force for the manipulation of single atoms is unveiled by varying the phase of the substrate across the superconducting transition via temperature as well as magnetic field strength.

Zusammenfassung

In der vorliegenden Arbeit wird ein kombiniertes Rastertunnel- und Rasterkraftmikroskop optimiert, um Ströme und Kräfte in aus einzelnen Atomen und Molekülen bestehenden Kontakten zu untersuchen. Eine wesentliche Erhöhung der Leistungsfähigkeit des Mikroskops wird durch Reduzieren der Temperatur und mechanischer als auch elektromagnetischer Störungen erreicht.

Zunächst werden Kontakte zu einzelnen C_{60}-Molekülen auf einer supraleitenden Nb(110)-Oberfläche hergestellt, um den stabilen Betrieb des Mikroskops mit einer Energieauflösung zu verifizieren, welche der temperaturbedingten Grenze entspricht. Spektroskopische Messungen während der Bildung dieser Kontakte zeigen eine graduelle Zunahme des differentiellen Leitwerts innerhalb der supraleitenden Energielücke. Die experimentellen Beobachtungen verdeutlichen die Zunahme der Andreev-Reflexionswahrscheinlichkeit mit abnehmendem Abstand zwischen Probe und Spitze. Eine sorgfältige Auswertung der differentiellen und gesamten Leitwerte zeigt feine Unterschiede auf, welche auf die atomare Kontaktgeometrie zurückgeführt werden. Ein Vergleich der Resultate mit einer Erweiterung des Blonder-Tinkham-Klapwijk-Modells legt den Einfluss der Orientierungsabhängigkeit der Transmissionskoeffizienten einzelner C_{60}-Moleküle nahe. Es wird eine neuartige Methode vorgestellt, um die Mindestanzahl von Transportkanälen zu bestimmen.

Zusätzlich wird der fehlerfreie Betrieb des Rasterkraftmikroskops durch das Reproduzieren des Kraftverlaufs während der Bildung von C_{60}–C_{60}-Kontakten bestätigt. Der Einfluss der extern angelegten Spannung auf die während der Kontaktbildung herrschende vertikale Kraft wird zum ersten Mal berichtet. Die Berücksichtigung konventioneller Kräfte und starrer Elektroden weist auf das Auftreten bisher unerforschter Phänomene hin.

Schließlich wird die Temperaturabhängigkeit der zur Manipulation einzelner Atome benötigten lateralen Kraft quantifiziert. Die Erfassung von Kräften mit einer Auflösung im Piconewton-Bereich hebt die Leistungsfähigkeit des optimierten Mikroskops hervor. Die Unempfindlichkeit der zur Manipulation einzelner Atome benötigten lateralen Kraft von der Zustandsdichte am Fermi-Niveau wird gezeigt, indem das Substrat mittels Variation von Temperatur und magnetischer Feldstärke vom supraleitenden in den nichtsupraleitenden Zustand gebracht wird.

Contents

Chapter 1

Introduction

The invention of the scanning tunneling microscope (STM) in 1982 (ref. 1) and the atomic force microscope (AFM) in 1985 (ref. 2) revolutionized modern surface science. The capability of imaging structures, probing electronic effects, and measuring forces at the atomic scale rendered the examination of a vast number of previously inaccessible solid state phenomena and effects at unprecedented length scales possible. STM experiments revealed the presence of the Kondo effect at the single atom level[3,4]. Vibrational spectra of single molecules were directly obtained[5]. The edge state of monoatomic Fe chains on a superconducting Pb(110) surface was examined with STM[6] as well as AFM[7] and assigned to the presence of Majorana quasiparticle modes. The chemical structure of a single organic molecule[8], the charge state of single atoms[9], and the bond order of individual C–C bonds in polycyclic aromatic hydrocarbons as well as fullerenes[10] were measured. The force required to move a single atom on a metallic surface was quantitatively determined using AFM[11].

Employing the AFM enables the examination of the microscopic origins of phenomena related to friction. Previously, the directionality of friction of crystalline surfaces was examined[12–14]. The anisotropy present in the chemical structure of H-terminated Si(100) was shown to manifest itself as an anisotropic friction force[15]. The magnitude of friction was found to depend on the charge state of semiconducting Si(100)[16].

The impetus to the present thesis comprises the optimization of a combined ultrahigh-vacuum and low-temperature STM/AFM in order to explore electronic excitations and forces in single-atom and single-molecule contacts. **Chapter 2** gives a brief introduction to the theoretical framework required for understanding the experimental techniques as well as the analysis of the data. In **Chapter 3**, substantial improvements of the experimental setup are presented that were obtained by gradual optimization of the microscope performance during the course of the present work. The reduction of thermal as well as athermal noise levels are quantified. In order to examine the enhanced energy resolution, spectroscopic measurements of superconducting energy gaps were performed employing a Nb(110) surface. One benchmark of STM performance comprises the formation of stable contacts to single atoms or molecules. **Chapter 4** presents spectroscopic measurements during the gradual formation of contacts between a metallic tip, C_{60} molecules, and the surface of a superconducting Nb(110) crystal. The gradual transformation of the superconducting energy gap into a zero–bias peak was observed and rationalized in terms of increasing

Andreev reflection probability. The performance of the optimized STM setup is highlighted by the detection of subtle conductance variations caused by the orientation of the C_{60} molecule.

Initial AFM experiments are addressed in **Chapter 5**. In order to verify the correct operation of the force sensor, the previously reported[17] forces during the formation of contacts to single C_{60} molecules were recorded. The bias–dependence of the point of contact formation recently observed with an STM[18] was reproduced with the optimized AFM setup. Finally, the lateral force required to move single adatoms on three face-centered cubic metal surfaces is presented in **Chapter 6**. The temperature variation of the lateral force is quantified and reproduced in a simple microscopic model. Contrary to the variations observed across the superconducting transition temperature previously reported for N_2 films[19,20] and a lateral pendulum AFM[21], no impact of the superconducting phase on the lateral force necessary to move single atoms was observed.

Chapter 2

Theory

This chapter introduces the basic theoretical concepts used throughout the present thesis. First, the main assertions of the first microscopic theory of superconductivity developed by John Bardeen, Leon Cooper, and John Robert Schrieffer, generally referred to as BCS theory, are outlined. Then, the concepts relevant to scanning tunneling microscopy and spectroscopy are elucidated. Thereafter, the BTK formalism, named for Greg E. Blonder, Michael Tinkham, and Teun M. Klapwijk, which describes charge transport across the superconductor–normal metal interface for varying barrier heights, is recapitulated. Subsequently, the mathematics pertinent for non-contact atomic force microscopy are specified. Forces occurring in atomic scale junctions are briefly summarized. Finally, formulae applied to the statistical analysis throughout this thesis are presented.

2.1. Bardeen-Cooper-Schrieffer Theory

The BCS[22] ground state can be described by a set of coupled Schroedinger equations consisting of electron-like (u_k) and hole-like (v_k) wave functions with wave vector k.

$$\begin{pmatrix} \mathcal{H} & \Delta \\ \Delta^* & -\mathcal{H} \end{pmatrix} \begin{pmatrix} u_k \\ v_k \end{pmatrix} = E_k \begin{pmatrix} u_k \\ v_k \end{pmatrix} \tag{2.1}$$

The Hamiltonian $\mathcal{H}$ is expressed in terms of the reduced Planck constant $\hbar$, the particle mass m, and the chemical potential μ.

$$\mathcal{H} = -\frac{\hbar^2}{2m}\nabla^2 - \mu \tag{2.2}$$

The energy of single-particle excitations E_k is related to the free-electron energy ϵ_k (with respect to μ) and the energy gap Δ via $E_k^2 = \epsilon_k^2 + \Delta^2$.

During the transition from the normal-conducting ($\mathcal{N}$) into the superconducting ($\mathcal{S}$) state, number of quasiparticles has to be conserved. This condition can be expressed using the density of states in each state, $\varrho_{\mathcal{N},\mathcal{S}}$.

$$\int \varrho_{\mathcal{S}}(E_k)\, \mathrm{d}E_k = \int \varrho_{\mathcal{N}}(\epsilon_k)\, \mathrm{d}\epsilon_k = \int \varrho_{\mathcal{N}}(\epsilon_k)\, \frac{\mathrm{d}\epsilon_k}{\mathrm{d}E_k}\, \mathrm{d}E_k \tag{2.3}$$

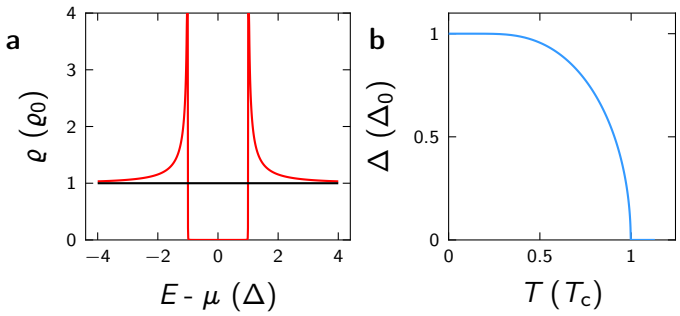

Figure 2.1. **a**, Density of states ϱ in the normal (black) and superconducting state (red) normalized to the normal-state DOS at the Fermi level ϱ_0 as a function of energy E. **b**, Temperate-dependence of the superconducting gap Δ according to BCS theory.

Usually, $\varrho_\mathcal{N}$ does not vary appreciably within $\mu \pm \Delta$ allowing the approximation[23] $\varrho_\mathcal{N}(\epsilon_k) \approx \varrho_\mathcal{N}(E_k) = \text{const.}$ which leads to the BCS expression[22] of the density of states

$$\varrho_\mathcal{S}(E_k) = \varrho_\mathcal{N}(\epsilon_k)\,\frac{\mathrm{d}\epsilon_k}{\mathrm{d}E_k} = \varrho_0 \frac{E_k}{\sqrt{E_k^2 - \Delta^2}} \tag{2.4}$$

using $\varrho_0 := \varrho_\mathcal{N}(\mu)$. $\varrho_\mathcal{S}$ exhibits an energy gap of width 2Δ and two singularities at $\pm\Delta$ (cf. Fig. 2.1 **a**). The temperature-dependence of Δ is given by the implicit integral equation[22]

$$\frac{1}{\varrho_0 \mathcal{V}} = \int_0^{\hbar\omega_\mathrm{D}} \frac{\mathrm{d}\epsilon_k}{\epsilon_k^2 + \Delta^2} \tanh\left(\frac{\beta}{2}\sqrt{\epsilon_k^2 + \Delta^2}\right) \tag{2.5}$$

as a function of the electron-electron interaction potential $\mathcal{V}$, Debye frequency ω_D, and Boltzmann factor $\beta = 1/\mathrm{k_B}T$ ($\mathrm{k_B}$ - Boltzmann constant, T - temperature). Eq. (2.5) can be solved numerically (cf. Fig. 2.1 **b**).

2.2. Scanning Tunneling Microscopy

The STM is a powerful tool that uses the quantum mechanical tunneling effect in order to probe conducting surfaces at the nanoscale. Tunneling occurs due to the exponentially decreasing but non-vanishing wave function inside a potential barrier. The tunneling current flowing from a probing tip t to the examined sample s is related to the single-electron tunneling matrix element $\mathcal{M}$ that is obtained from the Schroedinger equation[24], the occupied density of states of t and the empty density of states of s. The occupied density of states is obtained by multiplication of the density of states ϱ with the Fermi function $\mathfrak{f}(E,T) = \left[\exp\left(\frac{E-\mu}{\mathrm{k_B}T}\right) + 1\right]^{-1}$. $\mathfrak{f}$ is a function of the energy of the tunneling particle E, the chemical potential μ, and the temperature T. The application of an external bias voltage V between t and s leads to a modification of the first argument of $\mathfrak{f}_\mathrm{t}$ and ϱ_t, i.e., $E \to E + \mathrm{e}V$.

$$I_{\mathrm{t}\to\mathrm{s}}\,(V,T_\mathrm{t},T_\mathrm{s}) \;=\; \frac{2\pi e}{\hbar}\cdot\int_{-\infty}^{\infty}\mathrm{d}E\cdot|\mathcal{M}|^2\cdot\overbrace{\varrho_\mathrm{t}(E+\mathrm{e}V)\cdot\mathfrak{f}_\mathrm{t}(E+\mathrm{e}V,T_\mathrm{t})}^{\text{occupied density t}}\cdot\overbrace{\varrho_\mathrm{s}(E)\cdot\left[1-\mathfrak{f}_\mathrm{s}(E,T_\mathrm{s})\right]}^{\text{empty density s}} \tag{2.6}$$

Likewise, the current flowing from s to t is given as a function of the occupied ϱ_s and empty ϱ_t.

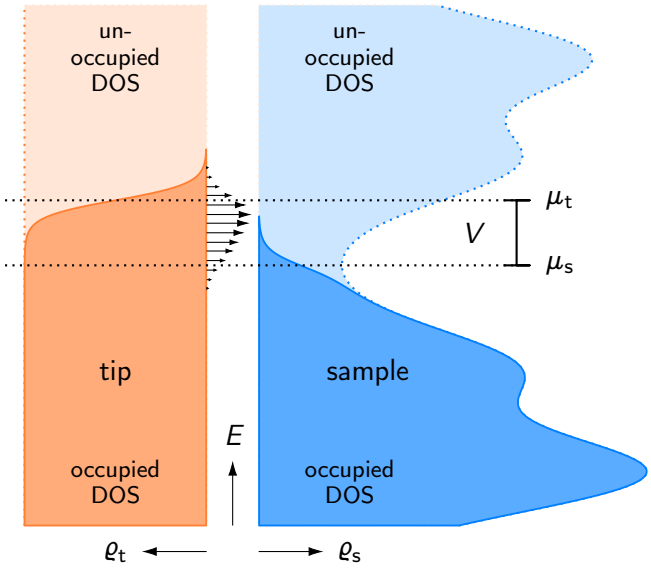

Figure 2.2. Visualization of the tunneling process between a tip with DOS ϱ_t = const (left, orange) and sample with ϱ_s (right, blue). The occupied DOS [dark orange (blue)] consists of ϱ_t (ϱ_s) multiplied with the Fermi function. The chemical potential of the tip, μ_t, is shifted by the externally applied bias V with respect to the chemical potential of the sample, μ_s. The energy-dependent net tunneling probability from occupied (dark orange/blue areas) to unoccupied states (light orange/blue areas) is indicated by the length of the horizontal arrows.

$$I_{s\to t}\,(V,T_t,T_s) \;=\; \frac{2\pi e}{\hbar}\cdot\int_{-\infty}^{\infty} \mathrm{d}E\cdot|\mathcal{M}|^2\cdot \overbrace{\varrho_t(E+eV)\cdot\Big[1-\mathfrak{f}_t(E+eV,T_t)\Big]}^{\text{empty density t}}\cdot \overbrace{\varrho_s(E)\cdot\mathfrak{f}_s(E,T_s)}^{\text{occupied density s}} \tag{2.7}$$

The total, net current I is given by the difference of $I_{t\to s}$ and $I_{s\to t}$ (cf. Fig. 2.2).

$$\begin{aligned} I\,(V,T_t,T_s) \;&=\; I_{t\to s} - I_{s\to t} \\ &=\; \frac{2\pi e}{\hbar}\cdot\int_{-\infty}^{\infty}\mathrm{d}E\cdot|\mathcal{M}|^2\cdot\varrho_s(E)\cdot\varrho_t(E+eV)\cdot\Big[\mathfrak{f}_t(E+eV,T_t)-\mathfrak{f}_s(E,T_s)\Big] \end{aligned} \tag{2.8}$$

Tunneling of an electron occupying a state n from a metal $\mathfrak{a}$ to a state m of a metal $\mathfrak{b}$ leads to a modification of the initial wave function Ψ_0 to Ψ_{mn}. The tunneling matrix element or transmission factor of this process can be obtained by integration over the area of $\mathfrak{a}$ (ref. 24).

$$\mathcal{M}_{mn} = \int_{\mathfrak{a}}\Big[\Psi_0^*\mathcal{H}\Psi_{mn} - \Psi_{mn}\mathcal{H}\Psi_0^*\Big]\mathrm{d}A \tag{2.9}$$

Within the Wentzel-Kramers-Brillouin approximation of slowly varying wave functions and a trapezoidal potential barrier, $\mathcal{M}$ is expressed as a function of the mean work function $\bar{\Phi} = (\Phi_t+\Phi_s)/2$ reflecting the exponentially decaying tunneling probability with increasing separation z (ref. 25,26) ($\Phi_{t,s}$ - work function of t and s, m - mass of the tunneling particle).

$$\mathcal{M}\propto\exp\left(-z\frac{2\sqrt{m}}{\hbar}\sqrt{\bar{\Phi}+eV/2-E}\right) \tag{2.10}$$

The STM consists of a metallic tip that is used to examine a conducting surface. Commonly, the tip is fixed to piezoelectric actuators that enable precise positioning in three dimensions (alternatively one or more piezoelectric actuators may be connected to the sample without altering

the principle of operation). The STM can be operated in imaging mode in order to gather topographic information of a surface. Here, a feedback mechanism is used to keep the tunneling current constant by continuously adjusting the tip height z (constant–current mode). The tip trajectory follows the contour of constant integrated density of states reflecting the surface topography. Alternatively, the tip height is fixed and the tunneling current as a function of tip position recorded (constant–height mode).

Moreover, spectroscopic information can be obtained in scanning tunneling spectroscopy (STS) mode. To this end, the current I is recorded as a function of applied bias voltage V at a specific location on the surface. According to eq. (2.8), I is dependent on the sample density of states ϱ_s. Tip materials with constant tip density of states $\varrho_t = \text{const}$ around the Fermi level are preferentially used. At low temperatures $T_{t,s} \to 0$, Fermi-Dirac functions are equal to heaviside functions

$$f_{(E,T=0)} = \Theta(-E) = \begin{cases} 0, & \text{for } E > 0 \\ 1, & \text{for } E \leqslant 0 \end{cases} \tag{2.11}$$

Consequently, the integral of eq. (2.8) is simplified from

$$\int_{-\infty}^{\infty} \mathrm{d}E \cdot \cdot \cdot \ (f_t - f_s) \qquad \text{to} \qquad \int_0^{eV} \mathrm{d}E \cdot \cdot \cdot \tag{2.12}$$

For low voltages, i.e., $eV \ll \bar{\Phi}$, $\mathcal{M}$ is constant[24,27]. Since work functions of metals exceed 1 eV, this condition is satisfied for tunneling experiments studying superconducting energy gaps that are of the order 1 meV. Hence,

$$I_{(V)} \ \propto \ \int_0^{eV} \mathrm{d}E \cdot \varrho_s(E) \tag{2.13}$$

The differential conductance is then directly proportional to the density of states.

$$G^{\partial}_{(V,T=0)} \ \equiv \ \mathrm{d}I/\mathrm{d}V_{(V,T=0)} \ \propto \ \varrho_s(eV) \tag{2.14}$$

At finite temperature ($T > 0\,\mathrm{K}$) eq. (2.11) is not valid. Evaluating eq. (2.8) for $\varrho_t = \text{const}$ yields G^{∂} as a convolution of ϱ_s with the derivative of f_t. The latter is usually referred to as instrumental function χ_{th}.

$$G^{\partial}{}_{(V,T)} = \varrho_{s\,(eV)} \ * \ \chi_{th\,(V,T)} \tag{2.15}$$

$$\chi_{th\,(V,T)} = |\partial_V f_{(eV,T)}| = \frac{\frac{e}{k_B T} \exp\left(\frac{eV}{k_B T}\right)}{\left[\exp\left(\frac{eV}{k_B T}\right) + 1\right]^2} \tag{2.16}$$

Note, that the only relevant temperature in the case of $\varrho_t = \text{const}$ is the tip temperature, T_t. χ_{th} is shown in Fig. 2.3 **a** for $T = 6\,\mathrm{K}$. It represents a Gaussian of full width at half minimum (FWHM) of $3.53\,k_B T = 1.83\,\mathrm{meV}$. This temperature significantly broadens the BCS density of states consisting of a gap of half width $\Delta = 1.5\,\mathrm{meV}$ (Fig. 2.3 **b**).

For common metals and higher voltages $|V| \gtrsim 0.5\,\mathrm{V}$, the tunneling matrix element $\mathcal{M}$ is not energy-independent[28]. At 0 K, eq. (2.8) leads to

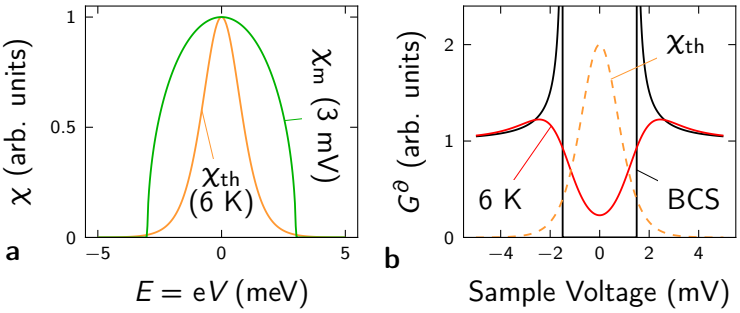

Figure 2.3. Broadening in STS. **a**, Instrumental function χ for thermal broadening at $T = 6\,\mathrm{K}$ (orange, duplicated in **b** [dashed]) and modulation broadening for amplitude $V_\mathrm{m} = 3\,\mathrm{mV}$ (green). **b**, Impact of thermal broadening at 6 K (red) on the zero-temperature G^∂ (black) of a BCS gap of width $\Delta = 1.5\,\mathrm{meV}$.

$$I_{(V)} \propto \int_0^{eV} \mathrm{d}E \cdot \varrho_\mathrm{s}(E) \cdot \mathcal{M}_{(E,eV)} \tag{2.17}$$

$$G^\partial \propto \varrho_\mathrm{s}(eV) \cdot \mathcal{M}_{(eV,eV)} + \int_0^{eV} \mathrm{d}E \cdot \varrho_\mathrm{s}(E) \cdot \partial_{eV}\mathcal{M}_{(E,eV)} \tag{2.18}$$

In order to reduce the impact of $\mathcal{M}$ and obtain a quantity that provides a better representation of ϱ_s than G^∂, Feenstra *et al.* proposed normalizing G^∂ by division with $G = I/V$ (ref. 29).

$$G^\partial / G = \frac{\varrho_\mathrm{s}(eV) + \int_0^{eV} \mathrm{d}E \cdot \varrho_\mathrm{s}(E) \cdot \dfrac{\partial_{eV}\mathcal{M}_{(E,eV)}}{\mathcal{M}_{(eV,eV)}}}{\dfrac{1}{eV} \cdot \int_0^{eV} \mathrm{d}E \cdot \varrho_\mathrm{s}(E) \cdot \dfrac{\mathcal{M}_{(E,eV)}}{\mathcal{M}_{(eV,eV)}}} \tag{2.19}$$

To first approximation, the exponential dependencies of $\mathcal{M}$ on z and V are canceled, since only fractions of $\mathcal{M}_{(E,eV)}$ and $\mathcal{M}_{(eV,eV)}$ appear. Hence, the denominator normalizes ϱ_s, whereas the second term introduces a "background" [29] term. Compared to alternative normalization methods[28,30–32], this approach does not require additional data, such as estimates of the work function difference and the actual tip–sample distance. The result of an exemplary normalization is presented in Fig. 2.4. Fig. 2.4 **a** show the arbitrary input ϱ_s, which serves as basis for the calculation of the differential conductance (Fig. 2.4 **b**) according to eq. (2.8). The normalized differential conductance is visualized in Fig. 2.4 **c**. One advantage of the normalization consists of the recovering of a peak for the feature at negative bias voltage, which is visible as shoulder in G^∂ data. Hence, a peak position can be assigned subsequent to the normalization. However, G^∂/G data yield a slight variation of the peak locations compared to the input ϱ_s. Specifically, the separation between the first peak at negative and positive voltages is systematically underestimated.

Lock-In Technique

Usually, the quantity of interest in STS is the density of states which is closely related to the differential conductance G^∂. G^∂ may be obtained by numerical derivation of I which, however, leads to the amplification of phase-incoherent noise. This drawback can be circumvented by employing the Lock-In technique[33–35]. A Lock-In amplifier modulates the applied bias voltage V_0 with an alternating voltage of amplitude V_m and frequency f_m.

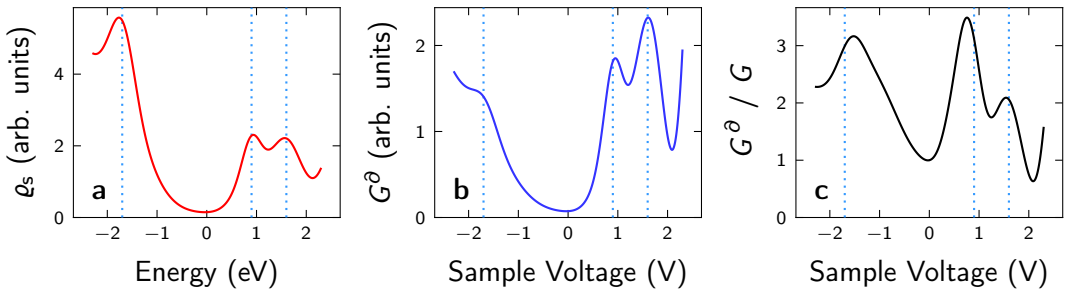

Figure 2.4. Visualization of the differential conductance normalization. **a**, Input ϱ_s, **b**, G^∂ calculated according to eq. (2.8), and **c**, normalized G^∂/G for an exemplary model system. Tunneling parameters are $T_s = T_t = 6\,\mathrm{K}$, $\bar{\Phi} = 5\,\mathrm{eV}$, $z = 0.5\,\mathrm{nm}$, and $m = 3\,m_e$ (m_e - free electron mass). ϱ_s was modeled by a superposition of Gaussian functions, centered at the vertical dashed lines.

$$V(t) = V_0 + V_m \sin(2\pi f_m t) \tag{2.20}$$

Consequently, an oscillating current response $I = I(V_0 + V_m \sin 2\pi f_m t)$ is generated with an amplitude that is proportional to V_m and the slope of I, i.e., $\mathrm{d}I/\mathrm{d}V = G^\partial$ (Fig. 2.5). The $\mathrm{d}I/\mathrm{d}V$ signal is given by the first order Fourier coefficient of I. This connection can be rationalized by the comparison of a Taylor and a Fourier expansion. The former and later are given as

$$I(V_0) \sim \sum_{i=0}^{\infty} \frac{\partial_V^{(i)} I(V_0)}{i!}(V - V_0)^i = I(V_0) + \partial_V I(V_0) \cdot V_m \sin(2\pi f_m t) + \mathcal{O}(V_0^2) \tag{2.21}$$

and

$$I(V) \sim \frac{b_0}{2} + \sum_{j=1}^{\infty} [a_j \sin(\mathrm{j}2\pi f_m t) + b_j \cos(\mathrm{j}2\pi f_m t)] \tag{2.22}$$

respectively. The current I is given by the zero-order Fourier coefficient b_0, while the first derivative $\mathrm{d}I/\mathrm{d}V \equiv G^\partial$ is proportional to a_1. The Lock-In amplifier uses homodyne detection that enables the determination of the Fourier coefficients by using the bias modulation $V_{AC} = V_m \sin(2\pi f_m t)$ as reference signal.

$$a_1(t) = \int_t^{t+\tau_i} I(\hat{t}) \sin(2\pi f_m \hat{t})\, \mathrm{d}\hat{t} \propto \int_t^{t+\tau_i} I(\hat{t})\, V_{AC}(\hat{t})\, \mathrm{d}\hat{t} \tag{2.23}$$

Figure 2.5. Operational principle of a Lock-In amplifier. An oscillating bias voltage $V = V_0 + V_m \sin 2\pi f_m t$ (green) entails an oscillating current I (blue). Black horizontal bars depict $2V_m$.

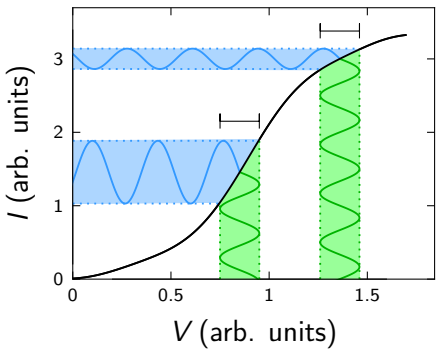

The bias modulation causes additional broadening. The measured G^{∂} is represented by a convolution of the thermally broadened G^{∂} with the instrumental function χ_{m}.

$$G^{\partial}_{V_{\mathrm{m}}>0} = G^{\partial}_{V_{\mathrm{m}}=0} \; * \; \chi_{\mathrm{m}}(V_{\mathrm{m}}) \tag{2.24}$$

$$\chi_{\mathrm{m}} = \begin{cases} \dfrac{2}{\pi V_{\mathrm{m}}} \sqrt{1 - \dfrac{V^2}{V_{\mathrm{m}}^2}}, & \text{for } |V| \leq V_{\mathrm{m}} \\ 0, & \text{for } |V| > V_{\mathrm{m}} \end{cases} \tag{2.25}$$

$\chi_{\mathrm{m}}\,(\mathrm{V})$ represents a semi-ellipse of FHWM $1.73\,V_{\mathrm{m}}$ (green curve Fig. 2.3 **a**).

2.3. Blonder-Tinkham-Klapwijk Theory

Tunneling into a superconductor at large tip–sample separations allows a measurement of the superconducting density of states featuring an energy gap around $V = 0$ since electrons incident from the normal metal $\mathcal{N}$ cannot enter the superconductor $\mathcal{S}$ at voltages $|eV| < \Delta$. When $\mathcal{N}$ and $\mathcal{S}$ are in close proximity, electrons do not have to be reflected back into $\mathcal{N}$ but may be retro-reflected as holes (cf. Fig. 2.6). Charge and particle number are conserved since the process is accompanied by the addition of a Cooper pair to the superconducting condensate. The effect was first described by Andreev [36] and is commonly referred to as Andreev reflection (AR). In total, four processes may occur at the $\mathcal{NS}$ interface that can be characterized according to their modification of the velocity direction parallel ($\hat{v}_{\parallel}$) and perpendicular ($\hat{v}_{\perp}$) to the interface:

symbol	description	$\hat{v}_{\parallel}$	$\hat{v}_{\perp}$
$\mathcal{A}$	normal (specular) reflection as an electron	$\hat{v}_{\parallel} \to \hat{v}_{\parallel}$	$\hat{v}_{\perp} \to -\hat{v}_{\perp}$
$\mathcal{B}$	Andreev (retro) reflection as a hole	$\hat{v}_{\parallel} \to -\hat{v}_{\parallel}$	$\hat{v}_{\perp} \to -\hat{v}_{\perp}$
$\mathcal{C}$	transmission as electron-like quasiparticle	$\hat{v}_{\parallel} \to \hat{v}_{\parallel}$	$\hat{v}_{\perp} \to \hat{v}_{\perp}$
$\mathcal{D}$	transmission as hole-like quasiparticle	$\hat{v}_{\parallel} \to -\hat{v}_{\parallel}$	$\hat{v}_{\perp} \to \hat{v}_{\perp}$

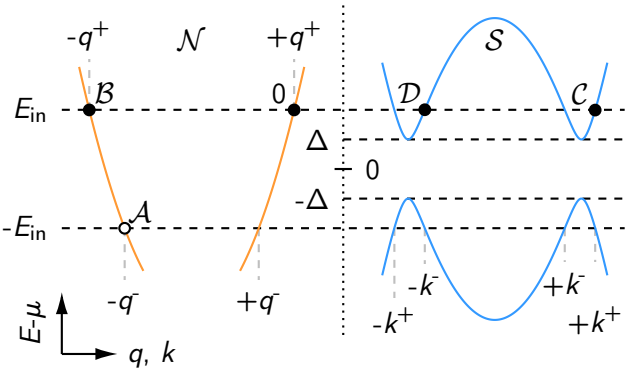

Figure 2.6. Illustration of Andreev reflection in k-space. An electron (0) incident from the normal conductor $\mathcal{N}$ with wave vector q^+ and energy E_{in} can either be reflected ($\mathcal{B}$, $-q^+$), retro-reflected as a hole ($\mathcal{A}$, $-q^-$), or injected into the superconductor $\mathcal{S}$ as electron-like ($\mathcal{C}$, k^+) or hole-like quasiparticle ($\mathcal{D}$, $-k^-$). Andreev reflection ($\mathcal{A}$) is accompanied by the creation of a Cooper pair in $\mathcal{S}$ at μ. Orange (blue) curves represent the dispersion relation in the normal (superconducting) state.

As a consequence of AR, G^{∂} is altered since current may flow at voltages within the energy gap. The corresponding theoretical framework was developed by Blonder, Tinkham, and Klapwijk[37] and is commonly referred to as BTK theory. Here, the BCS Hamiltonian of eq. (2.2) is extended by a delta potential of height $\mathscr{H}$, i.e., $\mathcal{V}_{(z)} = \mathscr{H} \cdot \delta(z)$, controlling the probability of AR.

$$\mathcal{H} = -\frac{\hbar^2}{2m}\nabla^2 - \mu + \mathcal{V}_{(z)} \tag{2.26}$$

BTK introduces a dimensionless barrier strength Z, replacing $\mathscr{H} = \hbar v_\mathrm{F} \cdot Z$ (Fermi velocity v_F). The BTK ansatz considers four quasiparticle wave functions in $\mathcal{S}$ with coefficients u_0 and v_0 featuring electron- and hole-like character, respectively.

$$\psi_{\pm k^+} = \begin{bmatrix} u_0 \\ v_0 \end{bmatrix} \exp\left(\pm \mathrm{i} k^+ x\right) \tag{2.27}$$

$$\psi_{\pm k^-} = \begin{bmatrix} u_0 \\ v_0 \end{bmatrix} \exp\left(\pm \mathrm{i} k^- x\right) \tag{2.28}$$

In the following, $\pm k^\pm$ denote the wave vectors corresponding to the energy of the electron incident from $\mathcal{N}$ (cf. Fig. 2.6). The incoming electron wave (ψ_in) with wave vector q^+ leads to reflected (ψ_refl) and transmitted (ψ_trans) waves.

$$\psi_\mathrm{in} = \begin{bmatrix} 1 \\ 0 \end{bmatrix} \exp\left(\mathrm{i} q^+ x\right) \tag{2.29}$$

$$\psi_\mathrm{refl} = a \begin{bmatrix} 0 \\ 1 \end{bmatrix} \exp\left(\mathrm{i} q^- x\right) \;+\; b \begin{bmatrix} 1 \\ 0 \end{bmatrix} \exp\left(-\mathrm{i} q^+ x\right) \tag{2.30}$$

$$\psi_\mathrm{trans} = c \begin{bmatrix} u_0 \\ v_0 \end{bmatrix} \exp\left(\mathrm{i} k^+ x\right) \;+\; d \begin{bmatrix} u_0 \\ v_0 \end{bmatrix} \exp\left(-\mathrm{i} k^- x\right) \tag{2.31}$$

$$\hbar k^\pm = \sqrt{2m}\sqrt{\mu \pm \sqrt{E_k^2 - \Delta^2}} \qquad\qquad \hbar q^\pm = \sqrt{2m}\sqrt{\mu \pm E_k} \tag{2.32}$$

Matching value and slope of the wave functions at the interface yields analytical formulae for a, b, c, and d that enable the calculation of the BTK coefficients $\mathcal{A} = a^* a$, $\mathcal{B} = b^* b$, $\mathcal{C} = c^* c$, and $\mathcal{D} = d^* d$ as functions of $E_k = \mathrm{e}V$, Δ, and Z according to eqs. (2.33) to (2.35) and Tab. 2.1.

$$u_0^2 = \frac{1}{2} + \frac{1}{2}\sqrt{\frac{E_k^2 - \Delta^2}{E_k^2}} \tag{2.33}$$

$$v_0^2 = 1 - u_0^2 \tag{2.34}$$

$$\gamma^2 = \left[u_0^2 + Z^2 \cdot \left(u_0^2 - v_0^2\right)\right]^2 \tag{2.35}$$

The differential conductance across the NS interface at 0 K is given by

$$G^{\partial}_{\mathrm{BTK}(V,\Delta,Z)} \;=\; 2\,\varrho_0\,\mathrm{e}\,v_\mathrm{F}\,\mathscr{A} \;\cdot\; [1 + \mathcal{A}_{(V,\Delta,Z)} - \mathcal{B}_{(V,\Delta,Z)}] \tag{2.36}$$

	$\mathcal{A}$	$\mathcal{B}$
$\lvert E_k\rvert \leqslant \Delta$	$\dfrac{\Delta^2}{E_k^2 + (\Delta^2 - E_k^2)\cdot(1+2\cdot Z^2)^2}$	$1-\mathcal{A}$
$\lvert E\rvert > \Delta$	$\dfrac{u_0^2 v_0^2}{\gamma^2}$	$\dfrac{(u_0^2 - v_0^2)^2 \cdot Z^2 \cdot (1+Z^2)}{\gamma^2}$

Table 2.1. Analytic expressions for the BTK coefficients $\mathcal{A}$ and $\mathcal{B}$.

$G^{\partial}_{\mathrm{BTK}}$ depends linearly on the DOS at the Fermi level ϱ_0, the elementary charge e, the Fermi velocity v_F, the effective tunneling area $\mathcal{A}$, and a factor determined by BTK coefficients, $[1+\mathcal{A}-\mathcal{B}]$. The energy-dependence of the last factor in eq. (2.36) represents the variation of the tunneling probability caused by superconductivity. Without SC, i.e., $\Delta = 0$, no AR occurs ($\mathcal{A} = 0$) and G^{∂} is governed by the energy-independent reflection probability $\mathcal{B} = \text{const}$, yielding $G^{\partial} = \text{const}$. The transparency of the tunneling barrier τ can be obtained evaluating eq. (2.36) for either $\Delta = 0$ or $|eV| \gg \Delta$. Here, $u_0^2 = 1$, $v_0^2 = 0$, and $\gamma^2 = (1+Z^2)^2$, Thus, $\mathcal{A} \to 0$ and $\mathcal{B} = Z^2/(1+Z^2)$. τ is then given by the relation

$$\tau = 1 - \mathcal{B} = \left(1 + Z^2\right)^{-1} \tag{2.37}$$

For finite Δ but large tunneling barrier $Z \to \infty$, $\mathcal{A} \to 0$ and $\mathcal{B} \neq \text{const}$. The BCS progression of the density of states is recovered (bottom curve in Fig. 2.7 **a,b**). $G^{\partial} \propto 1 - \mathcal{B}$ signifies unity tunneling probability ("1") subtracted by the probability of ordinary reflection ("$-\mathcal{B}$"). For finite Z, G^{∂} is enhanced ("$+\mathcal{A}$") below and close to the energy gap due to the second electron transferred for each retro-reflected electron. For high transparency $\tau \to 1$ ($Z \to 0$), G^{∂} inside the gap $-\Delta \leq eV \leq \Delta$ amounts to twice the value at high bias $|eV| \gg \Delta$ representing the transfer

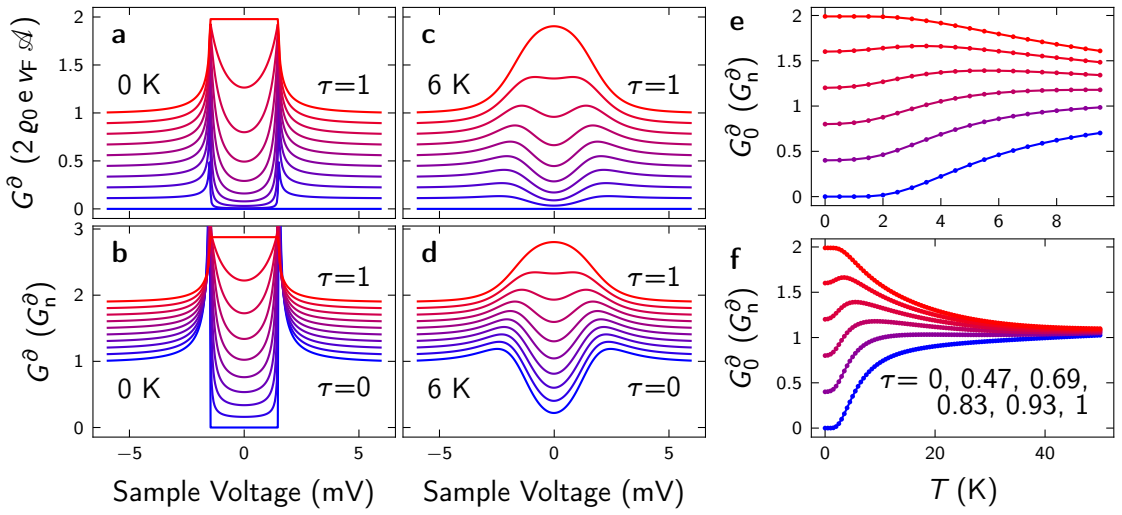

Figure 2.7. **a-d**, Differential conductance G^{∂} according to BTK theory at 0 K (**a,b**) and 6 K (**c,d**) for different BTK transparency values $0 \leq \tau \leq 1$ using $\Delta = 1.5$ meV. G^{∂} in **b,d** is normalized to G^{∂} in the normal state $G^{\partial}_{\mathrm{n}}$ and consecutively shifted upward. **e-f**, G^{∂} at $V = 0$ as a function of temperature T for (from bottom to top) $\tau = 0$, 0.47, 0.69, 0.83, and 1.

of two electrons for each incoming electron (top curve in Fig. 2.7 **a**). The impact of temperature is exhibited in Fig. 2.7 **c,d**. The exemplary temperature of 6 K leads to a filling inside the gap and the disappearance of the sharp coherence peaks for low τ. For $\tau \to 1$, the sharp edges at $\pm\Delta$ flatten leading to the development of a gaussian-like peak at zero bias. The effect of thermal broadening is visualized by the evolution of the differential conductance at zero bias G_0^∂ shown in Fig. 2.7 **e,f**. For $T \lesssim 2\,\mathrm{K}$, the 0 K values are retained while for increasing T G_0^∂ progressively approaches the value outside the gap $G_\mathrm{n}^\partial = G^\partial(|eV| \gg \Delta)$.

2.4. Atomic Force Microscopy

The atomic force microscope (AFM) shares the key components of the STM. The main difference consists of the addition of a flexible cantilever that enables force measurements. Two modes may be employed. First, the static deflection of the cantilever is a measure proportional to the force acting on the AFM tip attached to the end of the cantilever. This mode requires a force constant much lower than the interatomic force constant of the probe material. Typical force constants are of the order 0.01 to $5\,\mathrm{N\,m^{-1}}$ (ref. 38). Obtaining atomic resolution is a rather challenging task since low force constants entail the risk of a jump into contact at low distances leading to inelastic deformations and requiring a large-scale retraction of the tip.

In the dynamic (non-contact, nc) mode an external excitation is used to oscillate the cantilever in either amplitude-modulation (AM) or frequency-modulation (FM) mode. AM-AFM consists of a constant excitation frequency f and constant excitation amplitude. This technique has the disadvantages of low temporal sensitivity and the measured oscillation amplitude and phase exhibit a non-trivial relation to the forces acting on the tip. In a superior approach the cantilever is excited at constant oscillation amplitude and at its resonance frequency. Forces acting on the tip continuously modify the resonance frequency which serves as a measure of the interaction force.

Mathematical Description

The FM-AFM cantilever is commonly treated as a driven harmonic oscillator (HO) (cf. Fig. 2.11). The basic physics of a HO is captured by considering a body of inertial mass m that experiences a restoring force $-k_0 x$ opposite to x, the displacement from its equilibrium position. When a mass is suspended on a spring, k_0 represents the spring constant. External driving is incorporated via $F_\mathrm{ext}(t)$, which for FM-AFM comprises a periodic excitation force $F_\mathrm{ext}(t) = \hat{F}_\mathrm{ext} \cdot \cos(2\pi f t)$ with driving frequency f and amplitude $\hat{F}_\mathrm{ext}$. Newton's second law reads

$$m\ddot{x} = -k_0 x - 2m\gamma\dot{x} + F_\mathrm{ext} \tag{2.38}$$

An undamped HO has a resonance frequency $2\pi f_0 = \omega_0 = \sqrt{\frac{k_0}{m}}$. In real HOs, a friction or damping force $-2m\gamma\dot{x}$ opposes the motion leading to dissipation. The magnitude of the damping is characterized by the dimensionless quantity $\hat{Q}$, commonly termed quality factor. γ can be expressed as a function of $\hat{Q}$, i.e., $\gamma = \omega_0/(2\hat{Q})$. Damping reduces the resonance frequency.

$$\omega_0 \to \omega_0 \cdot \sqrt{1 - \gamma^2/4mk_0} \tag{2.39}$$

A nc-AFM cantilever in close proximity to a sample can be described by a mass connected to the z piezo with a spring k_0 and to the sample by a second spring k_{ts} (embodying the force acting between tip and sample, F_{ts}, cf. Fig. 2.11 **b**).

$$\begin{aligned} m\ddot{x} &= -k_0 x - k_{ts} x - 2m\gamma\dot{x} + F_{ext} \\ &= -(k_0 + k_{ts})x - 2m\gamma\dot{x} + F_{ext} \end{aligned} \tag{2.40}$$

A non-vanishing k_{ts} thus entails a modified (undamped) resonance frequency $\hat{\omega}_0$.

$$\hat{\omega}_0 = 2\pi\hat{f}_0 = \sqrt{\frac{k_0 + k_{ts}}{m}} \tag{2.41}$$

In nc-AFM, the quality factor Q is commonly defined as a frequency-to-width ratio using the FWHM Δf_{FWHM} obtained from amplitude-vs-frequency data.

$$Q := \frac{f_0}{\Delta f_{FWHM}} \tag{2.42}$$

A high quality oscillator ($Q \gg 1$) excited at a frequency f by a sinusoidal oscillation of amplitude A_{exc} via a spring k_0 causes a driving force of amplitude $\hat{F}_{ext} = k_0 \cdot A_{exc}$ and gives rise to an oscillation of amplitude A (ref. 38)

$$A = A_{exc} / \sqrt{(1 - f^2/f_0^2)^2 + f^2/(f_0^2\hat{Q}^2)} \tag{2.43}$$

and phase ϕ between excitation and response signal

$$\phi = \arctan\left(\frac{f}{\hat{Q} f_0 (1 - f^2/f_0^2)}\right) \tag{2.44}$$

A and ϕ as a function of excitation frequency f are depicted in Fig. 2.8 for different values of Q. The amplitude (FWHM) of A increases (decreases) linearly with Q. The slope of ϕ at f_0, $\partial_f \phi(f_0) = 2Q/f_0$, likewise increases linearly with Q. $\hat{Q}$ according to eq. (2.43) and Q as defined by eq. (2.42) differ by a factor of 1.73 (1.76 obtained from experimental data, cf. Fig. A.1).

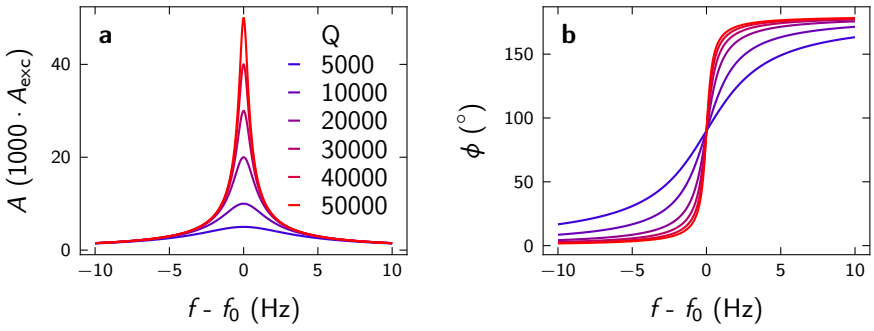

Figure 2.8. **a**, Amplitude A and **b**, phase ϕ as a function of excitation frequency f for a harmonic oscillator and varying quality factor Q.

A Taylor expansion of eq. (2.41) at f_0 using $\sqrt{1+x} \sim 1 + x/2$ allows a linear approximation of the shift of the resonance frequency, Δf.

$$\Delta f := \hat{f}_0 - f_0 = f_0 \frac{k_{ts}}{2k_0} \tag{2.45}$$

In the limit of zero oscillation amplitude, Hooke's law may be employed in order to directly obtain the tip–sample interaction force F_{ts} by integration of $k_{ts} = -\nabla F_{ts}$. For finite oscillation amplitudes this simple relation does not hold. For $\Delta f \ll f_0$ the frequency shift can be derived using the Hamilton-Jacobi method and calculated by integrating over one oscillation cycle[38–40].

$$\Delta f(z) = -\frac{f_0^2}{kA}\int_0^{1/f_0} \mathrm{d}t \cdot F_{ts}(z + A \cdot \cos\omega_0 t) \cdot \cos\omega_0 t \tag{2.46}$$

The result of the convolution of an arbitrary force (Fig. 2.9 **a**) is shown in Fig. 2.9 **b**. The impact of the oscillation is clearly visible progressively reducing the magnitude of the Δf minimum as well as shifting the z value at the minimum for increasing A. In order to recover the pristine, deconvoluted F_{ts} two methods may be applied. Gießibl used a discretization in order to rewrite eq. (2.46) in matrix form ("matrix method") and obtained F_{ts} by matrix inversion and multiplication with Δf (ref. 41). Sader and Jarvis employed a Laplace transformation and utilized properties of the Riemann-Liouville fractional integral in order to derive an analytical function ("Sader method")[42]. The results of deconvolution using algorithms developed on basis of the matrix and Sader method are shown in Fig. 2.9 **c,d**. Both curves resemble the input force, shown in black. Two main properties of the different approaches are pertinent for a practical application. The artificially added noise is more pronounced for the matrix method. The minimum force deviates less than 1 % for all amplitudes, whereas the Sader method systematically underestimates the force minimum by $\sim$ 5 % for amplitudes below 100 pm.

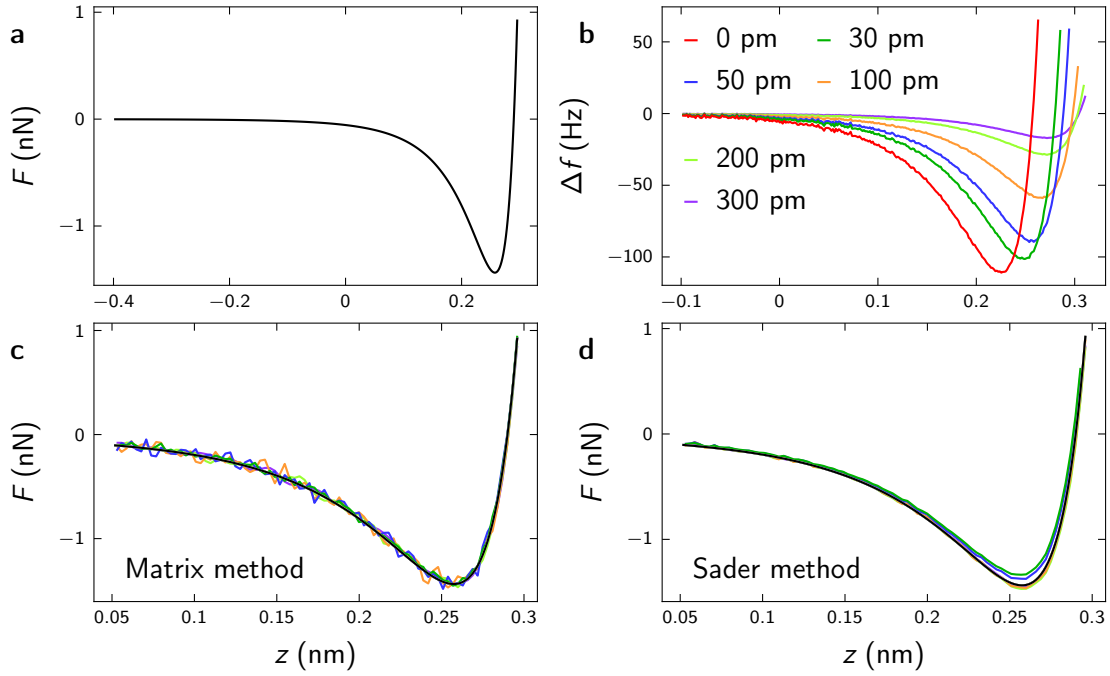

Figure 2.9. Evaluation of the force deconvolution algorithms. **a**, Exemplary input force (black). **b**, Convoluted frequency shift computed with the input force of **a** at different oscillation amplitudes A ranging from 30 pm (dark green) to 300 pm (violet) as indicated in the panel. Red denotes the zero-amplitude frequency shift without convolution. A random noise was added to Δf. **c,d**, Deconvolution of Δf of **b** using algorithms introduced by Gießibl[41] (**c**) and Sader and Jarvis[42] (**d**) as well as input force (black).

The current flowing during AFM measurements is likewise affected by the sensor oscillation. The impact of the oscillation amplitude on the measured, average current I_{avg} according to

$$I_{avg}(z) = \int_0^{1/f_0} \mathrm{d}t \; I(z + A \cdot \cos(2\pi f_0 t)) \tag{2.47}$$

is shown in Fig. 2.10 **a** for different amplitudes. Sader and Sugimoto used a similar approach to the Sader method[42] to obtain an analytical function for the deconvoluted current[43]. Deconvolution yields an error <3 % in semi-logarithmic representation (Fig. 2.10 **b**).

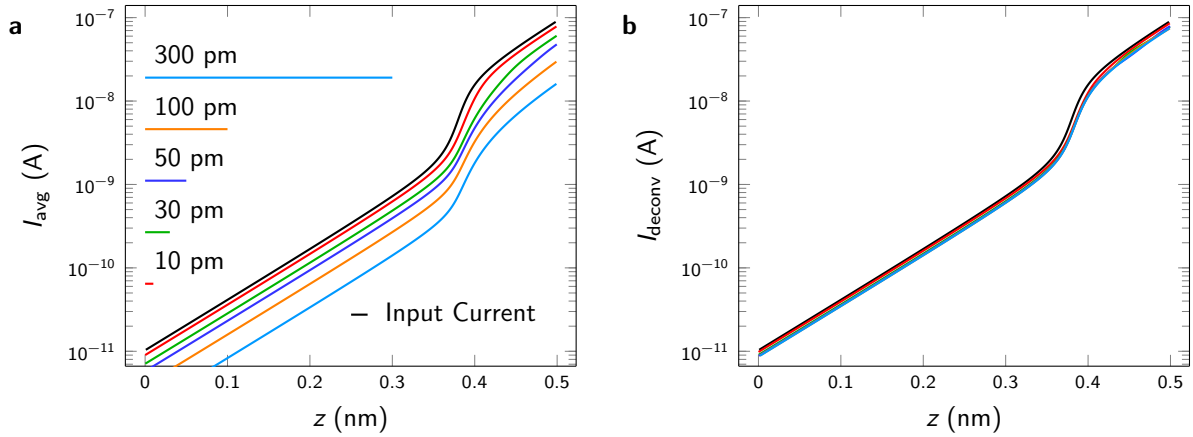

Figure 2.10. Evaluation of the current deconvolution algorithm. **a**, Arbitrary input current (black) and averaged current I_{avg} for different oscillation amplitudes indicated on the left. **b**, Deconvoluted current using the algorithm introduced by Sader and Sugimoto[43].

Quartz Tuning Forks as High-Resolution Force Sensors

The highest spatial as well as force resolution is obtained by employing quartz tuning forks (QTF)[38,44]. Quartz is a tetrahedral polymorph of silicon dioxide, SiO_2, and a piezoelectric material. The principle of a force sensor based on a quartz tuning fork is outlined in Fig. 2.11 **a**. One prong of the fork is glued to the tip holder and the second one oscillates freely. A metal tip attached to the end of the free prong is commonly connected via a small wire allowing the application of a bias voltage and the measurement of the tunneling current. The QTF sensor is excited in z direction by an additional piezoelectric actuator that is driven with a sinusoidal voltage of adjustable amplitude and frequency. The tuning fork oscillating with a frequency ω causes a piezoelectric sinusoidal voltage response $V_\sim = \hat{V}_\sim \sin(\omega t)$. Deflection of the free beam leads to a distortion of its cross-section[45] and consequently surface charges arise charging the top and bottom of the beam opposite to its sides[46]. $V_\sim$ is measured by wires connected to two pairs of metallic contacts evaporated onto the faces of the free prong.

Amplitude Calibration

Prior to the experiments, the oscillation amplitude A requires calibration. The relation between A and the measured voltage amplitude $\hat{V}_\sim$ is given by a constant α, i.e., $A = \alpha \hat{V}_\sim$. Previously, it was shown that for large amplitudes $A > 500$ pm increasing the amplitude by ΔA in constant-current mode causes the tip to retract by $\Delta z = \Delta A$ (ref. 47). Hence, α may be obtained by increasing

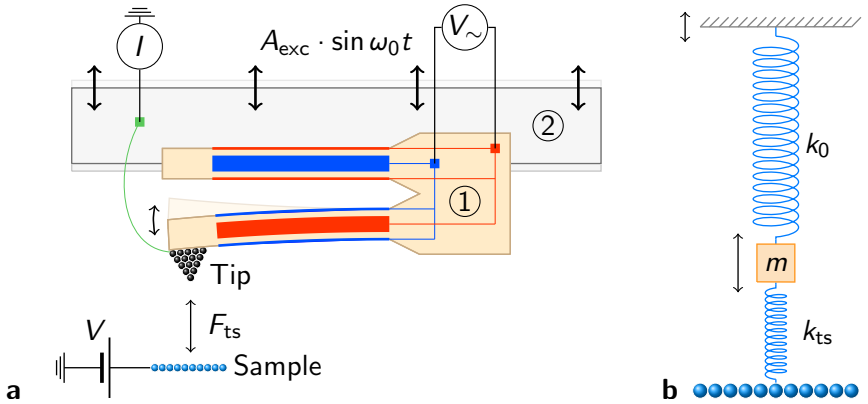

Figure 2.11. **a**, Sketch of a quartz tuning fork (TF) ① connected to a tip holder ②. The sensor oscillation is excited by a sinusoidal movement of the tip holder $A_{exc} \cdot \sin \omega_0 t$. The excitation leads to an oscillation of the free TF prong inducing a sinusoidal piezo voltage response $V_\sim$ that is measured by two sets of contacts on each prong (blue, red). The tunneling current I flowing between tip (black circles) and sample (blue circles) is measured by a small wire (green). A bias V is applied to the sample. **b**, Equivalent representation as harmonic oscillator. The tip is coupled to the tip holder (sample) by a spring of stiffness k_0 (k_{ts}).

the excitation amplitude and measuring the change of the oscillation voltage $\Delta\hat{V}_\sim$ as well as tip displacement Δz, i.e., $\alpha = \Delta z / \Delta\hat{V}_\sim$.

2.5. Forces on the Atomic Scale

At the atomic scale, several forces contribute to the total interaction between an atomically sharp metal tip and a metallic substrate. In vacuum, van-der-Waals (vdW), electrostatic, magnetic, and chemical interaction forces are operative. Van-der-Waals forces arise due to charge fluctuations that lead to a temporary electric dipole moment. Adjacent particles are polarized parallel to the polarizing dipole moment yielding attraction. The van-der-Waals energy of two atoms separated by the distance r exhibits a r^{-6} dependency[25]. Assuming additivity of vdW forces and neglecting retardation effects[48] yields a simple expression for the interaction between a sphere and a flat surface[49]

$$E_{vdW} = -\frac{\mathcal{H} r_t}{6z} \tag{2.48}$$

$\mathcal{H}$ denotes the material-dependent Hamaker constant, r_t the sphere radius, and z the closest sphere-surface separation.

Electrostatic forces are caused by charges present in tip and sample. When two metals are in close proximity to each other, electrons tunnel in order to align the chemical potentials of both electrodes. Hence, charges accumulate at their surfaces that induce an intrinsic potential difference, commonly referred to as contact potential difference (CPD), V_{cp}. The magnitude of V_{cp} is governed by the work function Φ of both metals. Φ represents the difference between vacuum level E_∞ and chemical potential μ, $\Phi = E_\infty - \mu$. Hence, $eV_{cp} = \Phi_t - \Phi_s$. An externally applied bias voltage V likewise charges the capacitor formed by the two electrodes. The electrostatic interaction energy is specified as $E_{el} = \frac{1}{2}C(V - V_{cp})^2$ depending on the capacitance C. An

analytical expression for C between a sphere and a flat surface has previously been reported[50]

$$E_{\mathrm{el}} = -\pi\epsilon_0 r_{\mathrm{t}} (V - V_{\mathrm{cp}})^2 \ln z \tag{2.49}$$

(ϵ_0 - vacuum permittivity).

Chemical interaction forces between two atoms are commonly expressed using a Lennard-Jones (LJ) potential.

$$E_{\mathrm{LJ}} = \varepsilon \left[\left(\frac{z_{\mathrm{eq}}}{z} \right)^{12} - 2 \left(\frac{z_{\mathrm{eq}}}{z} \right)^{6} \right] \tag{2.50}$$

(ε - depth of the potential well, z_{eq} - equilibrium distance). E_{LJ} consists of a repulsive, short-range first term due to Pauli repulsion as well as an attractive, long-range second term representing vdW interaction between two point-like particles. In most cases, E_{LJ} approximates the chemical interaction sufficiently, especially in experiments probing one dimension. Due to the neglect of angular dependencies relevant for atomic orbitals, a detailed description of whole surfaces such as that of Si(111)[51] requires more complex models[52].

The total energy is given by a linear superposition of contributing energies. Forces can be derived from the interaction energy by the general relation $F = -\partial_z E$. The stiffness k is given by the negative force gradient $k = -\partial_z F = \partial_z^2 E$. E, F, and k for exemplary parameters considering electrostatic, LJ, and vdW interactions are visualized in Fig. 2.12.

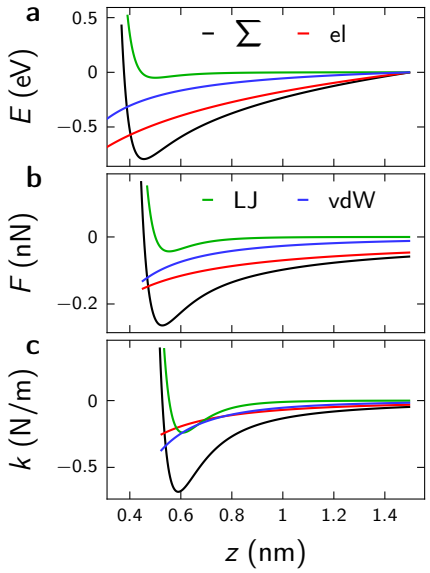

Figure 2.12. Exemplary potential energy E (**a**), force F (**b**), and stiffness k (**c**) occurring in atomic scale junctions in UHV. The total interaction ($\sum$, black) is shown as linear superposition of electrostatic (el, red), Lennard-Jones (LJ, green), and van-der-Waals interaction (vdW, blue). The energies are shifted vertically in order to set their value at $z = 1.5\,\mathrm{nm}$ to zero. Input parameters are $r_{\mathrm{t}} = 10\,\mathrm{nm}$, $\varepsilon = 50\,\mathrm{meV}$, $\mathscr{H} = 0.1\,\mathrm{eV}$, $V = 0.3\,\mathrm{V}$, $V_{\mathrm{cp}} = -0.2\,\mathrm{V}$, and $z_{\mathrm{eq}} = 0.5\,\mathrm{nm}$.

2.6. Data Analysis

In the present work, curve fitting was performed for several data sets. The Levenberg-Marquardt algorithm was employed in order to carry out least squares optimization, i.e., finding min χ^2. Data pairs of dependent quantities X and Y, i.e., (x_i, y_i), are compared to the value that is calculated for the target function $f(x, \mathfrak{P})$ with parameter set $\mathfrak{P}$.

$$\chi^2 = \langle [Y - f(X, \mathfrak{P})]^2 \rangle \tag{2.51}$$

Throughout this work, the coefficient estimate $\mathfrak{C}$ for an element of $\mathfrak{P}$ obtained from the fitting routine is given considering the one-sided 95 % confidence interval $[\mathfrak{C} - \delta\mathfrak{C}, \mathfrak{C} + \delta\mathfrak{C}]$ following the notation $\mathfrak{C} \pm \delta\mathfrak{C}$.

Distributions of a quantity X adopting n values x_i ($i \in [1, n]$) are presented as mean value $\mu_X = \bar{x}$ with the standard deviation σ_X using the notation $\mu_X \pm \sigma_X$.

$$\mu_X = \frac{1}{n}\sum_{i=1}^{n} x_i \tag{2.52}$$

$$\sigma_X = \sqrt{\frac{1}{n-1}\sum_{i=1}^{n}(x_i - \bar{x})^2} \tag{2.53}$$

Correlations of two variables X and Y are quantified using the Pearson correlation coefficient $\mathfrak{r}_{X,Y}$ (ref. 53).

$$\mathfrak{r}_{X,Y} = \frac{\mathrm{cov}\,(X,Y)}{\sigma_X \sigma_Y} \tag{2.54}$$

cov (X, Y) is the covariance of X and Y. X and Y comprise n values x_i and y_i, respectively. cov (X, Y) is then calculated as

$$\mathrm{cov}\,(X,Y) = \frac{1}{n}\sum_{i=1}^{n}(x_i - \bar{x})(y_i - \bar{y}) \tag{2.55}$$

$\mathfrak{r}_{X,Y}$ adopts values between –1 and +1. +1 (–1) implies a perfect positive (negative) linear correlation, whereas 0 stands for no linear correlation. Commonly, $|\mathfrak{r}| \geqslant 0.7$ is considered as strong correlation[54]. Examples of $\mathfrak{r}$ for different randomly generated sets of (x,y) data are presented in Fig. 2.13.

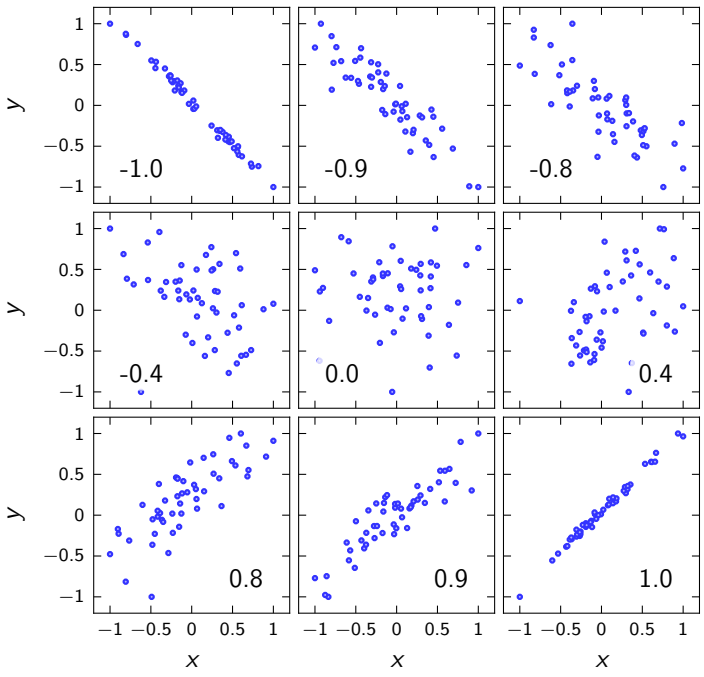

Figure 2.13. Visualization of the Pearson correlation coefficient $\mathfrak{r}$ for different sets of (x,y) data. $\mathfrak{r}$ for each set is indicated at the bottom of the corresponding panel.

Chapter 3

Optimization of an Atomic Force Microscope

Scanning tunneling and atomic force microscopes are delicate tools that allow the measurement of currents and forces at the atomic scale. The resolution of such microscopes is limited. Thermal excitation of electrons in a resistor of resistance R introduces Johnson-Nyquist noise on the current $\delta I_{\text{J–N}} = \sqrt{4 k_B T B / R}$ increasing with temperature T and bandwidth B (ref. 55,56). The energy resolution is limited by thermal fluctuations superimposed on the bias voltage applied to the tunneling junction and can be estimated by the FWHM of eq. (2.16), $\delta E = 3.53 k_B T$. Thermal fluctuations present at the tuning fork allow a minimum detectable frequency variation $\delta f_{\text{th}} = \sqrt{k_B T B_m f_0 / \pi k A^2 Q}$ (B_m - measurement bandwidth)[57]. At 5 K, these limits are of the order $\delta I_{\text{J–N}} \sim 0.1$ pA [with $B = 3$ kHz, $R = 100$ MΩ (ref. 58)], $\delta E \sim 1.5$ meV, and $\delta f_{\text{th}} \sim 0.1$ Hz [using $f_0 = 30$ kHz, $Q = 30000$, $k_0 = 1800$ N/m, $A = 50$ pm, and $B_m = 500$ Hz].

However, these limits are often not reached in practice. Mechanical vibrations and acoustic disturbances of the experimental setup modify the real tip–sample separation which manifests itself as a stochastical variation of the measured tunneling current and tip–sample force. Athermal fluctuations arising from triboelectric effects, electromagnetic interference of wireless communication techniques, and an insufficiently decoupled power grid introduce electronic disturbances that reduce the microscope resolution[59–63]. Voltage variations of standard deviation δV increase the effective temperature $T_{\text{eff}} = \sqrt{T^2 + T_V^2}$ with $T_V = \sqrt{3 e^2 \delta V^2 / k_B^2 \pi^2}$ (ref. 64).

The AFM is particular sensitive to external disturbances. In order to drive a tuning fork of quality factor $Q = 30000$ at an amplitude $A = 30$ pm, an excitation amplitude $A_{\text{exc}} = A/Q = 1$ fm is required [cf. eq. (2.43)]. The corresponding driving voltages amount to few mV. The oscillation of the quartz sensor leads to AC currents of the order 1 pA that are converted by an internal amplifier with gain 10^8 V/A. The resulting AC voltage (~ 0.1 mV) is passed through the cryostat, bandpass filtered and amplified at ambient conditions. Consequently, minimizing external disturbances is crucial for high-resolution nc-AFM.

For the work presented in this thesis, a commercially available system provided by Createc Fischer & Co. GmbH was utilized. However, the as-installed system proved unsuitable for high resolution scanning tunneling spectroscopy as well as atomic force microscopy. Prelimi-

nary measurements revealed significant external noise that yielded effective temperatures ∼13 K at measurement temperatures ∼7 K. Moreover, stable operation of the atomic force microscope at oscillation amplitudes below 200 pm was prevented by an inadequate signal-to-noise ratio of the tuning fork oscillation signal.

In the following, the initial experimental setup is introduced. Several substantial amendments have been elaborated during this thesis in order to reduce thermal excitations as well as athermal disturbances and stabilize the AFM signal. Finally, a brief summary of the optimized instrumental characteristics is given.

3.1. Initial Setup

The experimental setup used in the present experiments is based on a commercially available system (LT-STM-AFM-2) distributed by Createc Fischer & Co. GmbH. Two ultra-high vacuum (UHV) chambers allow spatially separated preparation and analysis of samples with diameter up to ∼5 mm. The preparation (PC) and analysis (AC) chambers are separated by a gate valve enabling *in-situ* sample transfer. The PC is connected to a load lock (LL) chamber via a gate valve in order to introduce tips and samples without breaking the vacuum of the main chambers. The PC features a facility for sample preparation via Ar^+ ion bombardment (Specs IQE 11/35) and thermal annealing (radiative annealing up to ≈ 1000 K, electron bombardment up to ≈ 2300 K). A second facility for high temperature annealing above 3000 K was developed by the author prior to the experiments depicted in the present work[65]. Two electron beam evaporators (Createc EBE-40-1-180-WK-SH, Omicron EFM 3) are installed in the PC allowing either thermal evaporation from a metal rod or deposition of molecules using a heated crucible. An additional, self-assembled, and resistively heated crucible for molecule evaporation is installed. A quartz microbalance which is operated by an Intellemetrics IL 150 quartz crystal growth rate monitor at 6 MHz enables the detection of the molecule flux. A quadrupole mass spectrometer (Pfeiffer Prisma Plus QMG 220) allows analysis of the residual gas composition.

The UHV is maintained via turbomolecular pumps (Pfeiffer HiPace 300; PC and LL), and ion-getter with integrated titanium sublimation pumps (Gamma Vacuum 300TV; AC and PC). A He bath cryostat (Cryovac, CR-2-D) allows the operation of a Pan-type[66] STM/AFM head cooled with liquid helium. The outer (14 l) and inner (4 l) cryostat dewars designated for liquid N_2 and liquid He, respectively, present a holding time of ≈ 72 h without tip or sample transfer. Tips and samples can be exchanged *in-situ*. Sample plates comply with the standardized Omicron design. Tips are mounted at the bottom of ceramic cylinders of diameter 6.5 mm and height 5.0 mm. The STM/AFM head features a corresponding cylindrical slot. A spring wrapped around the cylinder fixes the tip holder by pressing it to the top of the slot. Before a tip transfer, the spring is compressed with a tool mounted to the tip of a wooble stick and the cylinder subsequently removed from or inserted into the slot. The top of the cylinders and the top of the slot feature three contacts (one for the tunneling current, two for the AFM oscillation signal).

The STM/AFM head located below the cryostat is suspended on springs and features an eddy current damping system. The whole UHV system is vibrationally isolated from the surrounding building by a concrete block standing directly on the bedrock. Four pneumatic isolation dampers (Newport S-2000) separate the steel frame of the UHV system from the concrete block.

Single atoms can be deposited onto the cold sample residing inside the microscope by evaporation from a heated metal rod (Omicron EFM 3). A NiTi coil which is superconducting below 10 K allows the application of a magnetic field up to 2 T perpendicular to the surface. A Zener diode BZT03-C200 located next to the sample permits heating up to ≈ 10 K. Lake Shore diodes DT-670A1-BO (next to the sample) and DT-670B1-BO (attached to the inner cryostat) are employed for temperature measurements.

The tunneling current is passed through the cryostat, converted into a voltage and amplified using a transimpedance amplifier (Femto DLPCA-200) with variable Gain (10^3 to 10^9). Direct measurement of the $\mathrm{d}I/\mathrm{d}V$ signal is achieved using a Lock-In amplifier (Stanford Research Systems SR830) which allows amplitudes 0.004 to 5 V_{RMS} at frequencies 1 mHz to 102 kHz. The AFM oscillation signal is amplified by an internal amplifier (Createc LT-STM-B-131, Gain 10^8, bandwidth 500 Hz) located at the inner side of the outer shield, i.e., operated at 78 K, and then processed using a combined bandpass and low-noise voltage preamplifier (Stanford Research Systems SR560). The amplified signal is fed into a floating-point digital signal processor (Texas Instruments, TMS320C6711D), part of the digital feedback system. A digital phase-locked loop (PLL) is utilized to drive the sensor at its resonance frequency and monitor the change from the unperturbed ($F_{ts} = 0$) resonance frequency. Tuning forks identical to those used in Swatch watches featuring a stiffness 1800 N/m, resonance frequency without tip of 2^{15} Hz = 32768 Hz, and quality factor $5000 < Q < 10000$ at 78 K and $20000 < Q < 60000$ at $\sim$5 K are employed.

3.2. Optimized Configuration

In order to decrease the base temperature, the thermal coupling of the inner (He) cryostat to the STM/AFM head was improved. The initial setup featured multiple 50 μm thick Ag wires soldered to Cu plates, the latter being screwed to the cryostat and STM/AFM head. Additional Ag wires were inserted connecting the inner cryostat to the head. Indium foil was added between the plates and the cryostat walls. Indium is an easily malleable material that permeates into the microscopic asperities of the materials it is pressed between. Hence, the microscopic contact area and the thermal conductivity through the Indium filled contacts is enhanced.

These changes reduced the base temperature from 6.9 K to 5.7 K. Additional Ag wires did not improve the temperature further. The discrepancy between the final base temperature and the target temperature of 4.5 K is most likely due heat introduction by the pulling mechanism. The latter allows the fixing of the STM/AFM head during tip or sample transfer and is not thermally coupled to either cryostat. Its temperature is thus presumed much larger than 4.2 K and the resulting (mainly radiative) heat transfer to the microscope considerable. Since the head has to be fixed during tip and sample transfer, the pulling mechanism cannot be firmly connected to either cryostat. For future improvement, the attachment of flexible wires between the mechanism and a cryostat may be considered.

Moreover, analysis of the tunneling voltage signal fed into the cryostat revealed a significant amount of fluctuations. In order to minimize electromagnetic interference, all cables entering and leaving the cryostat were covered with aluminum foil. RC low-pass filters (LPF) with cutoff frequency $f_c = 1$ kHz were installed filtering the control voltages for x, y, and z piezo movements. During experiments, the diodes for temperature measurements were disconnected and

all disconnected cables entering/leaving the cryostat isolated as well as wrapped with aluminum foil. Moreover, all power supplies not necessary for the operation of the STM were disconnected from the power grid. These measures proved sufficient to reduce the bias noise to the detection threshold.

Fig. 3.1 **a** shows spectroscopy data of the superconducting Nb(110) surface prior to the optimization. A BCS fit (red) yields an effective temperature of 13.2 K whereas spectroscopy subsequent to the measures described above revealed an effective temperature of 6.4 K (Fig. 3.1 **b**). The effective temperature is slightly higher than the readout of the temperature diode $T_{\mathrm{Diode}} = 6.2\,\mathrm{K}$. This discrepancy may be due to residual bias noise, a slightly distorting background DOS of tip and/or sample, and additional intrinsic broadening mechanisms such as lifetime broadening[67,68] or energy exchange with the electromagnetic environment[69], that are not considered in the fit. A second BCS fit using the fit parameters of Fig. 3.1 **b** and an additional modulation broadening $V_{\mathrm{m}}^{(2)} = 2.3\,\mathrm{mV_{RMS}}$ matches the data prior to the optimization (green line in Fig. 3.1 **b**). The importance of a low athermal noise level is revealed by comparing fit values of the energy gap Δ. A large noise superimposed on the junction voltage yields distorted gap values ($\Delta_{\mathrm{a}} = 1.44\,\mathrm{meV}$ vs. $\Delta_{\mathrm{b}} = 1.26\,\mathrm{meV}$). According to eq. (2.5), Δ_{a} is equivalent to a sample temperature of 4.1 K, whereas Δ_{b} corresponds to 6.2 K, matching the read-out of the temperature diode.

In order to improve the vacuum, a non-evaporable getter (NEG) pump (Gamma Vacuum `N400`) was mounted to the AC. NEGs are efficient in reducing CO, CO_2, O_2, N_2, and especially H_2 partial pressures. The active material of Gamma Vacuum `N50` to `N400` pumps consists of Zr (70%), V (24.6%), and Fe (5.4%). NEGs getter gases by dissociation and subsequent absorption into their bulk material. Installation of the NEG reduced the base pressure from $8 \cdot 10^{-11}\,\mathrm{mbar}$ to $1 \cdot 10^{-11}\,\mathrm{mbar}$.

The standing time of the cryostat amounts to ∼72 h. After refilling the outer cryostat with liquid N_2, a beating pattern of zero-to-peak amplitude up to ∼30 pm superimposed on the z

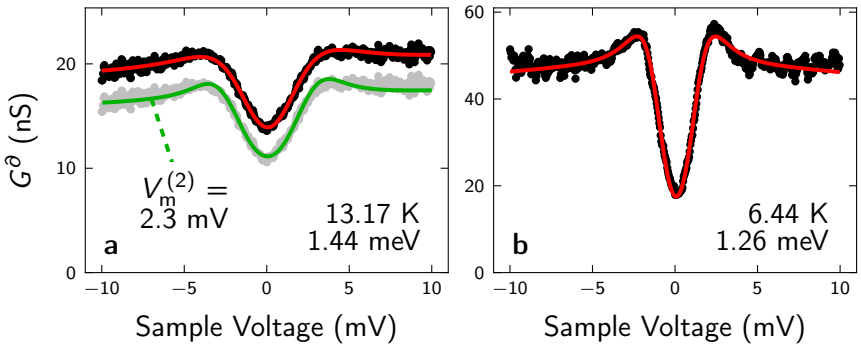

Figure 3.1. Comparison of tunneling spectroscopy (black, gray: shifted by -3 nS) of the superconducting energy gap of Nb(110) prior (**a**) and subsequent (**b**) to the modifications outlined in Sec. 3.2. The feedback has been disabled at 20 mV, 0.41 nA (**a**) and 0.92 nA (**b**) at a measurement temperature of 7.1 K (**a**), and 6.2 K (**b**). A modulation voltage of **a**, $V_{\mathrm{m}} = 0.5\,\mathrm{mV_{RMS}}$ and **b**, $V_{\mathrm{m}} = 0.15\,\mathrm{mV_{RMS}}$ was applied. BCS fits (red) yield fit parameters $\Delta = 1.44 \pm 0.02\,\mathrm{meV}$, $T_{\mathrm{t}} = 13.17 \pm 0.21\,\mathrm{K}$ (**a**) and $\Delta = 1.26 \pm 0.01\,\mathrm{meV}$, $T_{\mathrm{t}} = 6.44 \pm 0.10\,\mathrm{K}$ (**b**). The green line in **a** represents the BCS fit of **b** with an additional modulation broadening of $V_{\mathrm{m}}^{(2)} = 2.3\,\mathrm{mV}$.

signal in constant current mode was visible for up to 48 h (cf. Fig. A.2 **a**). Commonly, cryostats are operated with the liquid N_2 input closed and the gaseous N_2 exhaust output opened in order to avoid pressure build-up of evaporating nitrogen. In the present setup, the beating pattern could be eliminated by either closing or opening both pipes of the cryostat (cf. Fig. A.2 **b**). The frequencies of the beating pattern, 4.2 Hz and 4.5 Hz (cf. Fig. A.2 **c**), are in the range of mechanical frequencies and most likely correspond to natural frequencies of cryostat oscillations that are excited by boiling of the liquid N_2.

In addition to the measures applied in order to reduce electromagnetic disturbances outlined above, the AFM noise was addressed by several means. Isolation transformers were added between the electrical outlets and the power supplies required for the operation of the AFM thus shielding the system from noise originating from the power grid. All grounding cables were replaced by a single cable removing ground loops. LPFs ($f_c = 1$ Hz) were introduced between the power supply of the internal preamplifier and the internal preamplifier.

Moreover, the electrical connections for measuring the tunneling current and the AFM oscillation signal were replaced by cables directly soldered to the top of the tip holders. In the initial setup, the electrical connection required the spring to press the sensor contacts to the corresponding contacts at the top of the slot. Two problems arose with the initial configuration. First, the measured amplitude was critically dependent on the exact positioning of the tip holder inside the slot. Small position changes altered the measured oscillation amplitude by up to three orders of magnitude. For some circumstances, no oscillation was detectable at all. Maximization of the AFM signal proved to be stochastic and time consuming. Second, the oscillation amplitude changed during the cool-down of the microscope from liquid N_2 to liquid He temperatures as well as during the tip approach. Both factors rendered measurements with a high AFM oscillation signal and hence large signal-to-noise ratio impossible. In order to circumvent these problems,

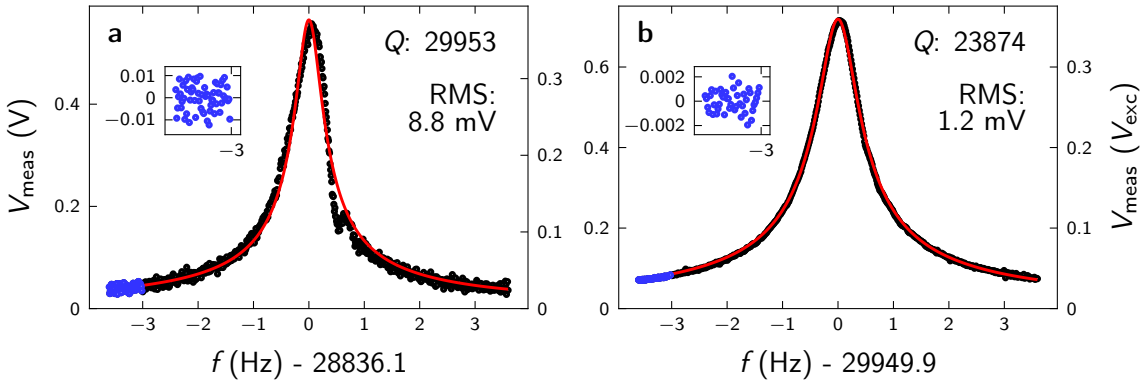

Figure 3.2. Measured tuning fork oscillation amplitude (black) at 6 K as a function of excitation frequency f prior (**a**) and subsequent (**b**) to the modifications outlined in Sec. 3.2. Red lines denote a fit to the harmonic oscillator model. The force sensors were excited with $V_{exc} = 1.5$ V (**a**) and $V_{exc} = 2$ V (**b**). Resonance frequencies are $f_0 = 28.8$ kHz (**a**) and $f_0 = 29.9$ kHz (**b**). The quality factors calculated from the FHWM yield $Q = 29953$ (**a**) and $Q = 23874$ (**b**). The data depicted in blue are used to estimate the noise level. For this purpose, the data are subtracted by a quadratic fit within the selected interval (inset). The RMS values of these data amount to 8.8 mV (**a**) and 1.2 mV (**b**).

the AFM cables were soldered directly to the tip holder. This measure yielded a constant and high amplitude of the measured AFM signal.

A resonance curve obtained prior (subsequent) to the modifications outlined above is presented in Fig. 3.2 **a** (**b**). Fig. 3.2 **a** was measured prior to the tip approach after manually maximizing the AFM amplitude whereas Fig. 3.2 **b** was obtained already in close proximity to the sample. A reduced noise level and consequently enhanced signal-to-noise ratio subsequent to the modifications is exposed in Fig. 3.2 **b**. The RMS of the data yields a noise reduction of 86% (8.8 mV $\rightarrow$ 1.2 mV, inset of Fig. 3.2 **a,b**). Moreover, a slight asymmetry with respect to the resonance frequency is clearly visible in Fig. 3.2 **a**. Asymmetric resonance curves were commonly observed prior to the modifications and were previously assigned to parasitic capacitances arising at electrical contacts[70]. The successful removal of the asymmetry (Fig. 3.2 **b**) indicates a suboptimal position of the sensor accompanied by an imperfect electrical contact in the initial configuration, which was corrected by directly soldering wires to the contacts at the tip holder.

3.3. Conclusions

Several substantial improvements were made that enable state-of-the-art current and force spectroscopies of single-atom and single-atom junctions. Key performance indicators are summarized in Tab. 3.1. The base temperature of the microscope was reduced by 1.2 K by enhancing the thermal connection between the STM/AFM head and the bath cryostat. Mounting a NEG pump to the AC improved the base pressure from $8 \cdot 10^{-11}$ mbar to $1 \cdot 10^{-11}$ mbar. The effective electronic temperature was reduced from above 13 K to 6.4 K at 6.2 K primarily by the reduction of electromagnetic interference. The AFM noise was reduced by 86 % and the oscillation signal stabilized by reducing electronic noise originating from power supplies and ground loops as well as by optimizing the electrical connection to the sensor.

	initial	optimized	change
Base temperature (K)	6.9	5.7	-17 %
Base pressure (mbar)	$8 \cdot 10^{-11}$	$1 \cdot 10^{-11}$	-88 %
Effective temperature (K)	13.2 [(a)]	6.4 [(b)]	-52 %
RMS noise AFM (mV)	8.8	1.2	-86 %

Table 3.1. Comparison between the initial and the optimized configuration. [(a)] measured at 7.1 K. [(b)] measured at 6.2 K.

Chapter 4

Superconductivity of Single C_{60} Molecules on Nb(110)

The results presented in this chapter have been published in Phys. Rev. Lett. ***118****, 107001 (2017). Theoretical support was provided by* ***Pedro Ribeiro*** *(CeFEMA, Instituto Superior Técnico, Universidade de Lisboa, Av. Rovisco Pais, Lisboa, Portugal) and* ***Stefan Kirchner*** *(Center for Correlated Matter, Zhejiang University, Hangzhou, Zhejiang, China).*

Superconductivity is characterized by the superconducting order parameter Δ - a quantity that is highly sensitive to the electronic environment. In conventional superconductors, it describes the pairing correlations between electrons of opposite spin and momentum. It is associated with a pairing potential originating in bulk superconducting materials. At the interface of a superconductor $\mathcal{S}$ with a non-superconducting normal metal $\mathcal{N}$ the pairing potential does not drop to zero abruptly but vanishes gradually. Hence, superconducting properties are induced in $\mathcal{N}$.

The transfer of an electron from $\mathcal{S}$ to $\mathcal{N}$ is depicted by the process of Andreev reflection (AR)[36]. AR describes the reflection of a single electron incident from $\mathcal{N}$ at the $\mathcal{NS}$ interface as a phase-conjugated hole. Charge and particle number are conserved since the process is accompanied by the addition of a Cooper pair (CP), i.e., two electrons of opposite spin, to the superconducting condensate. Thus, AR presents the mechanism responsible for the transformation of single electrons into CPs and vice versa which determines charge transport across the $\mathcal{NS}$ interface at low bias voltage. The observation of electron transport governed by AR in $\mathcal{NS}$ and multiple AR (MAR) in $\mathcal{SS}$ junctions has considerably advanced the state of knowledge in the field of transport through contacts involving superconducting materials. The transmission probabilities of transport channels in atomic $\mathcal{SS}$ junctions were determined using the energy-dependence of MAR signatures[71]. AR provided tunable supercurrents through semiconductor nanowires contacted with $\mathcal{S}$ electrodes[72], electron transport through graphene quantum dots[73], and correlated spin currents in topological superconductors[74].

The spatial range in which AR occurs determines the region where superconductivity is induced in $\mathcal{N}$[75]. This phenomenon commonly referred to as the Superconducting Proximity Effect (SPE) represents a macroscopic manifestation of the microscopic AR process[76]. The SPE is commonly described as the pairing correlation (potential) *leaking* from $\mathcal{S}$ into $\mathcal{N}$. Close to the $\mathcal{NS}$ interface, Δ is finite in $\mathcal{N}$ and reduced from the bulk value of $\mathcal{S}$. First experimental evidence of the SPE has been reported in 1932 when Holm and Meissner observed a vanishing contact resistance of two superconductors separated by a layer of non-superconducting material[77]. Subsequently, the interplay of a normal metal or ferromagnet and a superconductor has attracted significant experimental[78–88] as well as theoretical[89–93] attention. The focus in these experiments rested firmly on the interplay of elementary metals or compounds consisting of two elements forming two-dimensional layers whereas the SPE in more complex structures or molecules has scarcely been examined. Notable exceptions include experiments comprising Cu[86] and InAs[72] nanowires, carbon nanotubes[94–96], DNA[97], a single-molecule transistor[98], and manganese-phthalocyanine[99].

AR spectroscopy is commonly performed using so-called "Andreev Reflection point contact spectroscopy" (ARPCS) experiments[100–107], where tip radii are commonly of the order 1 μm (ref. 100) to 100 μm with protrusions of the order 1 μm (ref. 101). Tip-sample distances are controlled via differential[100] or micrometer[101,105] screws and often deformed during the experiments[100] at conductances of the order 100 G_0 (ref. 100,102) to 5000 G_0 (ref. 101). Thus, ARPCS contacts are considered macroscopic.

AR has also been probed in microscopic contacts using the STM[102,108,109]. Although contacts comprised of a small number of atoms were reported, the spatial imaging capability of the STM has not been employed to examine the impact of topographic features on AR. In this chapter, the impact of the atomic-scale contact geometry on AR is unraveled. Contacts comprising metallic electrodes as well as single C_{60} molecules deposited on Nb(110) were studied during the transition from tunneling to contact. A zero-bias peak associated with AR emerges in W–Nb, W–C_{60}, and C_{60}–Nb contacts alike. The connection between BTK transmission and differential conductance exhibits subtle variations that are traced to geometric differences. Finally, the result of transport calculations[110] is presented elucidating the impact of C_{60} orientation on the transmission probability of its transport channels.

4.1. C_{60} Molecules on Nb(110)

Niobium is a transition metal located in the 5$^{\text{th}}$ group of the 5$^{\text{th}}$ period of the periodic system. Nb is a type II superconductor and the element with the highest transition temperature $T_c = 9.25\,\text{K}$ (ref. 111–115), largest energy gap $\Delta = 1.52\,\text{meV}$ (ref. 116,117) as well as highest critical field $B_c = 190\,\text{mT}$ (ref. 118,119). Nb is a refractory metal, i.e., it is highly resistant to temperature and has a rather high melting temperature (2750 K). Refractory metals and especially Nb exhibit a large affinity to oxygen and form resilient compounds[120–130]. The superconducting properties of Nb are sensitive to oxygen contamination[113,120,131]. Moreover, Nb(110) surfaces exhibit a characteristic superstructure[124,126,127,129,130] due to the presence of oxygen at the surface[120–127,129,130]. Here, the bcc Nb(110) crystal is terminated by a monolayer of NbO, the latter being a modification of fcc NbO(111), a NaCl type crystal with 25% vacancies in the Nb and O sublattices[129]. The NbO layer is covered by linear chains consisting of Nb atoms[129] that are visible in STM

imaging[124,126,127,129,130]. While the oxygen-reconstruction can be readily prepared, obtaining a pristine Nb(110) surface requires significant effort. Only two reports of a clean Nb(110) surface exist to date, which have been obtained by sputter deposition of Nb on a sapphire substrate[125] and preparing a Nb(110) crystal by repeated ($\approx$ 100) sputtering and annealing cycles[130].

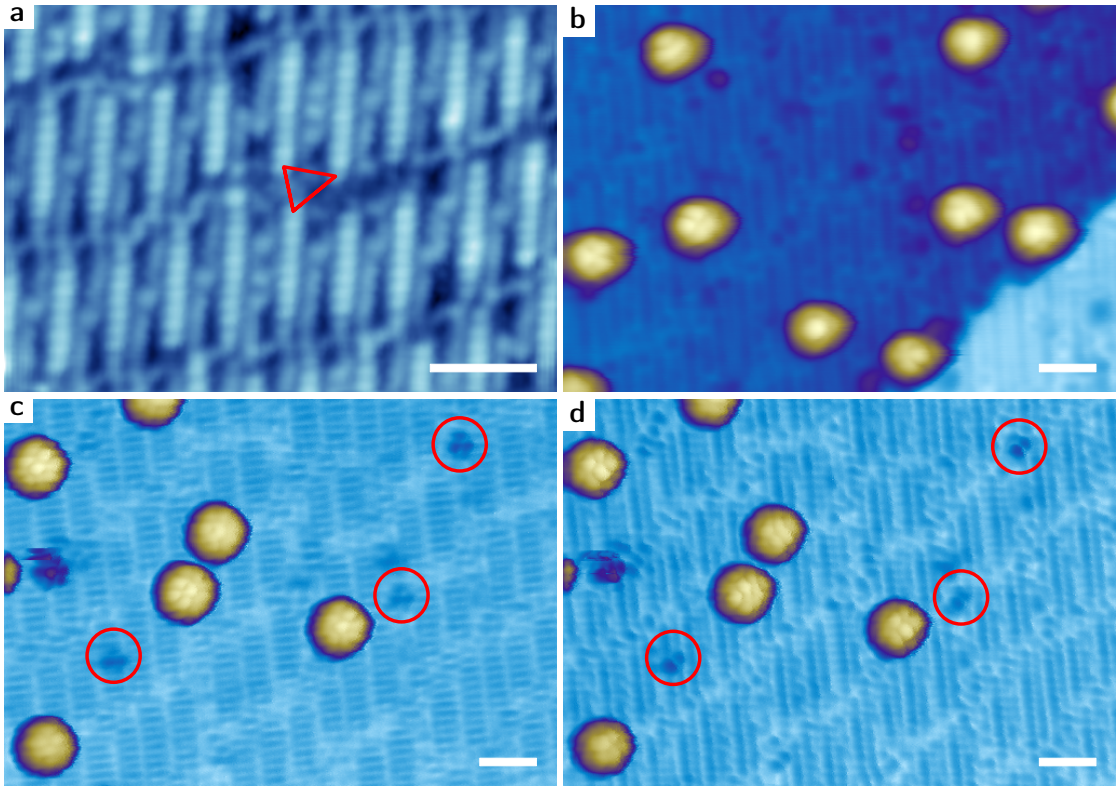

Figure 4.1. Constant-current topography of **a**, NbO and **b-d**, C_{60}/NbO. **c,d** were obtained with a C_{60}-terminated tip as evidenced from reverse imaging of the molecule at the tip apex at atomic defects[132,133] (red circles). Scanning parameters are **a**, 0.1 V, 0.5 μA and **b-d**, 0.1 V, 50 pA Apparent heights amount to 0.10 nm (**a**), 1.0 nm (**b**), 0.84 nm (**c**), and 0.86 nm (**d**). The image of **a** was processed by applying a 20 pt gaussian filter. In **a,c,d**, 40%, 20%, and 20% of the second derivative, respectively, were subtracted. Scale bar 2 nm. The preferential adsorption site of C_{60} molecules is indicated as red triangle in **a**. **b-d** are reproduced from ref. 65.

In the present experiments, the Nb(110) crystal was prepared by repeated annealing between 2200 and 2650 K (close to the melting temperature of Nb, 2750 K) for several hours. This procedure yielded the bulk Nb(110) substrate covered by a monolayer of oxygen-containing Nb terminated by the characteristic Nb chains, referred to as NbO in the following. A single flash cycle at 2650 K for 10-15 s was found sufficient for the subsequent removal of residual contaminants from the surface, restoring the NbO surface. Fig. 4.1 **a** presents a topographic image of the NbO surface exhibiting the characteristic Nb chains. The Nb chains consist of a varying number of Nb atoms and hence do not organize with long range order. A detailed analysis highlighting the structural heterogeneity visible in the variation of the chain length and geometry of the area enclosed by three Nb chains is shown in Fig. A.3.

C_{60} molecules were evaporated onto the NbO surface from a heated crucible. Fig. 4.1 **b** exhibits several C_{60} molecules on NbO. C_{60} preferentially adsorbs to three-fold coordinated hollow

sites (triangle in Fig. 4.1 **a**) in the trench between two rows of Nb chains. Submolecular resolution is visible in Fig. 4.1 **b** revealing a unique structural motif for virtually every molecule. This result reflects the topographic heterogeneity of the substrate that leads to a unique geometric environment for every C_{60} molecule and consequently a unique coupling / hybridization with the substrate. Thus, the spatial distribution of the molecular orbitals is unique for every C_{60} (see below).

C_{60}-terminated tips are obtained following previously reported procedures[132,133]. The pristine W tip is approached to the center of a C_{60} molecule until current discontinuities signal the transfer of the molecule to the tip apex. This procedure is successful for approximately every second molecule when the feedback loop is disabled at 0.1 V, 0.1 nA and the tip approached by $\Delta z = 0.7$ nm. The success of the C_{60} transfer can be verified in several ways[132]. First, the transferred molecule is absent from the surface. Second, the differential conductance trace is mirrored with respect to zero bias[132]. Third, topographic features are modified since the tunneling current consists of the convolution of the DOS of the surface with the DOS of the tip. Imaging circularly symmetric atomic defects exhibits structural motifs reflecting the spatial distribution of the density of states of the C_{60} at the tip[132,133]. The features marked by circles in Fig. 4.1 **c,d** depict the distribution of the lowest unoccupied molecular orbital (LUMO)[134] with a hexagon (Fig. 4.1 **c**) and C-C bond (Fig. 4.1 **d**) of the molecule pointing toward the sample[135–139]. The LUMOs are centered at C pentagons (cf. Fig. 4.7 **g,i**). After obtaining the image of Fig. 4.1 **c**, the tip was approached to the NbO surface until a discontinuity in the current occurred. The contact with the surface caused a mechanical deformation of the tip–C_{60} interface which is reflected in the rotation of the C_{60} at the tip apex. The atomic defects (circles) visible in the subsequently obtained image (Fig. 4.1 **d**) indicate a rotation from a hexagon to a C-C bond pointing toward the surface. Moreover, C_{60} molecules on the surface imaged with a C_{60}-terminated tip exhibit a more complex pattern compared to C_{60} molecules imaged with a metallic tip[132]. The modified patterns of Fig. 4.1 **d** compared to Fig. 4.1 **c** are further indicators for a rotation of the molecule at the tip. Fourth, the topographic resolution is enhanced. Molecular orbitals are spatially confined compared to the delocalized s-wave orbitals of a metallic tip. Consequently, the Nb atoms of the chains in Fig. 4.1 **c,d** appear much sharper compared to Fig. 4.1 **a,b**. The chains in Fig. 4.1 **d** are duplicated since two LUMOs with approximately equal distance to the surface contribute to the tunneling current. The second chain appears displaced in the same direction and with the same distance as the double protrusion of the atomic defects (circles). Similarly, the chains visible in Fig. 4.1 **c** appear elongated in the same direction of two of the three LUMOs of the C_{60}-terminated tip. The discrepancy to the sharp double protrusions visible in Fig. 4.1 **d** originates from the contribution of the third LUMO, which is located at a distance to the center of the other two LUMOs comparable to the intra-chain Nb–Nb distance. This interpretation is consistent with the appearance of the protrusions at the top of each chain. Their reduced elongation originates from the sole contribution of a single LUMO to the current.

In molecules, the orbitals of the contributing atoms hybridize and form molecular orbitals (MOs). Symmetric molecules feature degenerate orbitals since their wave functions are invariant under spatial transformations. C_{60} molecules exhibit a fivefold, threefold, and threefold degeneracy of the highest occupied molecular orbital (HOMO), lowest unoccupied molecular orbital (LUMO), and next-to-lowest unoccupied molecular orbital (LUMO+1), respectively[140]. Adsorp-

tion of a molecule to a surface alters its electronic properties compared to the molecule in the gas phase. Commonly, the HOMO-LUMO energy gap Υ is considered as a measure of the coupling strength to a substrate[141–144]. The presence of a metallic substrate enables charge redistribution thus screening the addition or removal of electrons which reduces the energy required to add or extract an electron. Hence, the energetic position of MOs are shifted toward the Fermi level and Υ decreases[142,145]. In addition to that, interaction with the substrate atoms reduces the symmetry of the charge distribution within the molecule thus lifting degeneracy of certain energy levels[134,142]. Hybridization of molecular orbitals with substrate states leads to a broadening of the resonances[142]. When considering a molecular layer, additional charge screening and orbital overlap with adjacent molecules must be considered. For the process of tunneling into a molecule, Coulomb interaction between the electronic system and the tunneling electron enhances the apparent Υ (ref. 142,144), which is observable in STS. Estimating the apparent Υ as difference[142] of gas phase ionization potential (≈7.6 eV, refs. 146–149) and the electron affinity (2.7 eV, ref. 150) yields $\Upsilon \approx 4.9$ eV.

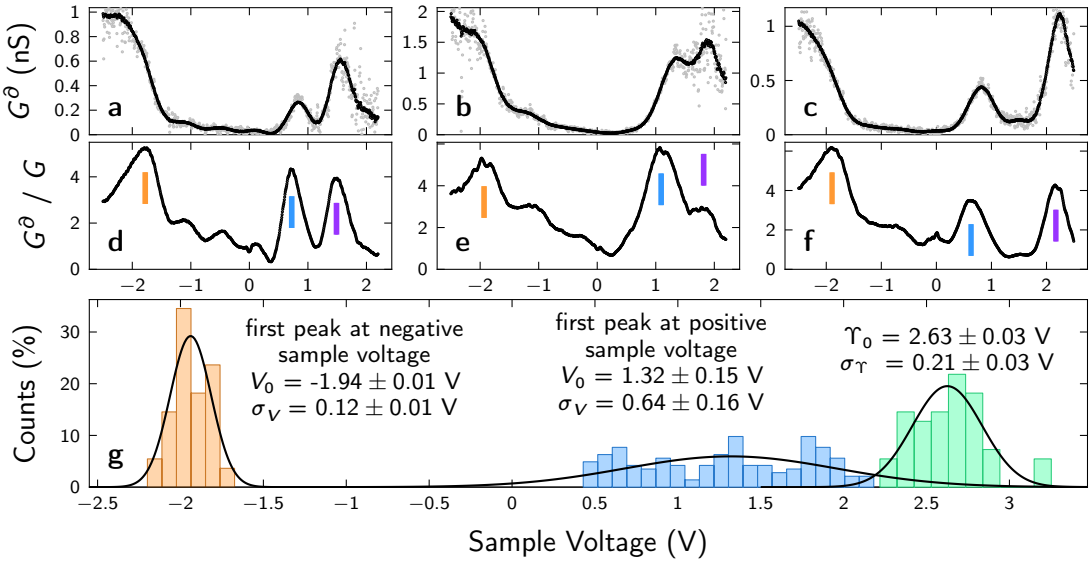

Figure 4.2. Electronic properties of C_{60} molecules adsorbed on NbO. **a-c**, Constant-height G^∂ and **d-f**, corresponding G^∂/G spectra acquired with a W tip atop single C_{60} molecules. Grey dots denote raw, black lines smoothed data. The feedback loop has been disabled at 0.1 V, 0.1 nA (**a**,**b**), and 2.5 V, 1.0 nA (**c**). The first G^∂/G peak at negative (positive) voltage is indicated as vertical orange (blue) bar, the second peak at positive voltage as violet bar. **g**, Histogram of peak positions of the first G^∂/G peak at negative (orange) and positive (blue) voltage. The distribution of the difference between both, the HOMO-LUMO gap Υ, is shown in green. Solid lines present Gaussian fits to the data. Fit values of the center voltage (V_0, Υ_0) and standard deviation (σ_V, σ_Υ) with corresponding uncertainty are indicated in the figure.

In the gas phase, DFT calculations predict $\Upsilon = 1.6$ eV (ref. 140). For a C_{60} crystal $\Upsilon = 3.7$ eV was measured[151]. On metal surfaces, 1.7 eV $\leq \Upsilon \leq$ 2.7 eV have been reported[132,135,138,142,152–160]. C_{60} molecules decoupled from a Au(111) substrate via rows of TPA molecules exhibit $\Upsilon = 3.5$ eV (ref. 159).

In the present experiments, G^∂ data exhibit two peaks at positive voltage whereas only a single

plateau-like feature is visible at $\approx -2\,\mathrm{V}$ (Fig. 4.2 **a-c**). In order to reduce the impact of the transmission factor and recover an identifiable peak at negative voltages, the data is normalized by dividing G^{∂} by G (cf. Sec. 2.2) which is presented in Fig. 4.2 **d-f**. Previous STS experiments on various metallic substrates reported HOMO, LUMO, and LUMO+1 G^{∂} positions between $-1.9\,\mathrm{V} \leq V_{\mathrm{HOMO}} \leq -1.7\,\mathrm{V}$, $0\,\mathrm{V} \leq V_{\mathrm{LUMO}} \leq 1.1\,\mathrm{V}$, and $1.7\,\mathrm{V} \leq V_{\mathrm{LUMO+1}} \leq 2.8\,\mathrm{V}$, respectively (cf. Tab. A.2)[132,135,138,142,152–160]. Thus, the three main features visible in Fig. 4.2 **d-f** may be assigned to the HOMO (orange bar), LUMO (light blue bar), and LUMO+1 (violet bar) resonances.

Alternatively, peaks may originate from splitting of the orbitals. Previously, split LUMO resonances were observed with a splitting of 0.4 eV on Ag(110)[135] and 0.6 eV on Cu(111)[153]. The presumed LUMO and LUMO+1 peaks in Fig. 4.2 are separated by 0.76 V (**a**), 0.73 V (**b**), and 1.54 V (**c**). A large splitting requires a strong coupling to the substrate. C_{60}/NbO features a rather high Υ, which amounts to $2.63 \pm 0.21\,\mathrm{V}$ (Fig. 4.2 **g**). A large Υ indicates weak coupling, which would be inconsistent with split resonances thus strengthening the interpretation of the three peaks in Fig. 4.2 **d-f** as HOMO, LUMO, and LUMO+1.

The large scattering of Υ reflects the topographic heterogeneity. Virtually every molecule is subject to its unique geometric and thus electronic environment leading to a continuous distribution of DOS features (Fig. 4.2 **g**).

4.2. Proximity-Induced Superconductivity in Single C_{60} Molecules

In order to examine the superconducting properties of the NbO surface as well as adsorbed C_{60} molecules, spectroscopy of W–NbO and W–C_{60} junctions was performed in the tunneling regime. A depression at $V = 0$ is visible in Fig. 4.3 **a,b**. With increasing temperature, the depth as well as width of the depression decreases. The data were fit using the BCS expression [eq. (2.4)] as sample DOS ϱ_{s} multiplied with a quadratic background $1 + a^{(1)}V + a^{(2)}V^2$. Temperature [eq. (2.15)] and Lock-In [eq. (2.24)] broadening were considered using variable T_{t} and the experimentally applied $V_{\mathrm{m}} = 250\,\mu\mathrm{V_{RMS}}$. The fits (red lines in Fig. 4.3 **a,b**) are in good agreement with the experimental data. The resulting fit values for the energy gap Δ is shown in Fig. 4.3 **c,d** as a function of the readout of the temperature diode, T_{Diode}. For temperatures $8.5\,\mathrm{K} \lesssim T \lesssim 9.5\,\mathrm{K}$, pronounced thermal drift of the system prevented the acquisition of G^{∂} data without significant slope. The total disappearance of the energy gap is indicated as data at $\Delta = 0$. For both junction types, Δ decreases monotonically with T in a similar fashion. The BCS prediction of the $\Delta(T)$ progression according to eq. (2.5) was then fit to the experimental data (solid lines in Fig. 4.3 **c,d**). The resulting fit parameter for the energy gap at zero temperature Δ_0 and critical temperature T_{c} are given in Tab. 4.1. The results are in good agreement with values reported for bulk Nb [$T_{\mathrm{c}} = 9.25\,\mathrm{K}$ (ref. 111–115), $\Delta_0 = 1.52\,\mathrm{meV}$ (ref. 116,117)]. Moreover, the consistence with bulk values indicates that the SPE is fully operative in NbO as well as single C_{60} molecules on NbO.

	Δ_0 (meV)	T_{c} (K)
W-NbO	1.52 ± 0.01	9.21 ± 0.05
W-C_{60}	1.54 ± 0.02	9.20 ± 0.12

Table 4.1. Result of the BCS fits.

The fit temperature T_{t}, which reflects the temperature of the tip [eq. (2.15)], matches T_{Diode} for $T_{\mathrm{Diode}} \lesssim 7\,\mathrm{K}$. At higher values, T_{t} falls short of T_{Diode}. This finding reflects the geometric arrangement of the experimental setup. The heating diode is located in close proximity to the

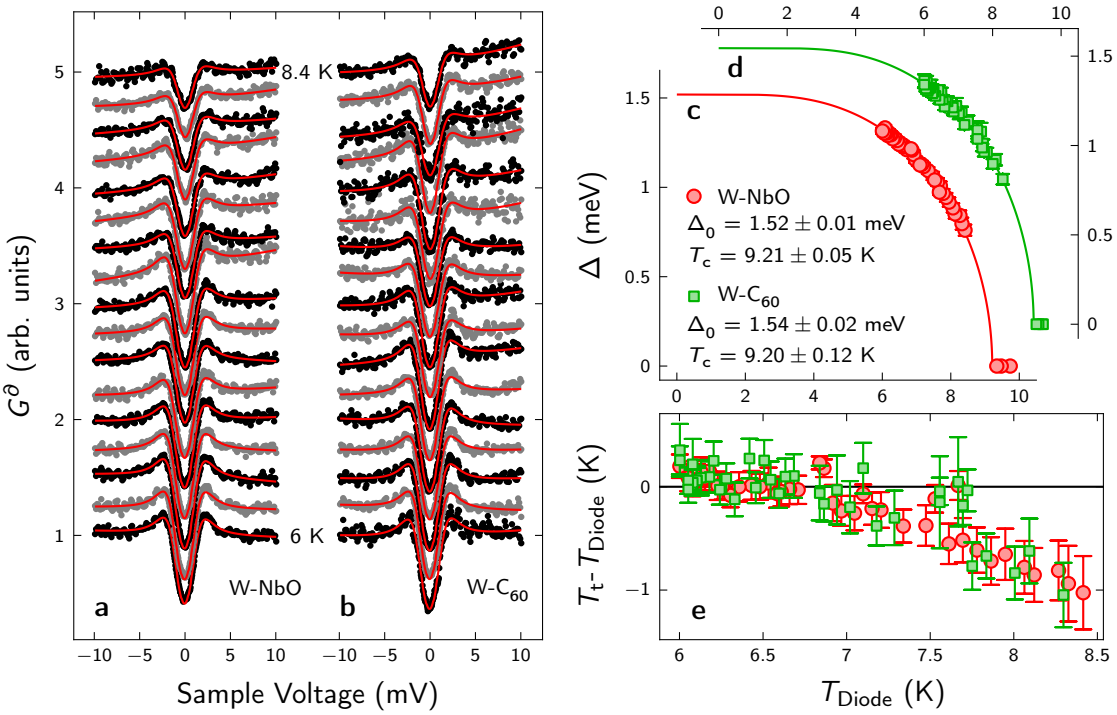

Figure 4.3. **a,b**, Differential conductance G^{∂} (dots) recorded for W-NbO (**a**) and W-C_{60} junctions (**b**) between 6 K (bottom) and 8.4 K (top). The data have been normalized to G^{∂} ($|V| = 10$ mV) and vertically offset with increasing temperature. Red lines denote BCS fits to the data. **c,d**, Δ extracted from BCS fits for W-NbO (**c**, red circles) and W-C_{60} junctions (**d**, green squares) as a function of the temperature readout of the Lake Shore diode T_{Diode}. Solid lines represent fits according to the BCS prediction. Fit values for the zero temperature gap Δ_0 and critical temperature T_c are indicated in the figure. **e**, Deviation of the BCS tip temperature T_t from T_{Diode} for W-NbO (red) and W-C_{60} junctions (green) as a function of T_{Diode}. Markers (error bars) in **c–e** present the parameter estimates (95% uncertainty intervals) obtained from least squares fits. The feedback has been disabled at 20 mV, 0.5 nA and a Lock-In modulation $V_m = 150\,\mu V_{\mathrm{RMS}}$ was applied.

sample and only connected to the tip slider via the piezo plates for $x - y$ coarse movement. Thus, thermal coupling between tip and diode is lower than between tip and cryostat and heating predominantly increases the sample temperature.

4.3. Andreev Reflection Spectroscopy of Single C_{60}-Contacts

In addition to the tunneling spectroscopy described above G^{∂} data in the same bias range were acquired for decreasing tip–sample distance. Fig. 4.4 exhibits data for W–NbO (**a**), C_{60}–NbO (**b**), and W–C_{60} (**c**) contacts. With increasing conductance the superconducting energy gap depth decreases and a zero-bias peak emerges. The data conform with the progression expected for AR (cf. Fig. 2.7).

Analogous to the BCS fit described in the previous section, the BTK expression of G^{∂} [eq. (2.36)] was fit to the data considering thermal as well as modulation broadening and a quadratic background. The resulting traces (solid lines in Fig. 4.4) are in good agreement with the experimental

data. The BTK fits yield fit parameters Δ, T_t, and the BTK transmission τ for each curve.

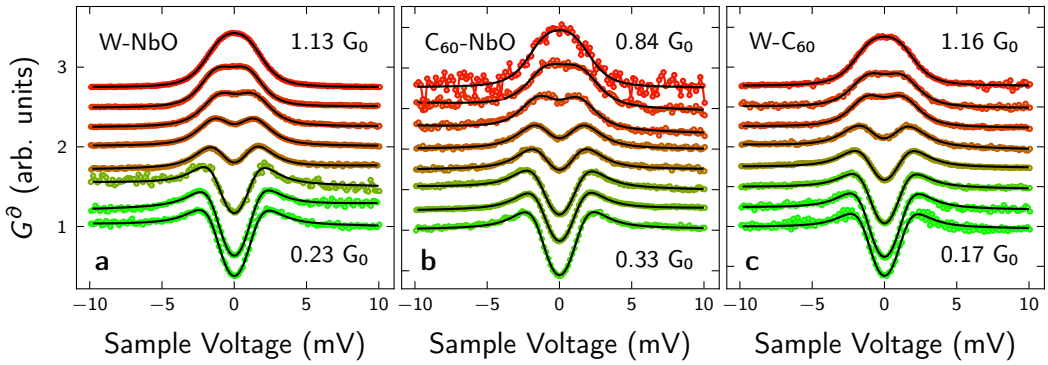

Figure 4.4. Differential conductance (G^∂, circles) traces recorded for W-NbO (**a**), C_{60}-NbO (**b**), and W-C_{60} junctions (**c**) at 6 K. The data are normalized by dividing with G_n^∂, vertically offset, and color-coded with the transmission τ extracted from the BTK fits ranging from $\tau = 0$ (green) to $\tau = 1$ (red). Solid black lines represent BTK fits to the data. The feedback has been disabled at 20 mV, 0.5 nA with an additional piezo displacement applied prior to spectroscopy. A Lock-In modulation $V_m = 150\,\mu V_{RMS}$ was used.

Conductance-vs-distance data of a contact between the pristine W tip and a Nb atom at the center of a Nb chain are presented in Fig. 4.5. The trace is in agreement with previous reports of metal–adatom contacts such as Ag/Ag(111), Cu/Cu(111), and Co/Cu(100)[161–165]. The evolution of G with z can be divided in three regimes. For $z \lesssim 480$ pm, G increases exponentially reflecting quantum tunneling (cf. red fit line in Fig. 4.5). Between 480 pm $\lesssim z \lesssim$ 510 pm, the slope of $G(z)$ increases since atomic scale relaxations reduce the actual tip–adatom separation (cf. green fit). The reduction originates from the presence of strong attractive forces and the elasticity of the electrodes[164]. This range is commonly referred to as transition regime. For large $z \gtrsim 510$ pm, chemical contact is formed which is accompanied by an almost constant conductance (contact regime). A further tip approach leads to orbital deformation, which marginally increases the conductance (cf. blue fit line in Fig. 4.5).

BTK fits to G^∂ data acquired at z corresponding to the colored circles in Fig. 4.5 yield values for the BTK transmission τ, a measure related to the tunneling barrier strength. Tunneling ranges are characterized by low values $\tau \leqslant 0.2$, while the contact regime corresponds to $\tau \geqslant 0.9$. The spectra at $z = 515$ pm corresponds to $\tau = 0.9$, which is lower than the value of $\tau = 1$ expected for a perfect, ballistic point contact. Two effects might contribute to this deviation in addition to the possibility, that chemical contact is not fully developed at this point. First, the presence of more than a single transport channel reduces the τ value obtained from a BTK fit (see below). Second, a mismatch between the Fermi velocities of tip $v_F^{(t)}$ and sample $v_F^{(s)}$ is contrary to the assumption of equal momenta in $\mathcal{N}$ and $\mathcal{S}$, which the BTK approach is based on. Hence, an additional, effective barrier emerges, which can be incorporated into BTK theory[100,166] by replacing

$$Z \to Z_{eff} = \sqrt{Z^2 + (1-\xi)^2/4\xi} \tag{4.1}$$

ξ represents the ratio of v_F, $\xi = v_F^{(s)}/v_F^{(t)}$. The Fermi velocities of W and Nb are $v_F^W = 0.97 \cdot 10^6$ m/s (ref. 167) and $v_F^{Nb} = 1.37 \cdot 10^6$ m/s (ref. 168), respectively. Consequently, $\xi = 1.41$ which yields a minimum $Z_{eff} \geqslant \sqrt{(1-\xi)^2/4\xi} = 0.17$ and corresponding maximum $\tau_{eff} \leqslant (1+Z_{eff}^2)^{-1} = 0.97$.

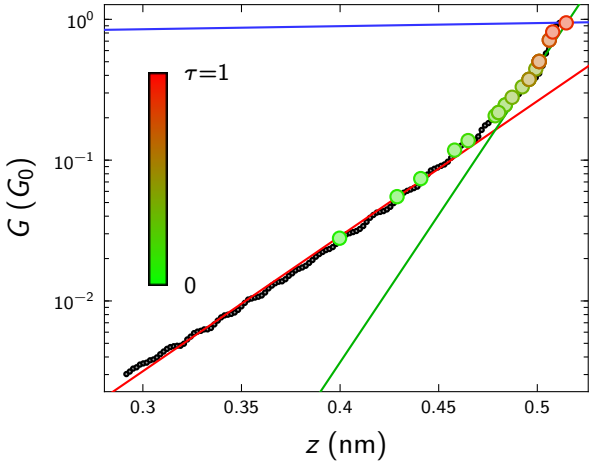

Figure 4.5. Conductance (black) of a W–NbO contact as a function of the tip displacement z. The feedback loop was disabled at 0.1 V, 0.1 nA, which corresponds to $z = 0$. Colored circles depict z positions, where G^{∂} spectra were recorded. The color of the circles represents the value of τ obtained from BTK fits according to the color scale on the top left. Red, green, and blue lines denote a simple exponential fit to the tunneling, transition, and contact regime, respectively.

According to BTK theory, the normal-state differential conductance, i.e., $G_n^{\partial} = G^{\partial}(|eV| \gg \Delta)$, increases linearly with τ. The linear dependence is experimentally confirmed for each data set, but the comparison of different sets reveals the existence of distinct subgroups for each junction type (Fig. 4.6 **a-c**). In order to identify the origin of the slope variations, the data were grouped according to their characteristic topographic fingerprints. Data for the subgroups are depicted by different colors and labeled 𝔄-𝔊. Each subgroup is distinguished by its unique slope (lines in Fig. 4.6 **a-c**). The linear relation $\tau = \mathfrak{s} \cdot G_n^{\partial}$ was fit to the data yielding slope values $\mathfrak{s}$ according to Fig. 4.6 **d-f**.

An exemplary topographic image for each subgroup is displayed in Fig. 4.7. W-NbO junctions appear with two distinct topographic fingerprints (Fig. 4.7 **a,b**). Tips used to obtain 𝔄 data

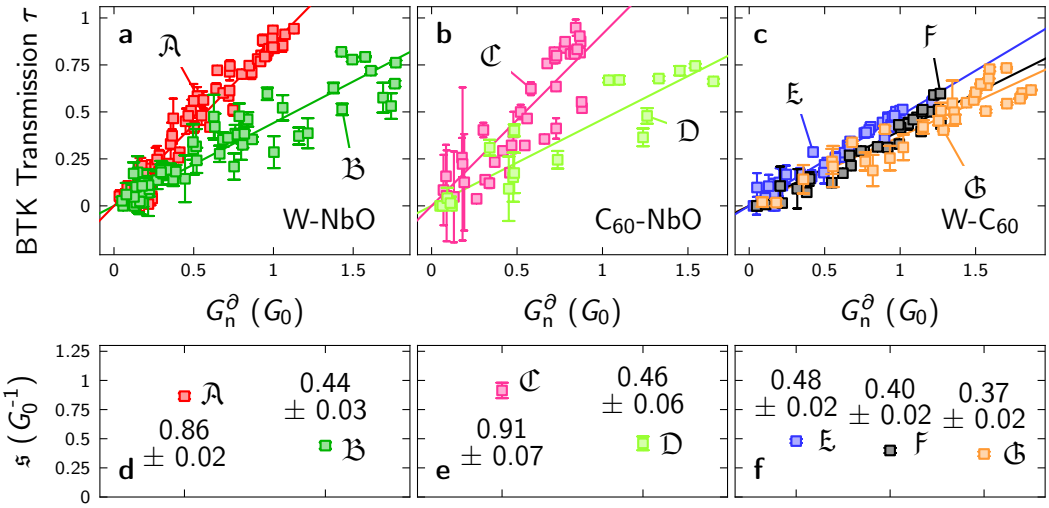

Figure 4.6. Evaluation of the BTK fits. **a-c**, BTK transmission τ (squares) as a function of normal-state differential conductance G_n^{∂} for W-NbO (**a**), C_{60}–NbO (**b**), and W-C_{60} junctions (**c**). Different junction subtypes are indicated with different color and accompanied by a linear fit (solid line). **d-f**, Slope of the linear fits. Data for the same junction subtypes are displayed with the same color and labeled 𝔄-𝔊. Markers (error bars) present the parameter estimates (95% uncertainty intervals) obtained from least squares fits.

exhibit the Nb chains with high resolution revealing the position of each atom (Fig. 4.7 **a**). This is contrasted by $\mathfrak{B}$ tips, where atomic resolution did not occur (Fig. 4.7 **b**). The linear slope of τ for $\mathfrak{A}$ is 1.95 times higher than for $\mathfrak{B}$ ($0.86 \pm 0.02\,G_0^{-1}$ compared to $0.44 \pm 0.03\,G_0^{-1}$, Fig. 4.7 **d**). A slope doubling implies a doubled normal-state differential conductance G_n^∂ for equal τ. Examining eq. (2.36) reveals the effective tunneling area $\mathscr{A}$ as only variable that may deviate by a factor of 2. The doubling of $\mathscr{A}$ can be rationalized by considering the tip termination. While tips terminated by a single atom lead to lower G_n^∂ and atomic resolution, two atoms at the tip apex yield higher G_n^∂ but reduced spatial resolution. This interpretation is strengthened by the enhanced scattering for $\mathfrak{B}$ in Fig. 4.6 **a**. During the course of the present experiments, the STM tip apex was repeatedly modified by small contacts with the surface, which resulted in either transfer of tip material to the surface or recrystallization of the tip apex. Here, tip apices are not expected to recrystallize with perfect crystalline order yielding different apex geometries (microtips). Different $\mathfrak{B}$ microtips may be terminated by two atoms that are not located with perfectly equal distance to the surface. Thus, the differential conductance is not exactly doubled. Similarly, a doubled contact conductance has been reported for diatomic compared to monoatomic clusters[133].

A topographic image revealing the origin of the different $\mathfrak{s}$ values for C_{60}-NbO junctions is presented in Fig. 4.7 **c**. $\mathfrak{C}$ and $\mathfrak{D}$ correspond to data acquired on top of an atom close to the center of a Nb chain and in the trench between two chains, respectively. The slope for $\mathfrak{C}$, enhanced by a factor of 1.98 with respect to $\mathfrak{D}$, indicates a doubling of the effective tunneling area $\mathscr{A}$ for trench contacts, where two chains contribute to the conductance.

W–C_{60} junctions (Fig. 4.6 **c,f**) exhibited three less distinct slopes of $0.48 \pm 0.02\,G_0^{-1}$ ($\mathfrak{E}$), $0.40 \pm 0.02\,G_0^{-1}$ ($\mathfrak{F}$), and $0.37 \pm 0.02\,G_0^{-1}$ ($\mathfrak{G}$). The C_{60} molecules contributing to Fig. 4.6 **c** exhibit different submolecular motifs. $\mathfrak{E}$ molecules feature three equidistant protrusions in STM images

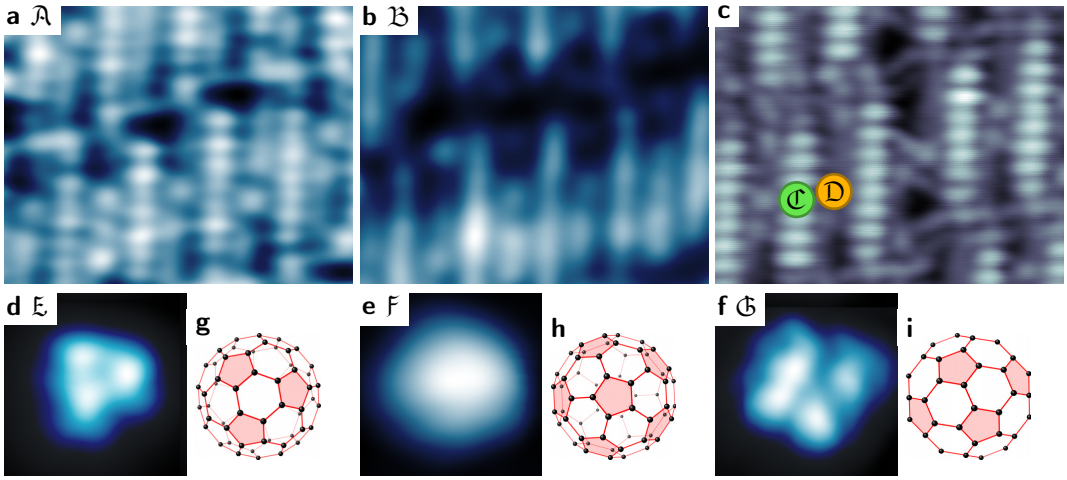

Figure 4.7. Constant-current topography corresponding to the different junctions $\mathfrak{A}$-$\mathfrak{G}$ introduced in Fig. 4.6. **a-c**, Topography of NbO and **d-f**, C_{60}/NbO obtained with a W (**a,b,d-f**) and C_{60}-terminated W tip (**c**). **g-i**, Sketch of different orientations of the C_{60} molecules inferred from **d-f**. Red areas highlight C pentagons. Imaging parameters are **a-d,f**, 0.1 V, 0.1 nA and **e**, 1.9 V, 0.1 nA. A 10 pt (5 pt) Gaussian filter was applied to **a,d-f** (**b**). 40 % and 50 % of the second derivative were substracted from **d** and **f**, respectively.

(Fig. 4.7 **d**). This appearance is consistent with a hexagon oriented toward the tip (**6**-C_{60}). The spatial distribution of a C_{60} LUMO is concentrated atop C pentagons presenting toroidal features of high charge density[134]. The three LUMOs predominantly contributing to the tunneling current at 0.1 V are located at the corners of a triangle around a C hexagon (red areas in Fig. 4.7 **g**). In STM images, C_{60} molecules with a hexagon oriented toward the vacuum appear with trefoil-like motifs resembling Fig. 4.7 **d**[135,138,142,152,153,155,160]. $\mathfrak{F}$ molecules exhibit a single protrusion that at closer look appears with a slight 5-fold symmetry (Fig. 4.7 **e**). The LUMOs of C_{60} molecules exposing a pentagon to the vacuum (**5**-C_{60}) arrange in this fashion, with a single orbital at the center that is accompanied by five symmetrically positioned orbitals (Fig. 4.7 **h**). C_{60} molecules with similar appearance were previously assigned to **5**-C_{60} as well[153,155]. $\mathfrak{G}$ C_{60} molecules feature four-fold symmetric motifs (Fig. 4.7 **f**). This appearance is consistent with a hexagon-hexagon-bond (**6**-**6**-C_{60}) exposed to the vacuum (Fig. 4.7 **i**). Commonly, **6**-**6**-C_{60} molecules appear with two-fold symmetry and only minor contributions of the two orbitals located at the left and right of Fig. 4.7 **i**[135,138,152]. The protrusions visible in Fig. 4.7 **f** indicate either a slight rotation of the molecule or a non-negligible contribution of the HOMO. The spatial distribution of a **6**-**6**-C_{60} HOMO has a perfectly four-fold symmetric component[134]. The decay of the HOMO (Fig. 4.3 **a**-**c**) indicates a possible contribution of the HOMO to the tunneling current at 0.1 V.

At constant τ, the orientations present differential conductances increasing in the order **6**-**6** $\rightarrow$ **5** $\rightarrow$ **6**. Previously, conductances beyond the point of contact were reported in the same sequence[138]. Possibly, the variation observed here occurs due to differences in the effective tunneling area for different orientations. However, a recent experiment examining electron transport through C_{60} with two superconducting electrodes revealed the orientation-dependence of the transmission coefficients[169]. In order to unravel the impact of transmission through more than a single channel, *ab initio* transport calculations were employed in collaboration with Pedro Ribeiro and Stefan Kirchner[110]. The contacts were modeled using one normal-conducting ($\mathcal{N}$) and one superconducting ($\mathcal{S}$) electrode as well as a single-level quantum dot $\mathcal{M}$ representing the molecule. The energy level of $\mathcal{M}$ is separated from the equilibrium Fermi level E_F of $\mathcal{N}$ and $\mathcal{S}$ by $\epsilon_\mathcal{M}$. The coupling of $\mathcal{M}$ to the electrodes is incorporated via the hybridization energies $\Gamma_{\mathcal{N},\mathcal{S}}$. The latter are connected to the hopping amplitudes from $\mathcal{M}$ to $\mathcal{N}$ ($\mathrm{t}_\mathcal{N}$) and $\mathcal{M}$ to $\mathcal{S}$ ($\mathrm{t}_\mathcal{S}$) via the relations

$$\Gamma_\mathcal{N} = \pi\, \mathrm{t}_\mathcal{N}^2\, \varrho_\mathcal{N}(E_\mathrm{F}) \qquad \text{and} \qquad \Gamma_\mathcal{S} = \pi\, \mathrm{t}_\mathcal{S}^2\, \varrho_\mathcal{S}(E_\mathrm{F}) \tag{4.2}$$

For strong hybridization with either electrode, i.e., $\Gamma_\mathcal{S} \gg \Delta, \epsilon_\mathcal{M}, \mathrm{e}V$ or $\Gamma_\mathcal{N} \gg \Delta, \epsilon_\mathcal{M}, \mathrm{e}V$, the BTK formalism, e.g., eq. (2.36), is rendered valid with Z being a function of the hybridization energies[110],

$$Z = \frac{|\Gamma_\mathcal{S} - \Gamma_\mathcal{N}|}{\sqrt{2\Gamma_\mathcal{S}\Gamma_\mathcal{N}}} \tag{4.3}$$

BTK theory was developed for macroscopic point contacts, which considers a delta potential barrier of height $\mathscr{H} = \hbar v_\mathrm{F} Z$ representing the tunneling barrier. Eq. (4.3) establishes a connection between the tunneling barrier and the coupling of a single molecule to the contacting electrodes.

In the following, a strong hybridization with $\mathcal{S}$, i.e., $\Gamma_\mathcal{S} = 10\Delta$, is considered. Two parallel transport channels, α and β, are regarded with hybridization energies $\Gamma_\mathcal{N}^{(\alpha,\beta)}$. The transmission of each channel, $\tau_{\alpha,\beta}$, is obtained using eqs. (2.37), (4.3). Fig. 4.8 **a**-**d** presents G^∂ data using

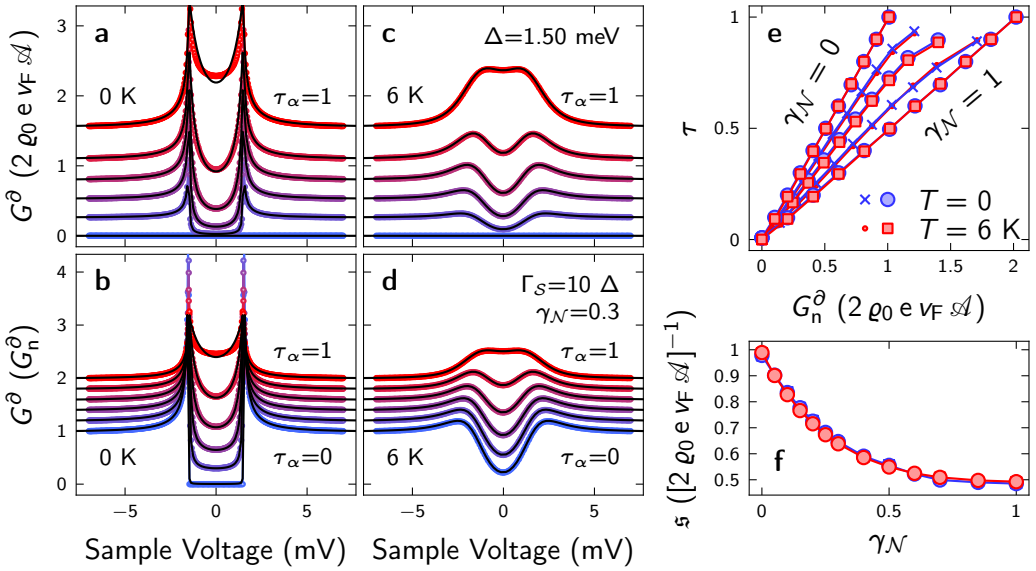

Figure 4.8. Theoretical modeling of a two-channel BTK system. **a-d**, Differential conductance G^∂ (colored) at 0 K (**a,b**) and 6 K (**c-d**) for $\Gamma_S = 10\Delta$, $\gamma_N = 0.3$, $\Delta = 1.5$ meV, and different transmission values $0 \leq \tau_\alpha \leq 1$. G^∂ data are color-coded ranging from $\tau_\alpha = 0$ (blue) to $\tau_\alpha = 1$ (red). A single-channel BTK fit is shown in black. G^∂ in **b,d** is normalized to G^∂ in the normal state G_n^∂ and vertically shifted consecutively. **e**, Evaluation of the single-channel BTK transmission τ as a function of G_n^∂ at 0 K (blue) and 6 K (red). Values of γ_N are (from top to bottom) 0, 0.1, 0.2, 0.4, 1. **f**, $\mathfrak{s}$ obtained from linear fits to the $\tau(G_n^\partial)$ data of **e** for $\tau \leq 0.7$ as a function of coupling ratio γ_N.

the coupling ratio $\gamma_N = \Gamma_N^{(\beta)}/\Gamma_N^{(\alpha)} = 0.3$ (colored dots). At $T = 0$, a single-channel BTK fit does not reproduce the data at elevated τ_α (solid black lines in Fig. 4.8 **a,b**). This observation is contrasted by the thermally broadened ($T = 6$ K) data (Fig. 4.8 **c,d**), that are well represented by a single-channel BTK fit. At temperatures as low as $T \lesssim 0.05\,T_c$ data obtained within the two-channel model can be matched well by single-channel BTK fits[110].

Fig. 4.8 **e** shows the variation of the transparency τ obtained from single-channel BTK fits to two-channel data with different coupling ratio γ_N. With γ_N increasing from 0 to 1, the slope decreases progressively until it reaches 50% of the value for the single-channel result. Fig. 4.8 **f** presents the slopes of $\tau(G_n^\partial)$, $\mathfrak{s}$, as a function of γ_N. The decreasing trend symbolizes the increasing differential conductance for increasing coupling of the second channel. Interestingly, the single-channel transparency is independent of temperature. This result is rather surprising, since the agreement of the fits is considerably lower at $T = 0$.

The data presented in Fig. 4.8 **e,f** indicate a possible contribution of the transmission coefficients $\mathcal{T}_i$ of the transport channels on the experimental $\mathfrak{s}$ values. The orientation-dependence of $\mathcal{T}_i$ previously observed for C_{60} on Pb(111)[169] may contribute to the different slopes observed in the experimental data (cf. Fig. 4.6 **a-c**).

The lower bound of the number of transmission channels n can be inferred from $\tau(G_n^\partial)$ data. Ballistic transport occurs with a conductance of $1\,G_0$ for each fully transmitting conductance channel[170–172]. Therefore, the value of G_n^∂ at the extrapolation of $\tau(G_n^\partial)$ data to $\tau(\hat{G}_n^\partial) = 1$ must satisfy the relation

$$\hat{G}_{\mathrm{n}}^{\partial} = \mathfrak{s}^{-1} \leqslant n\,G_0 \tag{4.4}$$

The data shown in Fig. 4.6 **a-c** evidence that $n \geqslant 2$ ($\mathfrak{A}$, $\mathfrak{C}$) and $n \geqslant 3$ ($\mathfrak{B}$, $\mathfrak{D}$–$\mathfrak{G}$) transport channels contribute to electron transport across the respective interface.

The fit parameters Δ and T_{t} obtained from the single-channel BTK fits to the experimental data are displayed in Fig. 4.9 as a function of τ. Within their respective standard deviations, the mean Δ and T_{t} for the different subgroups do not deviate markedly (Tab. 4.2). However, the mean gap values exceed those obtained from BCS fits, i.e., 1.32 ± 0.01 meV at 6.06 ± 0.04 K and 1.34 ± 0.02 meV at 6.04 ± 0.03 K for W–NbO and W–C_{60} junctions, respectively. While T_{t} at lower τ matches the temperature measured with the temperature diode, 6.02 ± 0.03 K, it increases with τ with a slope of 1.15 ± 0.13 K.

Several contributions to these discrepancies may occur. First, especially at elevated T the fit parameters Δ, T_{t}, and τ are becoming increasingly dependent of each other. Moreover, the existence of multiple channels contributes to T_{t} increasing with τ. The single-channel fit of the two-channel data shown in Fig. 4.8 **a-d** yielded a slope of 0.24 ± 0.04 K. Furthermore, some assumptions for the BTK model are not perfectly valid. In the following, several arguments previously elaborated by Lukic are briefly summarized[166]. Considering a finite gap onset yields a reduced differential conductance inside the gap, which becomes relevant at high τ. In BTK, all momenta k are set to the Fermi momentum neglecting the energy dependence of k. Including the exact moment leads to a shift of spectral weight from above to below Δ. Due to the conservation of $k_{\parallel}$ and the lower k of holes compared to electrons, the AR hole is not perfectly retroreflected. This results in a slight reduction of differential conductance inside the gap. The angle-dependence of the tunneling barrier is not included, which overestimates G below as well as above the gap.

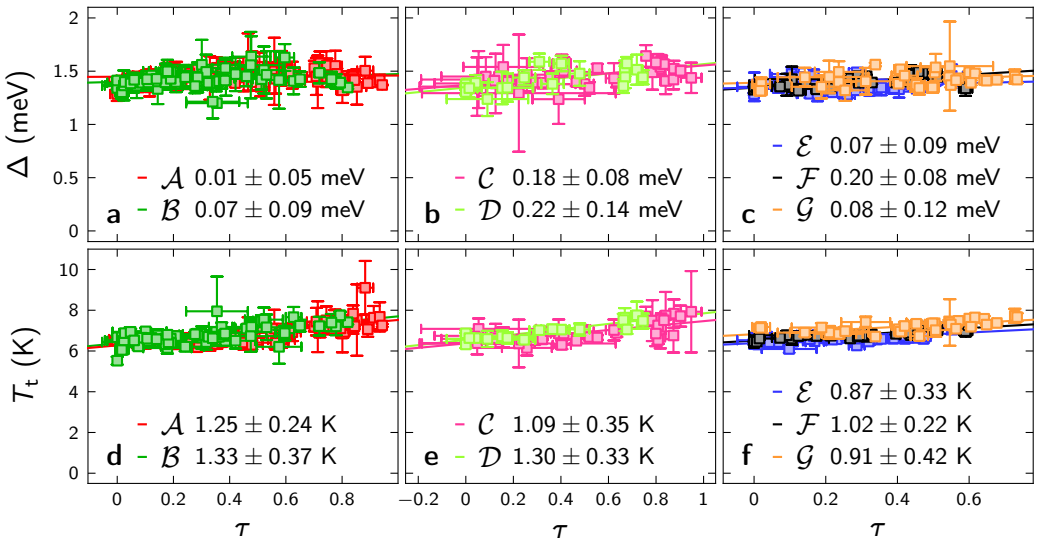

Figure 4.9. Evaluation of the BTK fits (II). Δ (squares in **a-c**) and T_{t} (squares in **d-f**) as a function of normal-state differential conductance $G_{\mathrm{n}}^{\partial}$ for W-NbO (**a,d**), C_{60}-NbO (**b,e**), and W-C_{60} junctions (**c,f**). Solid lines indicate a linear fit to the data. Coloring is consistent with Fig. 4.6. The slopes of Δ and T_{t} are indicated at the bottom of each panel. Markers (error bars) present the parameter estimates (95% uncertainty intervals) obtained from least squares fits.

		Δ (meV)	T_t (K)	$\partial_\tau \Delta$ (meV)	$\partial_\tau T_t$ (K)	$\mathfrak{s}$ (G_0^{-1})
W-NbO	$\mathfrak{A}$	1.46 ± 0.06	6.24 ± 0.21	$+0.01 \pm 0.05$	$+1.25 \pm 0.24$	$+0.86 \pm 0.02$
	$\mathfrak{B}$	1.41 ± 0.07	6.40 ± 0.29	$+0.07 \pm 0.09$	$+1.33 \pm 0.37$	$+0.44 \pm 0.03$
C_{60}-NbO	$\mathfrak{C}$	1.37 ± 0.08	6.31 ± 0.22	$+0.18 \pm 0.08$	$+1.09 \pm 0.35$	$+0.91 \pm 0.07$
	$\mathfrak{D}$	1.37 ± 0.11	6.56 ± 0.22	$+0.22 \pm 0.14$	$+1.30 \pm 0.33$	$+0.46 \pm 0.06$
W-C_{60}	$\mathfrak{E}$	1.36 ± 0.07	6.37 ± 0.18	$+0.07 \pm 0.09$	$+0.87 \pm 0.33$	$+0.48 \pm 0.02$
	$\mathfrak{F}$	1.34 ± 0.03	6.45 ± 0.15	$+0.20 \pm 0.08$	$+1.02 \pm 0.22$	$+0.40 \pm 0.02$
	$\mathfrak{G}$	1.41 ± 0.06	6.76 ± 0.15	$+0.08 \pm 0.12$	$+0.91 \pm 0.42$	$+0.37 \pm 0.02$
all		1.43 ± 0.08	6.87 ± 0.43	$+0.12 \pm 0.03$	$+1.15 \pm 0.13$	$+0.53 \pm 0.03$
W-NbO		1.44 ± 0.07	6.83 ± 0.47	$+0.04 \pm 0.04$	$+1.21 \pm 0.19$	$+0.61 \pm 0.04$
W-C_{60}		1.40 ± 0.06	6.86 ± 0.35	$+0.14 \pm 0.06$	$+1.25 \pm 0.25$	$+0.40 \pm 0.01$
C_{60}-NbO		1.45 ± 0.10	6.95 ± 0.45	$+0.20 \pm 0.07$	$+1.04 \pm 0.27$	$+0.69 \pm 0.07$

Table 4.2. Evaluation of the BTK fits. The 3rd and 4th column give mean values and standard deviation of Δ and T_t respectively. The 5th, 6th, and 7th column present the linear slopes of Δ and T_t as a function of τ as well as of τ as a function of the normal-state differential conductance, $\mathfrak{s}$, with their respective fit uncertainty.

Additionally, the finite quasi-particle lifetime[67,68] introduces additional broadening. Further, the coupling between $\mathcal{M}$ and $\mathcal{S}$, $\Gamma_\mathcal{S}$, may be altered with decreasing tip–sample distance due to atomic-scale relaxations caused by attractive forces between tip and molecule. Finally, an energy-dependent ϱ background may impact the accuracy of the fit result. No correlation between orientation and slope of G^∂ at $V = 0$ was observed in spectroscopy probing a larger bias range in the tunneling regime (such as Fig. 4.2). However, a previous examination of C_{60} molecules on Cu(100) revealed a dependence of the orientation on the G^∂ progression around zero bias at close tip approach[138].

Scrutinizing the Fit Results

Fig. 4.9 and Tab. 4.2 reveal, that the mean values of the fit parameters Δ and T_t differ between subtypes. Hence, the results for τ and consequently $\mathfrak{s}$ might be distorted by systematic deviations of Δ and T_t. In order to examine a possible influence of Δ and T_t on τ and $\mathfrak{s}$ obtained from BTK fits, G^∂ data were calculated within the two-channel model. Since variations of $\mathfrak{s}$ for W-C_{60} contacts ($\mathfrak{E}$, $\mathfrak{F}$, and $\mathfrak{G}$) are significantly lower than for W-NbO and C_{60}-NbO contacts, the impact of fit parameter variations for $\mathfrak{E}$, $\mathfrak{F}$, and $\mathfrak{G}$ data are examined in the following. Input parameters for the calculations are taken from the averages of $\mathfrak{E}$, $\mathfrak{F}$, and $\mathfrak{G}$, i.e., $\langle \Delta^{\mathfrak{E},\mathfrak{F},\mathfrak{G}} \rangle = 1.37\,\text{meV}$ and $\langle T_t^{\mathfrak{E},\mathfrak{F},\mathfrak{G}} \rangle = 6.5\,\text{K}$. $\gamma_\mathcal{N} = 0.6$ is chosen. $G^\partial(\tau_\alpha)$ data were calculated for $0 \leq \tau_\alpha \leq 1$. Then, three single channel fits were performed for each $G^\partial(\tau_\alpha)$ trace with fit boundaries

$$\Delta^{(\text{bound},\mathfrak{X})} = \langle \Delta^{\mathfrak{X}} \rangle \pm \delta\Delta \qquad \text{and} \qquad T_t^{(\text{bound},\mathfrak{X})} = \langle T_t^{\mathfrak{X}} \rangle \pm \delta T_t \qquad (4.5)$$

$$\mathfrak{X} \in \{\mathfrak{E}, \mathfrak{F}, \mathfrak{G}\}$$

$\langle \Delta^{\mathfrak{E}} \rangle$ and $\langle T_t^{\mathfrak{E}} \rangle$ denote the mean values of Δ and T_t, respectively, for $\mathfrak{E}$ data. $\delta\Delta = 0.004\,\text{meV}$ and $\delta T_t = 0.02\,\text{K}$ were chosen in order to separate fit ranges.

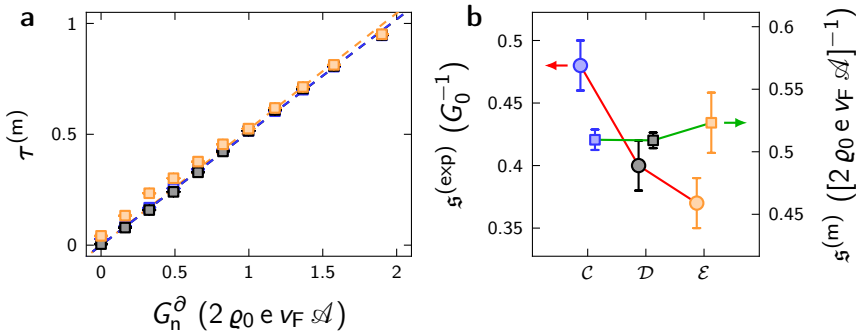

Figure 4.10. Fit results of a single-channel BTK fit for a two-channel model input. **a**, BTK transmission for the fit to the model $\tau^{(m)}$ as a function of G_n^{∂}. **b**, $\mathfrak{s}^{(m)}$ for the different subgroups obtained from the model (squares, green line, right axis) and comparison with experimental fit values ($\mathfrak{s}^{(exp)}$, circles, red line, left axis). The input parameters of the model were the mean values of Tab. 4.2 for W-C_{60} junctions, i.e., $\Delta = 1.37$ meV, $T_t = 6.5$ K, and setting $\gamma_N = 0.6$. The fit boundaries were chosen to [1.358,1.362] meV, [6.36,6.38] K ($\mathcal{C}$), [1.338,1.342] meV, [6.44,6.46] K ($\mathcal{D}$), and [1.408,1.412] meV, [6.75,6.77] K ($\mathcal{E}$). Markers (error bars) present the parameter estimates (95% uncertainty intervals) obtained from least squares fits.

Fig. 4.10 **a** presents the resulting fit parameter $\tau^{(m)}$. Noticeably, deviations for the different fit boundaries occurred only at low G_n^{∂} in contrast to the experimental observations. The slope of $\tau^{(m)}$ obtained from linear fits of Fig. 4.10 **a**, $\mathfrak{s}^{(m)}$, reveals a slight increase from $\mathfrak{E}$ to $\mathfrak{G}$ (squares in Fig. 4.10 **b**). This finding is contrary to the trend observed in the experimental data, which shows a significant decrease from $\mathfrak{E}$ to $\mathfrak{G}$ (circles in Fig. 4.10 **b**). Likewise, accounting for T_t increasing with τ did not reproduce the declining trend. Consequently, the experimentally observed differences of $\mathfrak{s}$ do not originate from systematic deviations of Δ and T_t.

4.4. Conclusion

Superconductivity of single C_{60}-junctions on NbO/Nb(110) was investigated in an STM/STS experiment. The superconducting energy gap determined from spectra obtained atop the molecules matches that of the plain surface as well as previously reported values for bulk Nb, indicating that the superconducting proximity effect is fully operative. Progressively approaching the tip to the NbO surface and single C_{60} molecules was accompanied by an increase in AR probability, revealed by the gradual transformation of the depression caused by the superconducting energy gap into a single zero-bias peak. The impact of the atomic-scale geometry as well as the orientation of the C_{60} was unraveled by analysis using the BTK model. The experimental data and multiple-channel systems in general are reproduced well within BTK theory due to finite temperature and strong molecule–electrode hybridization. Considering multiple transport channels qualitatively reproduces the experimental observations and indicates an orientation-dependence of the transmission coefficients. A novel approach for the determination of the minimum number of transport channels is presented.

In subsequent work, the experimental method presented in this chapter was applied in the examination of magnetic MnPc molecules absorbed on a superconducting Pb(111) substrate by the group of the author. The results are published in Phys. Rev. B **97**, 195429 (2018), ref. 173.

Chapter 5

Vertical Force Spectroscopy of Single-C_{60} Contacts

Theoretical support for the present chapter was provided by ***Susanne Leitherer***, ***Nick P. Rübner***, *and* ***Mads Brandbyge*** *(Department of Micro- and Nanotechnology, Technical University of Denmark, Kgs. Lyngby, Denmark).*

Recent advances in scanning probe methods[38,58] enable the examination of chemical bonding at the atomic scale with increasing precision[17,132,133,138,139,163–165,174–186]. Appropriate experiments employ atomically sharp tips contacting single adatoms or molecules[17,132,133,138,139,163–165,180–186]. For nonpolar and nonmagnetic metals in vacuum, the tip–sample interaction is governed by long-range van-der-Waals and electrostatic as well as short-range Pauli forces. Decreasing tip–sample distances initially lead to increasing attraction caused by attractive van-der-Waals and electrostatic forces. After entering the short-range Pauli regime, the magnitude of the total force decreases and turns repulsive at further approach. Due to atomic-scale elasticity of the electrodes, the atoms of tip and sample relax thus reducing the real junction separation by up to $\sim$1 nm for metal tip–adatom[184] and metal tip–C_{60} (ref. 17) contacts. The junction deformation impacts the progression of the current I with distance z (ref. 17). Initially, I increases exponentially in accordance with quantum tunneling. Then, the increasing junction deformation entails a reduction of the actual tip–sample distance and consequently increases the slope of $I(z)$, $\partial_z I$ (transition regime). After surpassing the point of maximum attraction, the junction deformation is reversed, $\partial_z I$ decreases, and chemical contact emerges. The three distinguished ranges are commonly termed tunneling, transition, and contact regime, respectively.

In previous experiments, the point of chemical contact between a metal tip and a C_{60} molecule has been defined as the intersection of simple exponential extrapolations of the transition and contact regime in $I(z)$ data[132,133,180]. This point coincides with the point of maximum attractive force for metal-C_{60} contacts[17] implying maximum junction deformation. Recently, the conductance at contact, G_c, was examined as a function of the externally applied bias voltage V (ref. 186). $G_c(V)$ exhibited a distinct variation with V due to variations of the transmission coeffi-

cients. Although the variation of the z value at contact, z_c, was not included in the report, a significant, linear bias-dependence of z_c was observed in $G(z)$ data[18].

In this chapter, C_{60}-C_{60} contacts on Cu(111) are studied as a function of the externally applied bias voltage. C_{60}-C_{60} contacts exhibit significantly reduced forces as well as junction deformations compared to metal–C_{60} contacts[17]. Hence, the transition regime is not discernible and only a decrease of $\partial_z I$ occurs beyond the tunneling regime[17,132]. Due to the very high robustness of C_{60} molecules[180] and the reduced forces in such dimolecular junctions, C_{60}-C_{60} contacts present enhanced structural integrity and are thus promising candidates for the examination of $z_c(V)$ in AFM experiments. The latter requires the acquisition of several F_z traces over a large V range entailing a significant enhancement of electrostatic forces.

5.1. C_{60} Islands on Cu(111)

Fig. 5.1 introduces the experimental system used for the vertical spectroscopy experiments. C_{60} molecules on Cu(111) assemble predominantly at step edges in hexagonal arrays with a nearest-neighbor distance of 1.0 nm (Fig. 5.1 **a,b**). The submolecular structure at positive bias reflects the spatial distribution of the LUMOs. The latter present a torus-like shape centered at C pentagons. Thus, the trefoil-like pattern visible in Fig. 5.1 **c** conforms with a C hexagon oriented toward to vacuum[17,132,134].

C_{60} molecules were evaporated in two steps. Subsequent to the first and prior to the second evaporation, the sample was annealed at 400–500 K. Annealing of the C_{60}-covered surface leads to a reconstruction of the surface removing seven Cu atoms below each C_{60} molecule[187]. Thus, C_{60} molecules are lowered by $\sim$0.2 nm, i.e., embedded in the surface, resulting in enhanced coordination of C with Cu atoms. While unreconstructed C_{60} molecules ($\mathcal{U}$–C_{60}) exhibit a charge transfer of $\sim 0.8\,e^-/C_{60}$ from Cu(111) to each molecule, $\sim 3\,e^-/C_{60}$ are transferred to reconstructed C_{60} molecules ($\mathcal{R}$–C_{60})[187]. The LUMO is shifted from 0.75 V ($\mathcal{U}$–C_{60}) to 0 V ($\mathcal{R}$–C_{60})[187] while the LUMO+1 appears as shoulder at +1.4 V ($\mathcal{R}$–C_{60}) and above 1.8 V ($\mathcal{U}$–C_{60}) (cf. Fig. 5.1 **d**). The increase toward –1.5 V for both $\mathcal{U}$–C_{60} and $\mathcal{R}$–C_{60} is due to the onset of the HOMO resonance.

The difference of the LUMO position enables the identification of $\mathcal{U}$–C_{60} and $\mathcal{R}$–C_{60} by measuring the spatial distribution of G^∂ at 0.7 V (Fig. 5.1 **b**). $\mathcal{U}$–C_{60} molecules present a larger G^∂ at $\sim$0.7 V (Fig. 5.1 **d**) thus appearing with high intensity in Fig. 5.1 **b**. Three types of C_{60} molecules are visible in Fig. 5.1 **a,b**.

- $\mathcal{U}$–C_{60} on the lower terrace appear red in Fig. 5.1 **a,b**.
- $\mathcal{U}$–C_{60} on the upper terrace appear bright orange in Fig. 5.1 **a** and red in Fig. 5.1 **b**.
- $\mathcal{R}$–C_{60} embedded in the upper terrace appear red in Fig. 5.1 **a** and blue in Fig. 5.1 **b**.

C_{60}-terminated tips are obtained in the same manner as described in Sec. 4.1. Since G^∂ is determined by the convolution of ϱ_s with ϱ_t, the topography (Fig. 5.1 **e**) is clearly distinguishable from that obtained with metallic tips (Fig. 5.1 **c**). The lobes in Fig. 5.1 **e** appear broader than in Fig. 5.1 **c**. Fig. 5.1 **e** is most reminiscent of experimental[17,188] and theoretical[189] data of a hexagon of the C_{60}-terminated tip oriented toward the surface and imaging a C_{60} exposing a pentagon toward the tip. Hence, a pentagon of the C_{60}-terminated tip is most likely exposed

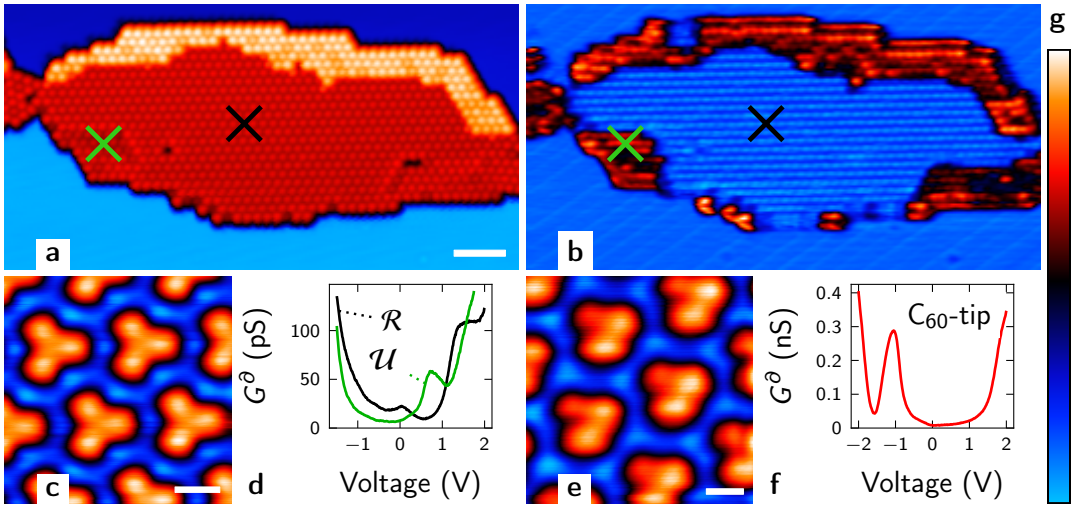

Figure 5.1. **a**, Constant-current topography and **b**, simultaneously acquired differential conductance map of C_{60}/Cu(111) measured at 0.7 V, 0.1 nA. **c**, Constant-current topography of C_{60}/Cu(111) obtained at 2 V, 0.1 nA. **d**, Differential conductance of a reconstructed ($\mathcal{R}$, black) and unreconstructed ($\mathcal{U}$, green) C_{60} on Cu(111). **e**, Constant-current topography of C_{60}/Cu(111) acquired at 1.5 V, 0.1 nA with a C_{60}-terminated tip. **f**, Differential conductance of the bare Cu(111) surface measured with a C_{60}-terminated tip. **g**, Color scale for **a-c,e** ranging from 0 to 0.81 nm (**a**), 98 pm (**c**), and 90 pm (**e**). The feedback loop was opened at 2 V, 0.1 nA prior to spectroscopy of **d** and **f**. A Lock-In modulation $V_m = 20\,\mathrm{mV_{RMS}}$ was applied during the measurements of **a**, **b**, **d**, and **f**. Scale bars are 5 nm (**a**) and 0.5 nm (**c**, **e**). Colored markers in **a**,**b** correspond to G^∂ data of the same color in **d**. The image of **e** was FFT-filtered reducing noise for $r^{-1} \geq 4\,\mathrm{nm}^{-1}$ ($r = \sqrt{x^2 + y^2}$, x and y representing the horizontal and vertical dimension, respectively).

to the surface, since C_{60} on Cu(111) predominantly expose a C pentagon to the vacuum. The lobe to the top left of each molecule in Fig. 5.1 **e** appears lower, most likely due to a slight tilt of the molecule at the tip apex. The differential conductance obtained with a C_{60}-terminated tip on the plain Cu(111) surface resembles that of $\mathcal{U}$–C_{60} (Fig. 5.1 **d**) mirrored with respect to zero bias. This observation is in accordance with theoretical expectations for exchanging ϱ_s with ϱ_t and previous observations of C_{60} on Au(111)[132].

5.2. Vertical Force Spectroscopy

In the following, vertical force spectroscopy data are presented and discussed. For this purpose, the frequency shift Δf was acquired as a function of the tip displacement z and the vertical force subsequently calculated by means of the Sader-Jarvis deconvolution algorithm[42]. Fig. 5.2 **a** shows an exemplary $\Delta f\,(z)$ trace acquired for a C_{60}–C_{60} contact on Cu(111). The corresponding force $F\,(z)$ is shown in Fig. 5.2 **b**. With decreasing tip–sample separation, i.e., increasing tip displacement z, the magnitude of F increases until the point of maximum attraction (z_c, F_c) is reached at $z = z_c \approx 268$ pm. At further tip approach, the total force increases and turns repulsive at $z \approx 434$ pm. The progression of the total force is in qualitative agreement with previous reports[17,188]. The magnitude of F_c is of the same order[17,188]. However, the F onset occurs at

lower z. This discrepancy is most likely due to a higher contribution of long–range background forces $F^{(\mathrm{bg})}$.

The long-range force contribution can be estimated using a power law[17].

$$F^{(\mathrm{bg})}(z) = \mathfrak{c} - \mathfrak{a} \cdot (\mathfrak{z} - z)^{-\mathfrak{b}} \tag{5.1}$$

$F^{(\mathrm{bg})}$ is fit to $F(z \leqslant 0)$ data, which is depicted as dashed light blue line in Fig. 5.2 **b** with fit coefficients $\mathfrak{a} = 2.36 \pm 0.73\,\mu\mathrm{N/pm}^{1.42}$, $\mathfrak{b} = 1.42 \pm 0.04$, $\mathfrak{c} = 16 \pm 1\,\mathrm{pN}$, and $\mathfrak{z} = 877 \pm 28\,\mathrm{pm}$. The exponent $\mathfrak{b} = 1.42 \pm 0.04$ is consistent with contributions of electrostatic ($F_{\mathrm{el}} \propto z^{-1}$) and van-der-Waals ($F_{\mathrm{vdW}} \propto z^{-2}$) forces in a sphere-plane geometry.

The short-range force $F^{(\mathrm{s\text{-}r})}$ can be estimated by subtracting $F^{(\mathrm{bg})}$ from F, i.e., $F^{(\mathrm{s\text{-}r})} = F - F^{(\mathrm{bg})}$. $F^{(\mathrm{s\text{-}r})}$ is presented as red line in Fig. 5.2 **b,c**. $F^{(\mathrm{s\text{-}r})}$ remains zero up to $z \approx +40\,\mathrm{pm}$,

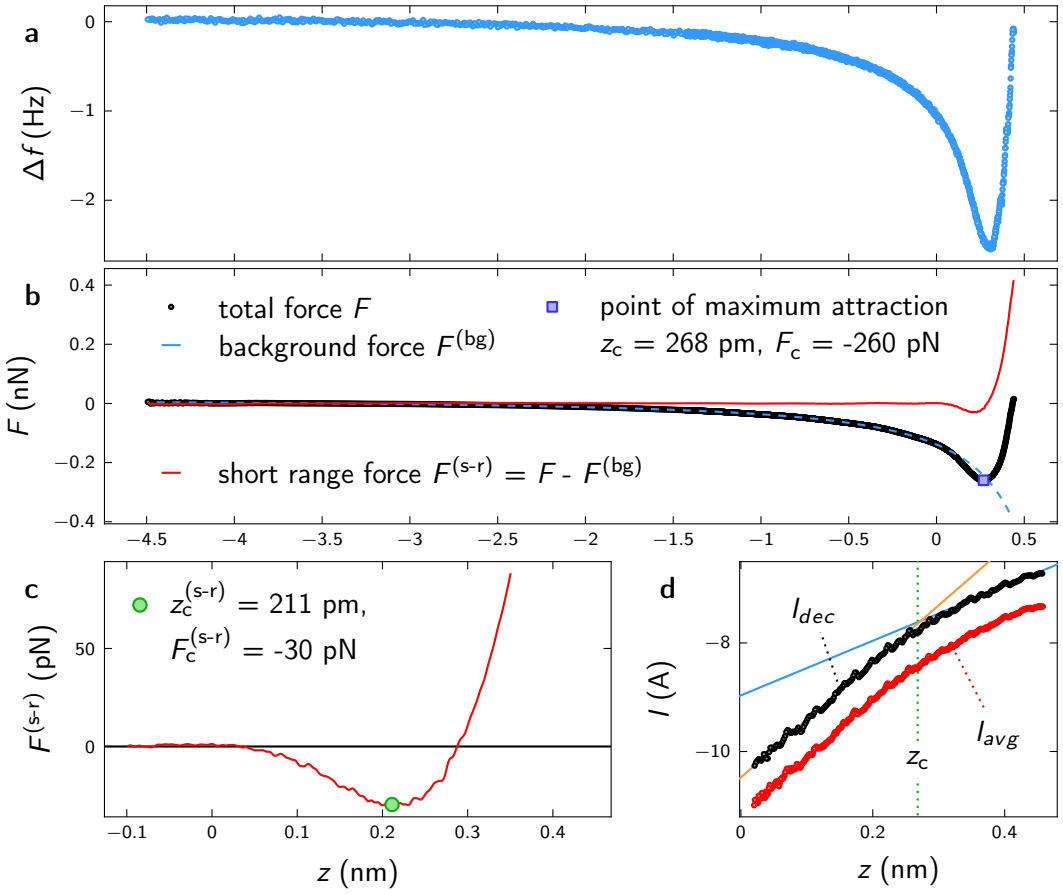

Figure 5.2. Force and current measured for a C_{60}-C_{60} contact on Cu(111). **a**, Frequency shift Δf as a function of tip displacement z. **b**, Total force F (black), background force $F^{(\mathrm{bg})}$ (blue dashed), and short-range force $F^{(\mathrm{s\text{-}r})}$ (red). **c**, Short-range force $F^{(\mathrm{s\text{-}r})}$. The green circle denotes the $F^{(\mathrm{s\text{-}r})}$ minimum ($z_c^{(\mathrm{s\text{-}r})}$, $F_c^{(\mathrm{s\text{-}r})}$). **d**, Measured (red, I_{avg}) and deconvoluted (black, I_{dec}) current as a function of z. The light blue and orange lines are simple exponential fits to I_{dec} data for $z < z_c$ (orange) and $z > z_c$ (blue). The z value at the force minimum, z_c, is indicated as blue square in **b** and green dotted line in **d**. The feedback loop was opened at 1.5 V, 0.1 nA and the data acquired at 0.15 V. The force sensor was operated at $A = 300\,\mathrm{pm}$, and $f_0 = 28.9\,\mathrm{kHz}$. The force minima were obtained from the minima of quadratic fits to F and $F^{(\mathrm{s\text{-}r})}$ data for $|z - z_c| \leqslant 30\,\mathrm{pm}$ and $|z - z_c^{(\mathrm{s\text{-}r})}| \leqslant 30\,\mathrm{pm}$, respectively.

decreases until it reaches the force minimum $F_c^{(s\text{-}r)} \approx -30\,\mathrm{pN}$ at $z_c^{(s\text{-}r)} \approx 211\,\mathrm{pm}$ and turns repulsive for $z \gtrsim 288\,\mathrm{pm}$. The short-range force is attractive for $\Delta z \sim 250\,\mathrm{pm}$, which is consistent with previously reported values for the Lennard-Jones equilibrium distance, $z_{eq} = 0.2\,\mathrm{nm}$ (ref. 190). An estimate considering two C_{60} molecules with each C–C interaction modeled by a LJ potential (using $z_{eq} = 0.2\,\mathrm{nm}$, $\varepsilon = 2.5\,\mathrm{meV}$, ref. 190) yields a maximum attraction of $-53\,\mathrm{pN}$, which is of the same order of magnitude as the estimate of the short-range force exhibited in Fig. 5.2 **b,c**.

The current measured simultaneously to the acquisition of Δf is presented in Fig. 5.2 **d**. The AFM oscillation is removed by deconvolution[43]. I increases exponentially and levels off at close tip approach starting at $z \approx 220\,\mathrm{pm}$. The intersection of simple exponential extrapolations for $z < z_c$ (orange) and $z > z_c$ (blue) matches the point of maximum attraction inferred from Fig. 5.2 **b**. The $I(z)$ progression as well as the magnitude of the deconvoluted conductance upon leaving the tunneling regime ($\approx 2\,\mathrm{mG_0}$) is consistent with previous reports of C_{60}–C_{60} contacts[17,132].

A set of F data acquired for different voltages $-0.9\,\mathrm{V} \leq V \leq +0.9\,\mathrm{V}$ is presented in Fig. 5.3 **a**. For each trace, the feedback loop is disabled at 1.5 V, 0.1 nA. Then, the voltage is ramped to the target bias and subsequently the frequency shift $\Delta f\,(z)$ measured. The traces qualitatively resemble the $F(z)$ progression presented in Fig. 5.2 **b** for all V. With increasing voltage, the traces shift horizontally with z at the total force minimum, z_c, moving from $z_c \approx 220\,\mathrm{pm}$ at –0.9 V to $z_c \approx 340\,\mathrm{pm}$ at +0.9 V (Fig. 5.3 **b**). The linear slope of z_c amounts to $\partial_V z_c = 55 \pm 5\,\mathrm{pm/V}$. $\partial_V z_c$ is of the same order of magnitude as estimated from $I(z)$ data of metal-C_{60} contacts[18]. The force value at contact, F_c, has a quadratic dependence on the voltage in accordance with electrostatic forces (Fig. 5.3 **b**). A quadratic fit of the $F_c\,(V)$ data is centered at $0.23 \pm 0.02\,\mathrm{V}$ which is in agreement with the contact potential inferred from $\Delta f(V)$ as well as $F(V)$ data.

For further analysis, parabolic fits to the force data of Fig. 5.3 **a** were performed for constant z using the formula

$$F(V, z = \text{const.}) = a \cdot (V - V_{max})^2 + F_{max} \tag{5.2}$$

The fit parameters $a\,(z)$ and $V_{max}\,(z)$ are presented in Fig. 5.3 **c** and Fig. 5.3 **d**, respectively, with corresponding 95% fit uncertainty. V_{max} is constant within the fit uncertainty up to $z \approx 0$, then increases up to $z \approx 170\,\mathrm{pm}$, and subsequently decreases. a decreases with increasing z from $a = 0$ at $z \to -\infty$ until $z \approx 200\,\mathrm{pm}$, followed by a steeper increase.

The data shown in Fig. 5.3 **a** are background-subtracted as described above. Fig. 5.4 **a** presents the estimated short-range contributions, $F^{(s\text{-}r)}$. The traces are qualitatively similar, initially decreasing up to the force minimum at ($z_c^{(s\text{-}r)}$, $F_c^{(s\text{-}r)}$), followed by a steep increase. The z_c shift persists for the short-range force with a slightly reduced slope of $38 \pm 7\,\mathrm{pm/V}$. Consequently, short-range effects dominantly contribute to the bias-dependence of z_c observed for the total force. $F_c^{(s\text{-}r)}$ also retains the quadratic variation occurring for the total force. However, the magnitude of the $F_c^{(s\text{-}r)}(V)$ variation is one order of magnitude lower than for $F_c(V)$ data. Since the background was fit with free parameters and approximated by a simple power law, the possibility of a systematic error cannot be excluded.

These findings are in contrast to the conventional picture, which considers only a Lennard-Jones-like contribution to the short-range force. The LJ potential has no bias-dependence. Hence, no variation of $z_c^{(s\text{-}r)}(V)$ and $F_c^{(s\text{-}r)}(V)$ should be observable. At the most, a slight quadratic variation should occur, since the force minima of a LJ plus electrostatic force varies slightly.

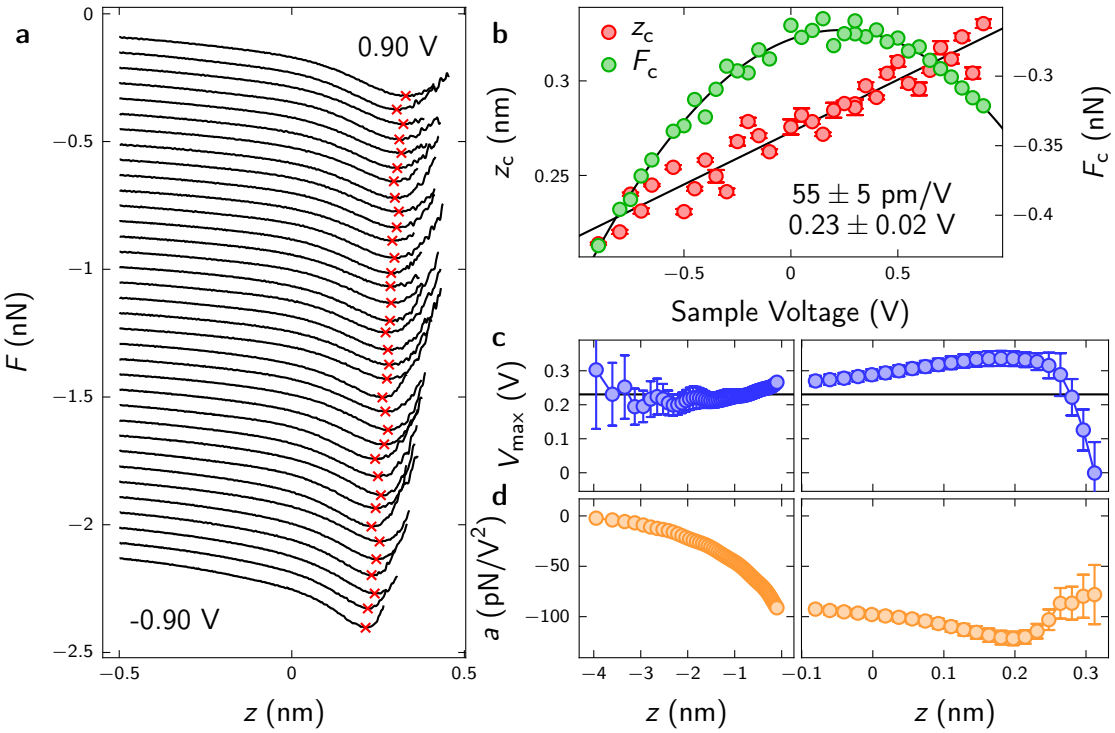

Figure 5.3. Force spectroscopy for a C_{60}-C_{60} contact on Cu(111). **a**, Vertical force F as a function of piezo displacement z for different bias voltages $-0.9\,\mathrm{V} \leq V \leq 0.9\,\mathrm{V}$. Each point of maximum attractive force (z_c, F_c) is indicated by a red cross. The F data were obtained by applying a ten point moving average filter prior and subsequent to the deconvolution of $\Delta f\,(z)$ data via the Sader method[42]. The curves are vertically shifted by a varying amount in order to minimize overlapping. $z = 0$ corresponds to 1.5 V, 0.1 nA. **b**, z_c (red, left axis) and F_c (green, right axis) as a function of bias voltage V. Black lines are linear and quadratic fits to $z_c\,(\mathrm{V})$ and $F_c\,(\mathrm{V})$, respectively. The linear slope of $z_c\,(\mathrm{V})$ amounts to $55 \pm 5\,\mathrm{pm/V}$. The $F_c\,(\mathrm{V})$ parabola is centered at $0.23 \pm 0.02\,\mathrm{V}$. **c**-**d**, Evaluation of the voltage at the maximum (**c**) and the curvature (**d**) of quadratic fits to $F(V, z = \mathrm{const})$ obtained from the data presented in **a**. Circles (error bars) present the parameter estimates (95% uncertainty intervals) obtained from least squares fits, circles in **b** were obtained by fitting a parabola to $F(|z - z_c| \leqslant 35\,\mathrm{pm})$.

Considering the elasticity of atomic scale junctions[17,184] might imply a quadratic dependence of $z_c^{(\mathrm{s\text{-}r})} \propto (V - V_{cp})^2$ as well, considering an electrostatic force $F_{el} \propto (V - V_{cp})^2$ exerted on the C_{60} molecules. In this picture, the C_{60} molecules are considered elastically coupled to each electrode, which leads to a variation of the molecule–electrode separation due to the force exerted on the molecule. Hooke's law, which in the linear regime reads $F_{tot} \propto \Delta z$, then yields $\Delta z \propto (V - V_{cp})^2$.

The data of Fig. 5.3 is not representative of all C_{60}–C_{60} contacts. Fig. A.7 presents a different data set that does not exhibit a linear increase of z_c with V. In addition to that, no variation of V_{max} (within the fit uncertainty) and a simple monotonic decrease of a with z occurs. Data showing variations in $z_c\,(V)$ and $V_{max}\,(z)$ as well as a non-monotonic behavior of $a\,(z)$ (indicated as $\oplus$ in the following) are not discernible from data without variations ($\ominus$) according to topographic or spectroscopic signatures. Most significantly, no differences between $\mathcal{R}$– and $\mathcal{U}$–C_{60} were observed. In addition to C_{60}–C_{60} contacts on Cu(111), vertical force spectroscopy was performed for metal–

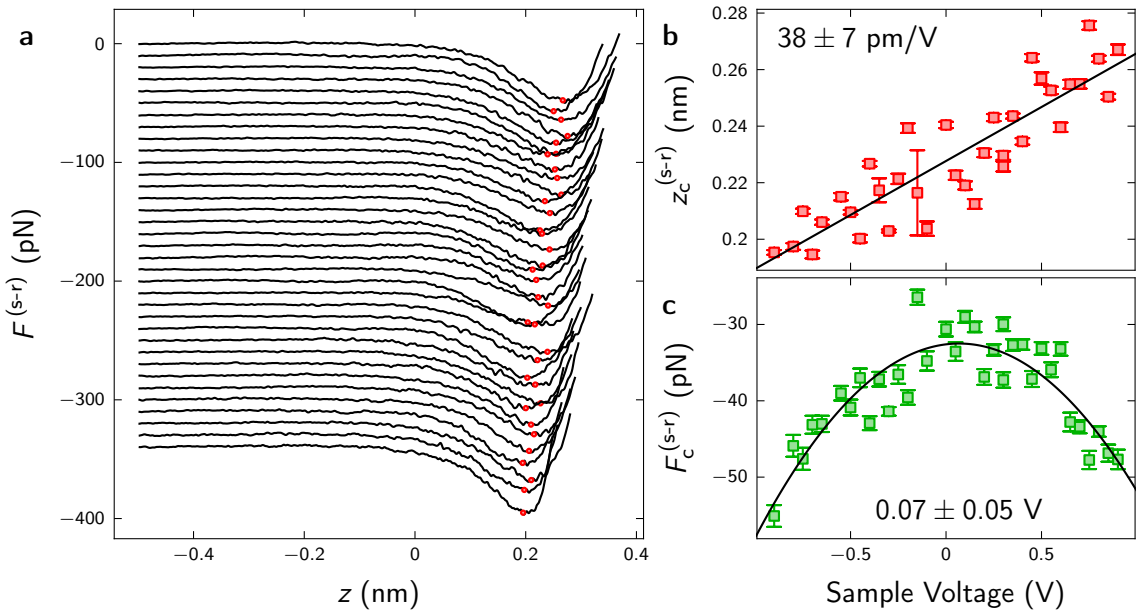

Figure 5.4. **a**, Short-range force obtained by background-subtraction of the data shown in Fig. 5.3 **a**. The data are vertically offset for clarity. The z and F value at point of maximum attractive force of the short range force $z_c^{(s\text{-}r)}$ (**b**) and $F_c^{(s\text{-}r)}$ (**c**), respectively, is presented as a function of the applied bias voltage and indicated as red dots in **a**. Squares (error bars) present the parameter estimates (95% uncertainty intervals) obtained from least squares fits of a parabola to $F^{(s\text{-}r)}(|z - z_c^{(s\text{-}r)}| \leqslant 35\,\mathrm{pm})$.

C_{60} contacts on Pb(111) (Fig. A.8). Here, the variations observed in Fig. 5.3 are reproduced.

In total, 15 data sets of C_{60}–C_{60} contacts on Cu(111) were obtained. In order to unveil the possible origin of the experimental observations for $\oplus$ data and quantitatively characterize the data, additional variables were calculated for each set. The $F_c(V)$ data were fit to the equation

$$F_c(V) = \hat{a} \cdot (V - V_{c,max})^2 + F_{c,max} \tag{5.3}$$

for each data set. The quantity relevant for the following discussion, $F_{c,max}$, represents a measure of the bias-independent background force. $\hat{G}_c$ denotes the mean conductance at contact $G_c = G(z = z_c)$. Since the transmission factor for electron tunneling rapidly increases for $|V| \gtrsim 0.5\,\mathrm{V}$, only data obtained at voltages $|V| \leqslant 0.5\,\mathrm{V}$ were included in the calculation of $\hat{G}_c$ thus enabling the comparison of data sets obtained within different bias ranges.

$$\hat{G}_c := \left\langle G(z = z_c,\ |V| \leqslant 0.5\,\mathrm{V}) \right\rangle \tag{5.4}$$

$\partial_V z_c$ as a function of $\hat{G}_c$ and $F_{c,max}$ is presented in Fig. 5.5. Fig. 5.5 **a** suggests an onset of the observed $\oplus$ effects for $F_{c,max} \gtrsim -0.5\,\mathrm{nN}$. A sectional linear fit according to the equation

$$\partial_V z_c = \begin{cases} a^\dagger \cdot (F_{c,max} - F^\dagger) & F_{c,max} \geqslant F^\dagger \\ 0 & F_{c,max} < F^\dagger \end{cases} \tag{5.5}$$

with fit coefficients $F^\dagger = -0.51 \pm 0.09\,\mathrm{nN}$, and $a^\dagger = 0.19 \pm 0.06\,\mathrm{m\,V^{-1}\,N^{-1}}$ represents the data rather well (red line in Fig. 5.5 **a**). The strong correlation between $\partial_V z_c$ and $\hat{G}_c$ ($\mathfrak{r} = 0.83 > 0.7$) is revealed in Fig. 5.5 **b**.

5.3. Discussion

The data presented in the current chapter were obtained using two different force sensors with different PtIr tips of the same diameter. While the tip wire attached to the first sensor, tip $\mathfrak{A}$, was prepared by focused ion beam milling (FIBM)[191–193], the tip of the second sensor, tip $\mathfrak{B}$, was chemically etched in a $CaCl_2$ solution[191,194,195]. Tip $\mathfrak{B}$ features comparatively large force values (cf. Fig. A.7, Fig. 5.5 **a**), consistent with enhanced background forces due to larger tip radii r_t, i.e., rather blunt apices, of tip $\mathfrak{B}$. This interpretation is in agreement with previously reported tip radii, which are as low as $\sim$3 nm using FIBM[192,193]. Chemically etched PtIr tips were reported with radii above $\sim$50 nm (ref. 191,194,195). In general, blunter tips, i.e., tips with a higher background force inferred from a lower Δf value at the STM set point, exhibited a lower success rate for the termination of the tip with a C_{60} molecule. This observation is consistent with the enhanced stability of flat electrodes, i.e., atomic rearrangements at the tip apex require much more energy than for sharper tips. In order to detach a molecule from the surface, a strong tip-molecule coupling must be achieved. Since atomic rearrangements require more energy for blunt electrodes, a reduced success rate is expected from energetic considerations.

The magnitude of the $\oplus$ effects appears to be highly dependent on the microscopic details of the tip. Neglecting any possible differences between tips $\mathfrak{A}$ and $\mathfrak{B}$ implies a linear increase of $\partial_V z_c$ with $\hat{G}_c$. Similarly, $\partial_V z_c$ is proportional to $F_{c,max}$ for $F_{c,max} \gtrsim -0.5$ nN. However, considering the $\partial_V z_c(\hat{G}_c)$ data for tips $\mathfrak{A}$ and $\mathfrak{B}$ individually does not lead to the same conclusion as the combined evaluation. The data scattering indicates at least a partial contribution of additional parameters.

A direct comparison between tips $\mathfrak{A}$ and $\mathfrak{B}$ might be inappropriate, since their chemical composition may differ. Both tips consist of PtIr wire of the same diameter and are prepared *in-situ* by field evaporation, indentation into the substrate, as well as controlled contacts with the surface.

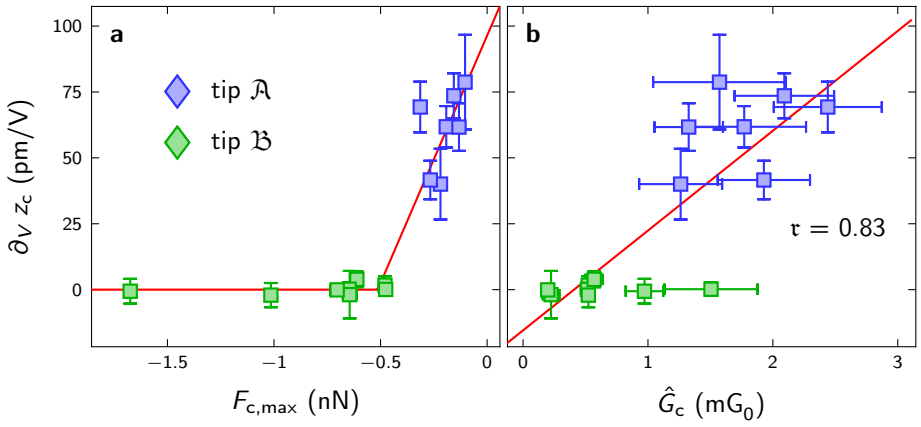

Figure 5.5. Evaluation of force spectroscopy data for 15 C_{60}-C_{60} contacts on Cu(111). The linear slope of $z_c(V)$, $\partial_V z_c$, is shown as a function of the force value at the maximum of the $F_c(V)$ parabola, $F_{c,max}$ (**a**), and the mean contact conductance $\hat{G}_c$ (**b**). Blue (green) data were obtained with tip $\mathfrak{A}$ ($\mathfrak{B}$). Red lines denote a sectional linear (**a**) and simple linear (**b**) fit acting as guide to the eye. The correlation coefficient between $\partial_V z_c$ and $\hat{G}_c$, $\mathfrak{r} = 0.83$, is indicated in **b**. Markers (error bars) of $\partial_V z_c$ and $F_{c,max}$ present the parameter estimates (95% uncertainty intervals) obtained from least squares fits, markers (error bars) of $\hat{G}_c$ denote mean value (standard deviation) of G_c ($V \leqslant 0.5$ V).

Previously, the process of atom evaporation in an electric field was studied using DFT calculations. The direction of the force acting on surface atoms was found to depend on the field strength as well as their vertical position relative to the electrode[196]. Hence, either removing atoms from the tip apex or coating with substrate material may occur during field emission for the same externally applied voltage depending on the initial tip geometry. This consideration indicates a potentially differing chemical composition of the apices of tips $\mathfrak{A}$ and $\mathfrak{B}$, which feature distinct initial tip radii due to the different fabrication processes. Moreover, the tip apices were modified *in-situ* between measurements. Indentations $\sim 1 - 5\,\mathrm{nm}$ into the substrate were occasionally performed that resulted in the creation of cavities of $\sim 10\,\mathrm{nm}$ diameter at the surface. Subsequent to such indentations, the tip is commonly assumed to be covered with substrate material. Predominantly, smaller contacts between tip and surface were conducted that entailed the transfer of single atoms or small atom clusters to the surface. The chemical composition of the tip apex depends on the balance between substrate material transferred to the tip during field evaporation as well as indentations and atoms transferred from the tip to the surface during smaller contacts. However, the chemical composition is not directly accessible in STM/AFM experiments.

To date, bias-dependent force spectroscopy including the analysis described above has not been reported. The origin of the z_c shift as well as the non-trivial behavior of $a(z)$ and $V_\mathrm{max}(z)$ is not obvious. Conventionally, forces in non-polar and non-magnetic junctions in UHV are only expected to consist of van-der-Waals, electrostatic, and Pauli forces. Hence, the only voltage-dependence enters via $F_\mathrm{el} \propto (V - V_\mathrm{cp})^2$ [cf. eq. (2.49)]. Varying V does not qualitatively alter the z-dependence of F_el but only changes its magnitude.

In order to examine the possible influence of different V, forces were calculated within a simple analytic model considering van-der-Waals, electrostatic, and Pauli interactions according to eqs. (2.48), (2.49), and (2.50). F_LJ is assumed to occur primarily due to the nearest C atoms using $\varepsilon = 2.5\,\mathrm{meV}$ in accordance with a previous report[190]. The C atoms are located 0.7 nm from the electrodes, which corresponds to the C_{60} diameter[197]. $z_\mathrm{eq} = 0.4\,\mathrm{nm}$ is used in order to enhance resemblance with the experimental data, which is of the same order as previously reported values for intra-C_{60} C–C bonds[190]. F_el and F_vdW between a spherical tip and a planar electrode are included using $\mathscr{H} = 0.2\,\mathrm{eV}$, $V_\mathrm{cp} = 0.2\,\mathrm{V}$, and $r_\mathrm{t} = 10\,\mathrm{nm}$. Previously reported values amount to $0.1\,\mathrm{eV} \lesssim \mathscr{H} \lesssim 2\,\mathrm{eV}$ (ref. 198–200). Tips prepared using focused ion beams yielded tip radii $r_\mathrm{t} \gtrsim 3\,\mathrm{nm}$ (ref. 192,193). However, evaluating forces within a simple analytic model does not reproduce the experimentally observed variations of $\oplus$ data (cf. Fig. 5.6). z_c and V_max remain constant while $a(z)$ decreases monotonically. Varying the input parameters ε, z_eq, $\mathscr{H}$, and r_t did not alter the results qualitatively. If at all, there is a slight quadratic dependence of $z_\mathrm{c}(V)$ when decreasing the contribution of F_vdW, i.e., decreasing $\mathscr{H}$.

In the following, several possible origins of the observed variations of $\oplus$ data are discussed. The arguments are evaluated on the basis of the data shown in Fig. 5.5, considering the data for both tips as single data set, i.e., neglecting possible differences due to experimentally inaccessible properties such as chemical composition.

Atomic Scale Relaxations

The most intuitive explanation consists of bias-dependent atomic scale relaxations. Previously, relaxations of $\sim 100\,\mathrm{pm}$ ($\sim 25\,\mathrm{pm}$) were reported for metal–C_{60} (C_{60}–C_{60}) contacts at voltages

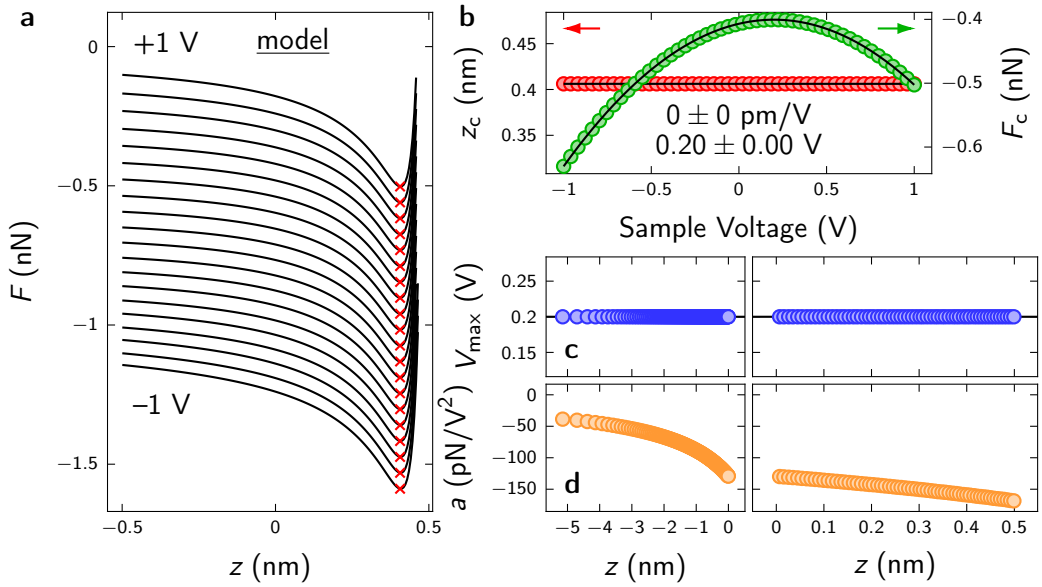

Figure 5.6. Evaluation of force data obtained from a simple model calculation using analytic expressions for van-der-Waals, Lennard-Jones, and electrostatic forces analogous to Fig. 5.3. Model parameters are $\mathscr{H} = 0.2\,\mathrm{eV}$, $\varepsilon = 2.5\,\mathrm{meV}$, $V_{\mathrm{cp}} = 0.2\,\mathrm{V}$, $z_{\mathrm{eq}} = 0.4\,\mathrm{nm}$, and $r_{\mathrm{t}} = 10\,\mathrm{nm}$.

close to V_{cp} (ref. 17). C_{60} molecules adsorbed to metal substrates are charged due to electron transfer from the metal to the C_{60}. The application of an external bias voltage, i.e., an electric field, induces a capacitor force on charges within the junction thereby modifying the molecule–electrode separation.

This interpretation is in qualitative agreement with Fig. 5.5 **a**. A blunter tip, i.e., larger magnitude of $F_{\mathrm{c,max}}$, means a geometrically more symmetric junction. An infinitely blunt electrode corresponds to a planar surface. Hence, assuming a Cu covered tip, the coupling of the molecule to tip and sample tends to be similar. The ensuing relaxations at both interfaces are approximately equal in magnitude and direction and compensate each other.

A rough approximation of a bias voltage of 1 V applied to a 0.5 nm wide plate capacitor yields an electric field strength of 2 V/nm. A C_{60} charged by $3\,\mathrm{e}^-$ is subjected to a force of $2\,\mathrm{V/nm} \cdot 3\,\mathrm{e} = 0.96\,\mathrm{nN}$. Previously, spring constants for sample-C_{60} and tip-C_{60} interfaces were estimated as $112\,\mathrm{N\,m^{-1}} \leqslant k_{\mathrm{s–C_{60}}} \leqslant 129\,\mathrm{N\,m^{-1}}$ and $43\,\mathrm{N\,m^{-1}} \leqslant k_{\mathrm{t–C_{60}}} \leqslant 81\,\mathrm{N\,m^{-1}}$, respectively[17]. Comparing the combined k of tip and sample with the experimentally determined values revealed an overestimation by a factor of 2 (ref. 17). In the following estimate, $k_{\mathrm{s–C_{60}}}/2$ and $k_{\mathrm{t–C_{60}}}/2$ are used. Employing Hooke's law yields displacement values $\Delta z = F/k$ of $15\,\mathrm{pm} \leqslant \Delta z_{\mathrm{s–C_{60}}} \leqslant 17\,\mathrm{pm}$ and $24\,\mathrm{pm} \leqslant \Delta z_{\mathrm{t–C_{60}}} \leqslant 45\,\mathrm{pm}$. Since both molecules in a C_{60}–C_{60} contact are negatively charged and hence displaced in the same direction, the effective reduction amounts to $9\,\mathrm{pm} \leqslant |\Delta z_{\mathrm{s–C_{60}}} - \Delta z_{\mathrm{t–C_{60}}}| \leqslant 28\,\mathrm{pm}$. The experimentally observed shift of $\sim 55\,\mathrm{pm/V}$ is of the same order of magnitude, exceeding the estimated values by a factor of 2 to 6.

At first glance, the directionality is opposite to the experimental observations. A negative sample voltage implies a negatively charged sample, and consequently a displacement of both molecules toward the tip. Due to the higher stiffness of the sample–C_{60} interface, the molecule at the tip is moved more compared to the molecule on the surface. Hence, the actual junction separation is increased and contact should occur at higher z. In contrast, lower z_{c} values are

observed at negative voltages.

However, experimental observations indicate a stronger attachment of the molecule to the tip, and consequently a higher $k_{t\text{–}C_{60}} > k_{s\text{–}C_{60}}$ as rationalized in the following. Termination of the tip apex with a C_{60} molecule is achieved by approaching the tip to the molecule, until discontinuities in the current signal atomic rearrangements and the formation of tip-C_{60} bonds. In order to detach a molecule from the surface, its coupling to the tip must exceed its coupling to the surface. Consequently, the successful detachment from the surface implies a molecule-tip interface with a stronger coupling then that of the molecule-surface interface. In this case, the expected directionality of the z_c shift matches the experimental observations. Note that assuming an enhanced $k_{t\text{–}C_{60}}$ alters the estimate given in the preceding paragraph. A higher $k_{t\text{–}C_{60}}$ leads to a decrease of $|\Delta z_{t\text{–}C_{60}}|$ and consequently a reduced magnitude of the field-induced relaxations.

The assumption of $k_{t\text{–}C_{60}} > k_{s\text{–}C_{60}}$ is contrary to the stiffness values previously obtained via DFT[17]. However, the authors presumed a specific geometry of the C_{60}-terminated tip by replacing the outermost atom of a pyramidal Cu tip with the C_{60}. Consequently, the weaker coupling of the molecule to the tip only reflects the input for the DFT calculations.

In order to qualitatively examine the impact of bias-dependent relaxations, the model calculation described above is slightly modified. The argument z entering F_{LJ} is replaced by $z+\alpha V$ mimicking an effective modification of the C_{60}–C_{60} separation linear with V. The results of the modified calculations are presented in Fig. A.10 for $\alpha = 40\,\mathrm{pm/V}$. While a linear slope of $z_c\,(V)$ is obtained, $F_c\,(V)$ and $V_{max}\,(z)$ are not in agreement with $\oplus$ data. The experimental $F_c\,(V)$ parabolae are centered at $V \approx V_{cp}$ matching $V_{max}(z \to -\infty)$. Fig. A.10 **b** presents a $F_c\,(V)$ parabola that is shifted by $-0.33\,\mathrm{V}$ with respect to $V_{cp} = 0.2\,\mathrm{V}$. $V_{max}\,(z)$ remains constant at $V_{max} = V_{cp}$, then decreases at closer tip approach lacking the experimentally observed increase at $z > 0$. Furthermore, the increasing a at close tip approach is reproduced.

Dipole Forces

Additional electrostatic forces may occur due to dipole or multipole interactions. Two static dipoles $\vec{p}_1$ and $\vec{p}_2$ separated by a distance z exert a dipole force $\vec{F}_{dipole}$ on each other according to

$$\vec{F}_{dipole} = -\frac{3}{4\pi\epsilon_0}\vec{\nabla}\frac{\vec{p}_1\cdot\vec{p}_2 - 3(\vec{e}_z\vec{p}_1)(\vec{e}_z\vec{p}_2)}{z^3} \tag{5.6}$$

($\vec{e}_z$ - unit vector in z direction, ϵ_0 - vacuum permittivity)[201]. Two aligned dipoles $\vec{p}_1 = p_1\vec{e}_z$, $\vec{p}_2 = p_2\vec{e}_z$ yield $F_{dipole} \propto p_1 \cdot p_2$. Additionally, inhomogeneous electric fields ($\vec{\nabla}\vec{E} \neq 0$) lead to forces on static dipoles $\vec{p}$, i.e., $\vec{F}_{in} = (\vec{p}\,\vec{\nabla})\,\vec{E}$ (ref. 202). The force on a dipole $\vec{p} = p\,\vec{e}_z$ centered in an axially symmetrical electric field E simplifies to $\vec{F}_{in} = p \cdot \partial_z E_z\,\vec{e}_z$.

C_{60} is a nonpolar molecule which features a comparatively high polarizability[203,204]. Polarization by the electric field yields dipole moments $p_{1,2} \propto V$, which are aligned in z direction for axially symmetric tips. The ensuing dipole force between both molecules thus presents a quadratic voltage-dependence $F_{dipole} \propto p_1 \cdot p_2 \propto V^2$. Similarly, the electric field gradient along z, $\partial_z E_z$, is proportional to V. Consequently, the force $F_{in} = p \cdot \partial_z E_z$ is proportional to V^2 as well. Since no linear voltage-dependence occurs, the linear $z_c(V)$ variations do not originate from dipole forces.

Contact Potential Variations

Eq. (2.49) gives the voltage-dependence of $F_{el} \propto (V - V_{cp})^2$. A possible contribution to the observed behavior of $\oplus$ data consists of a distance dependency of the local contact potential difference (LCPD) V_{cp}, i.e., $\partial_z V_{cp} \neq 0$. The distance-dependence of V_{cp} is affected by charges and multipole moments that arise at facets such as step edges or tip asperities. At large tip–sample separations, V_{cp} predominantly varies due to distance-dependent variations of the effective contribution of different areas. Steps of the substrate as well as tip asperities are stochastically distributed. When the tip is in close proximity to the sample, the presence of the electromagnetic potential of the tip (sample) leads to charge rearrangements in the sample (tip). The presence of large forces causing atomic relaxations further modifies the charge distribution and consequently impacts V_{cp}. The extent of the V_{cp} modification crucially depends on the geometry[205] and chemical composition of tip and sample.

Previously, V_{cp} variations of tens of mV were reported for 10 nm to mm-ranges[206–210]. In Au-Au break junctions, V_{cp} varies by ~ 100 mV for $\Delta z \sim 50$ nm (ref. 205). At closer junction separations, higher values of the order ~ 100 mV were reported on NaCl bilayers on Cu(111)[211] as well as on hydroxylated TiO_2 (ref. 212) and ~ 1 V on NaCl surfaces[213,214], CaF_2 on Si(111)[215], Cu(001)[216], Si(111)[217,218] as well as for Pt atoms on hydroxylated TiO_2 (ref. 212).

Including a variation of $V_{cp}(z)$ resembling the experimentally observed $V_{max}(z)$ variations into the simple model calculation did not reproduce the linear evolution of $z_c(V)$. Consequently, this effect cannot be solely responsible for the experimental observations. The decrease of $V_{max}(z)$ at closest tip approach (cf. $z \geqslant 200$ pm in Fig. 5.3, $z \geqslant 300$ pm in Fig. A.8) would be consistent with the vanishing contact potential expected for a fully developed chemical contact. However, only $\oplus$ data exhibit a $V_{max}(z)$ vanishing to $V_{max}(z) \to 0$, whereas typical $\ominus$ data present $V_{max}(z) \approx$ const (cf. Fig. A.7). This finding suggests that a C_{60}–C_{60} contact is not sufficient to reduce the contact potential difference to zero. Hence, the decrease of $V_{max}(z)$ for large z is most likely not caused by contact potential variations.

Phantom Force

Probing samples with low conductivity, such as Si, gives rise to an apparent force due to a finite voltage drop inside the sample. Previously, this effect was observed on a Si(111) surface with an estimated surface resistance $R_s \sim 100$ MΩ (ref. 219). At $R_s \sim 20$ GΩ, the Phantom force even leads to an inversion of the $\Delta f\,(V)$ parabola[220].

Charge transport through single C_{60} molecules on Cu surfaces occurs at conductances in excess of G_0, i.e., the intrinsic resistance of a C_{60} molecule is below 13 kΩ (ref. 132,133,180). Assuming an intrinsic C_{60} resistance $R_{60} = G_0^{-1}$ at a junction conductance of $R_j = 10\,mG_0$ yields a negligible voltage drop across the C_{60} molecule of $R_{60}/(R_{60} + R_j) \approx 1\%$ for metal–C_{60} contacts and $R_{60}/(2R_{60} + R_j) \approx 1\%$ for C_{60}–C_{60} contacts.

However, previous DFT calculations indicate a significant voltage drop of ∼80% drop for a metal–C_{60} contact on Cu(111), yet only at positive voltages[221]. The effect was assigned to the increased sample-C_{60} distance, which amounted to 600 pm for the maximum voltage drop of ∼80%. A polarity-dependence is not observed in the present experiments. For C_{60}–C_{60} contacts, a similar voltage drop may occur at the tip–molecule interface at negative voltages. However,

due to different coupling strengths an asymmetry with respect to zero voltage should occur, which is not observed in the present experiments. Larger forces, i.e., higher $F_{c,max}$ values, should lead to increased C_{60}–electrode distances and consequently larger effects, which is in contrast to Fig. 5.5 **a**. Moreover, this interpretation is not consistent with metal–C_{60} contacts on Pb(111) (cf. Fig. A.8) and STM experiments of metal–C_{60} contacts on Cu(111)[18]. For metal–C_{60} contacts, the polarity-dependence would occur. Finally, in contrast to previous experiments on semiconducting surfaces[219,220], the total voltage drop occurs at considerably lower distance ranges. Consequently, the voltage-induced charge accumulation relevant to the electrostatic force should not deviate significantly compared to junctions without molecules.

Non-Equilibrium Forces

In addition to the phenomena mentioned above, current-induced effects might contribute to the present observations. Bond formation between two atoms occurs due to hybridization of single-atom orbitals resulting in the creation of bonding and anti-bonding states. Bonding (antibonding) states are hybrid states with electron density predominantly accumulated (depleted) in the region between the two atoms thus increasing (decreasing) the bond strength. The overlap population (OP) between two atoms is a quantity related to the overlap integral of their wave functions. Bonding (antibonding) states have a positive (negative) contribution to the OP[222]. A measure of the strength of molecular bonds is the overlap population weighted density of states commonly referred to as crystal orbital overlap population (COOP)[223,224].

Currents flowing through the bond alter the equilibrium electron distribution leading to an increased occupation of antibonding states hence reducing the COOP[225]. As a consequence, the bonds between a C_{60} molecule and its supporting electrode as well as the C–C bonds of the C_{60} are weakened. Further, the formation of a chemical bond between the two C_{60} molecules, i.e., the gradual occupation of bonding states, produces an attractive C_{60}–C_{60} bond force F_b, which increases in magnitude for decreasing C_{60}–C_{60} distance.

The interpretation of non-equilibrium forces would be consistent with Fig. 5.5, assuming non-equilibrium forces are responsible for the $z_c(V)$ shift. A larger background force, i.e., $F_{c,max}$, implies an increased contribution of conventional, i.e., van-der-Waals and electrostatic, forces. Consequently, the relative contribution of non-equilibrium forces and thus $\partial_V z_c$ decreases. In addition to that, the magnitude of non-equilibrium forces increases with increasing conductance, which agrees with the correlation of $\hat{G}_c$ with $\partial_V z_c$.

Recent DFT calculations[226] examined unrelaxed C_{60}–C_{60} contacts assuming a geometry comparable to previous calculations[17]. Current-induced bond forces F_b occurring between two C_{60} molecules were estimated. The magnitude of F_b amounts to $\sim$0.55 nN ($\sim$0.15 nN) at -1 V ($+1$ V) and a C–C distance of 0.2 nm. Non-equilibrium forces are short-range forces, which arise within $\sim$200 pm prior to z_c. Non-equilibrium forces also present an almost quadratic bias-dependence within ± 1 V and asymmetric geometries yield $F_b(V)$ parabolae that are not centered at zero bias[226]. With decreasing distance, the maximum of the $F_b(V)$ parabola shifts progressively toward positive voltages for C_{60} molecules attached to a planar surface and non-planar tips[226]. Hence, non-equilibrium forces may be responsible for the initial V_{max} increase [cf. $V_{max}(-0.3\,\text{nm} \lesssim z \lesssim 0.17\,\text{nm})$ in Fig. 5.3 **c**].

However, it is yet unclear if non-equilibrium forces lead to a $z_c(V)$ behavior as observed in the

present experiments. Further theoretical modeling is required in order to investigate the detailed impact of non-equilibrium forces occurring in molecular junctions. In particular, the consideration of relaxed junctions is pertinent, which was not included in ref. 226. Non-equilibrium forces not only lead to a direct bond force between both molecules, but also reduce the stiffness of each C_{60} as well as of the molecule-electrode interface.

Contribution of Multiple Effects

Naturally, several of the phenomena mentioned above may be operative simultaneously, reinforcing or attenuating each other. For example, currents weaken the electrode–molecule coupling which increases the elasticity of the electrode–molecule interface. Consequently, the electrode–molecule distance at constant force increases. However, an increased electrode–molecule separation in turn reduces the charge transferred from the electrode to the molecule, leading to a reduced force of (in)homogeneous electric fields on the molecule.

5.4. Conclusion

The vertical force during the formation of C_{60}–C_{60} contacts was examined as a function of the externally applied bias voltage. A linear shift of the point of maximum attraction z_c with V and a non-monotonic z-dependence of the maximum and curvature of $F(V)$ parabolae were observed, both of which have hitherto not been reported. Statistical analysis of several data sets exhibited correlations between the magnitude of the z_c shift and the bias-independent background force as well as junction conductance. Several possible mechanisms contributing to the experimental observations were listed and discussed. Bias-dependent atomic scale relaxations and their interplay with additional phenomena, such as current-induced effects, may provide a promising candidate for the explanation of the reported findings. A definitive assignment, however, requires further theoretical work.

Chapter 6

Lateral Force Spectroscopy of Single Atoms

The controlled lateral manipulation of single atoms or small molecules on metal surfaces using an STM tip presents virtually indefinite opportunities for studying physical processes at the single-atom level and the precise fabrication of structures at the ultimate size limit[227–238]. Due to the potential induced by the tip, energetically more favorable adsorption sites are temporarily created inducing movement of single atoms. Direct measurements of lateral forces at the nanoscale was reported by exciting the torsional oscillation of beam cantilevers[239,240] and quartz tuning forks oscillating parallel to the surface[241,242]. Such techniques are usually employed to measure friction forces and force profiles of stable nanostructures but are less suitable for the determination of the minimum lateral forces required to manipulate single atoms or molecules ($F_x^{\rightarrow}$) due to their lateral oscillation that reduces the lateral resolution. A superior approach consists of a tuning fork oscillating perpendicular to the surface. Here, the vertical force F_z is obtained from the frequency shift as a measure of the vertical stiffness. Integration of F_z yields the tip–sample interaction potential U enabling the determination of the lateral force as lateral derivative $F_x = -\partial_x U$. This method was introduced by Ternes *et al.*[11] in order to determine the lateral force required to move single Co atoms on Pt(111) and Cu(111) as well as single CO molecules on Cu(111). In subsequent experiments lateral forces acting on single molecules were examined[243–247].

The hypothesis motivating the work presented in this chapter comprises the conjecture of the dependence of the lateral manipulation force on the density of states of the substrate. Friction between two bodies entails energy dissipation. The dissipation of two atomically flat metallic bodies moving relative to each other in UHV may occur within two dissipation channels: electronic and phononic excitations[248–250]. The electronic contribution consists of excitations of electrons at the Fermi level. Hence, friction is expected to be influenced by the density of states at the Fermi level $\varrho(E_F)$. Two effects allow a precise engineering of $\varrho(E_F)$. First, in the superconducting state an energy gap Δ at E_F emerges reducing ϱ to zero within $E_F \pm \Delta$. The size of Δ decreases monotonically with temperature[22]. Moreover, introducing a magnetic field B leads to a decrease of Δ as well as a non-vanishing $\varrho(E_F)$ for elevated B[251–254]. Second, spin-flip scattering of conduction electrons at a magnetic impurity manifests itself as a zero-bias Kondo resonance[255–257].

Increasing the temperature continuously weakens the singlet Kondo ground state thus broadening the resonance[258–261] and consequently modifying $\varrho(E_F)$.

Previous experiments measuring the friction of N_2 films on Pb(111) using a quartz crystal microbalance (QCM) across the superconducting transition have shown a reduced friction force below the superconducting transition temperature T_c (ref. 19). Subsequent failure to reproduce the experiment[262] sparked debates concerning the presence of contaminants resulting in pinning of the N_2 films and the conclusion of the observations[20,263,264]. Recently, reduced dissipation on a macroscopic Nb surface below T_c as well as a characteristic distance- and bias-dependence of the dissipation was observed using a pendulum AFM[21]. The observations were attributed to a reduction in electronic friction in accordance with theoretical considerations. In the present work, the influence of the density of states at the Fermi level is studied by measuring the lateral manipulation force for adatoms on three face-centered cubic (fcc) metals: single Pb atoms on a superconducting Pb(111) sample as well as single Co atoms on Au(111) and Cu(111) with Co/Au(111) and Co/Cu(111) being Kondo systems. $\varrho(E_F)$ is controlled by varying the temperature as well as applying a magnetic field for experiments using Pb atoms on the superconducting Pb(111) sample.

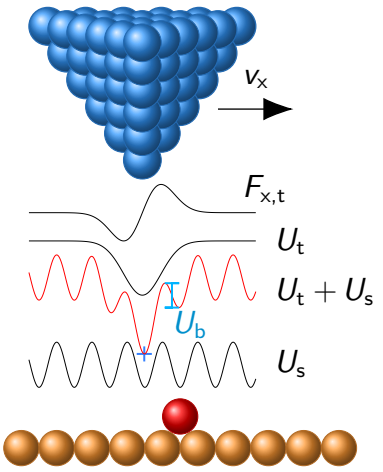

Figure 6.1. Illustration of the potential energy of tip U_t and substrate U_s as well as tip-induced lateral force $F_{x,t}$ in the context of lateral manipulation. The AFM tip (blue) is translated laterally at velocity v_x across the center of a single adatom (red sphere) adsorbed to the substrate (orange). The total potential energy (red line) exhibits an energy barrier U_b (light blue) between the adatom position and the energetically most favorable position below the lowermost tip atom (+).

The experimental approach concerning the determination of the lateral threshold force is outlined in Fig. 6.1. The AFM tip is laterally translated at constant height with a velocity of $20\,\mathrm{pm\,s^{-1}}$ across the center of a single atom along $\langle 1\,1\,\bar{2}\rangle$, i.e., manipulating between stable fcc and hexagonal close-packed (hcp) sites (cf. Fig. 6.2). Between subsequent scans, the tip height is reduced. The experiment is terminated once lateral manipulation occurs. During each scan along x for $z = \text{const.}$, the frequency shift as a measure of the vertical stiffness is recorded yielding two-dimensional data sets $\Delta f\,(x,z)$. For each x increment along the scan line, the vertical force F_z is then obtained by deconvolution using the method introduced by Sader and Jarvis[42] due to reduced noise amplification (cf. Section 2.4). Integrating F_z along z yields the tip–sample interaction potential U. Finally, the lateral force F_x is calculated by derivation along x, i.e., $F_x = -\partial_x U$.

6.1. Adsorption of Single Adatoms

The (111) surfaces of three different fcc metals were used in the experiments described below: Pb(111), Au(111), and Cu(111). The atomically resolved surfaces are shown in Fig. 6.3 **a-c**. The images are obtained by continuously manipulating a single adatom during the scan[233]. The atom is subject to the large potential caused by the close proximity of the tip. Consequently, the atom

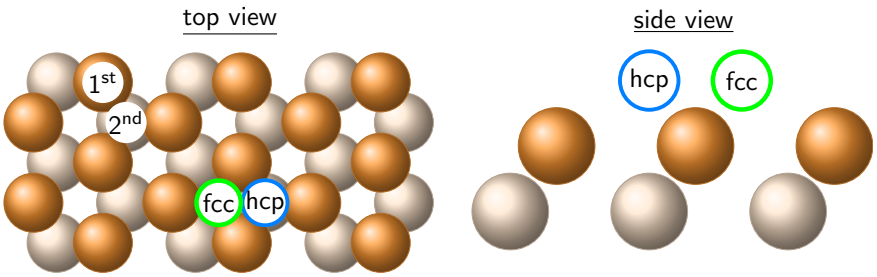

Figure 6.2. Sketch of the (111) surface of fcc metals. 1^{st} (2^{nd}) layer atoms are represented by (light) orange circles. One fcc (hcp) site is indicated as green (blue) circle.

is moved along the tip trajectory following the tip-induced potential minimum and temporarily residing in stable fcc or hcp sites. Top sites, representing local potential maxima, are avoided in favor of adjacent local minima. Therefore, the tip moves closer to the surface in order to pass the same current through the atom and the top site appears as depression. The energetically most favorable site (fcc for Cu[265,266], triangle in Fig. 6.3 **a**) where the atom resides predominantly appears as sphere[233]. The propensity of the atom to occupy fcc compared to hcp sites is reflected by the larger area marked by a triangle.

The image of the Au(111) surface (Fig. 6.3 **b**) shows no difference between fcc and hcp sites. Due to the strong bonding of single Au atoms to the Au(111) surface (cf. lateral force spectroscopy described below) a close tip–atom distance is required in order to continuously manipulate the atom. Consequently, the energy difference between fcc and hcp sites[267] is negligible in comparison to the potential induced by the tip. Imaging the Cu(111) surface using a Cu atom (cf. Fig. A.11 **c**) as well as Pt(111) using a Co atom[11] at close distances resembles the image of Au(111) (Fig. 6.3 **b**).

The Pb(111) image (Fig. 6.3 **c**) resembles the image obtained for Co/Cu(111). Previous density-functional theory calculations yielded the same total energy for fcc and hcp sites[268]. However, the asymmetry between fcc and hcp sites is clearly visible in Fig. 6.3 **c**. Previously, atomic point

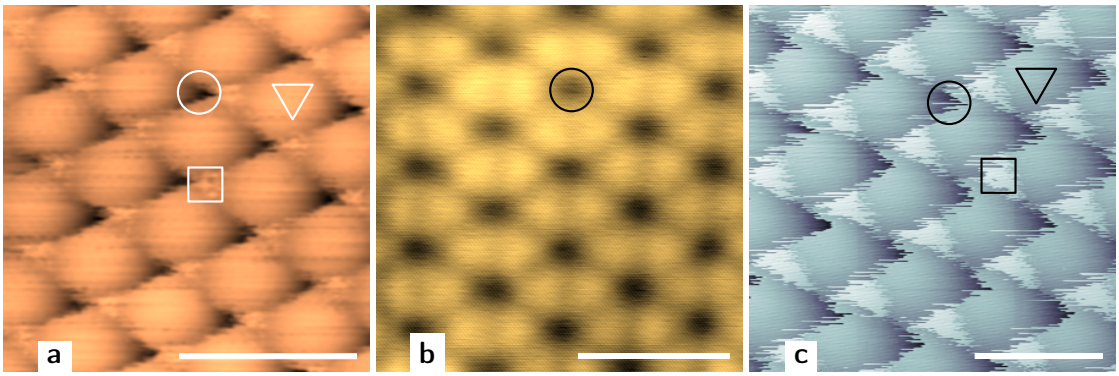

Figure 6.3. Constant-current topography of **a**, Cu(111), **b**, Au(111), and **c**, Pb(111). The images were obtained by trapping a single **a**, Co, **b**, Au, and **c**, Pb atom between the tip and the surface. Imaging parameters are **a**, 2 mV, 10 nA, **b**, 2 mV, 17 nA, and **c**, 1 mV, 3 nA, Triangles, squares, and circles denote fcc, hcp, and top sites, respectively. A 20 pt Gaussian filter was applied to **a**, a FFT filter for $r^{-1} \leqslant 0.01\,\mathrm{nm}^{-1}$ and $r^{-1} \geqslant 1.8\,\mathrm{nm}^{-1}$ to **b** ($r = \sqrt{x^2 + y^2}$, x and y representing the horizontal and vertical dimension, respectively). Scale bars: 0.5 nm.

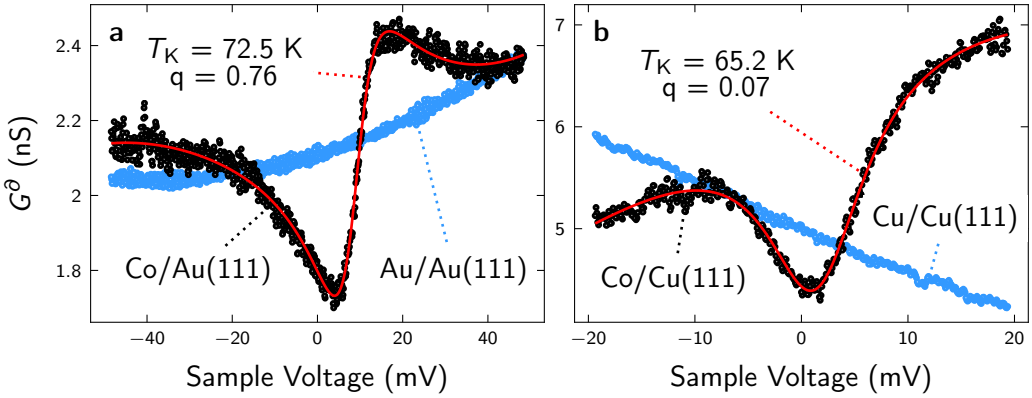

Figure 6.4. Differential conductance for **a**, Co/Au(111) (black), Au/Au(111) (blue), and **b**, Co/Cu(111) (black), Cu/Cu(111) (blue). The feedback loop has been disabled at **a**, 50 mV, 0.1 nA and **b**, 20 mV, 0.1 nA. Solid red lines denote Fano fits with fit parameters **a**, $T_K = 72.5 \pm 1.9\,\mathrm{K}$, $q = 0.76 \pm 0.03$, and **b**, $T_K = 65.2 \pm 2.7\,\mathrm{K}$, $q = 0.07 \pm 0.04$.

contacts between a Pb-covered tip and Pb(111) islands grown on Si(111) exhibited enhanced conductances at hcp sites compared to fcc sites[269]. Thus, areas indicated by squares in Fig. 6.3 **c** are assigned to hcp sites due to their elevated apparent height caused by enhanced conductivity. The preferential occupation of fcc compared to hcp sites indicates a lower potential of fcc sites similar to Cu(111) (cf. Fig. 6.3 **a**).

Co atoms were evaporated by means of an electron beam evaporator yielding Co densities of $0.04\,\mathrm{nm}^{-2}$ [Cu(111)] and $0.05\,\mathrm{nm}^{-2}$ [Au(111)]. Single substrate atoms were deposited from the tip after indenting the tip into the substrate thus coating the tip with substrate material[161].

Table 6.1. Fit parameter of the Fano fit of Fig. 6.4 and comparison with previously reported values.

	T_K (K)	q	Ref.
Co/Au(111)	72.5 ± 1.9	0.76 ± 0.03	Fig. 6.4 **a**
	67 ± 8	0.6 ± 0.1	[4]
	75 ± 6	0.60 ± 0.05	[270]
	76 ± 8	—	[271]
Co/Cu(111)	65.2 ± 2.7	0.07 ± 0.04	Fig. 6.4 **b**
	53 ± 5	—	[272]
	54 ± 2	0.18 ± 0.03	[273]
	61 ± 4	0.09 ± 0.03	[274]

Single Pb, Au, Cu, and Co atoms appear as circular symmetric protrusions. On Au(111) and Cu(111), single Au and Cu atoms can be distinguished from single Co atoms most reliably due to the presence of a Kondo resonance[255–257] around $V = 0$ (Fig. 6.4). While Au (Cu) atoms show no strong variation around zero bias, distinct features are clearly present in $G^\partial(\mathrm{V})$ data. A Fano fit of the experimental data yields fit parameters for the Kondo temperature T_K and asymmetry factor q in agreement with previously reported values (Tab. 6.1).

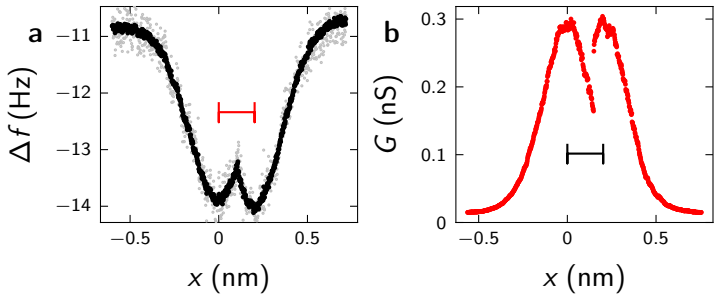

Figure 6.5. **a**, Frequency shift and **b**, conductance at the manipulation threshold of Pb/Pb(111). Raw (smoothed) data is shown in gray (black). The horizontal bars represent the fcc-hcp distance $\Delta x = 202\,\mathrm{pm}$. The feedback loop was disabled at 0.1 V, 56 pA and an additional piezo displacement of 195 pm applied. The tuning fork was operated at $f_0 = 29.9\,\mathrm{kHz}$, $A = 30\,\mathrm{pm}$.

6.2. Lateral Force Spectroscopy

The frequency shift Δf and corresponding conductance G measured at the manipulation threshold are shown in Fig. 6.5 for Pb/Pb(111). The tip is translated at constant height across the adatom center ($x = 0$) which is discernable as minimum (maximum) in Δf (G) data. With decreasing tip–adatom distance, Δf decreases due to increasing tip–adatom attraction at decreasing distances. G increases with decreasing tip–adatom distance. At $x \approx +140\,\mathrm{pm}$, a G discontinuity as well as a reversal of the Δf slope occurs signaling the displacement of the atom from its initial adsorption site. At the fcc-hcp distance $\Delta z = 202\,\mathrm{pm}$ a second Δf minimum as well as G maximum appears indicating the successful manipulation between fcc and hcp sites.

Fig. 6.6 **a** shows a series of Δf (x,z) data obtained for increasing piezo displacement z serving as basis for the determination of the lateral force required to move a single Pb atom. Due to the measurement noise the experimental data have been averaged within discrete steps (symbols) and fit to a series of gaussian functions (lines) prior to further processing. Special care was given to verify the absence of any systematic deviation from a gaussian-like profile, such as the two local maxima previously reported for vertical force profiles of flexible CO molecules on Cu(111)[11]. Δf (x,z=const.) data taken at $z < -300\,\mathrm{pm}$ were replaced by their mean value in order to further decrease scattering. At such distances, the influence of the adatom on Δf is not detectable.

The corresponding vertical tip–sample force F_z as well as the resulting tip–sample interaction potential U are shown in Fig. 6.6 **b**,**c**. Both F_z and U increase in magnitude with decreasing $|x|$ as well as increasing piezo displacement z, agreeing qualitatively with experiments for Co/Pt(111)[11]. The resulting lateral force F_x (Fig. 6.6 **d**) exhibits a point-symmetry around x=0. For x<0 (x>0), negative (positive) F_x values signal a force directed along $+x$ ($-x$) representing persisting attraction between tip and adatom.

At $x^{\rightarrow}$=−0.22 nm, manipulation of the atom occurs. Values of the vertical and lateral force at the manipulation amount to $F_z^{\rightarrow} = -0.39\,\mathrm{nN}$, $F_x^{\rightarrow} = 14.0\,\mathrm{pN}$. Frequency shift values and resulting lateral forces for Au/Au(111), Co/Au(111), Cu/Cu(111), and Co/Cu(111) are shown in Fig. A.15. Qualitative agreement is found for all adsorbate/substrate combinations studied in this work. In order to minimize the influence of the surface reconstruction of Au(111)[275,276], the experiments on this surface were performed in the center of fcc-like regions where the influence

of the soliton walls is lowest.

Lateral force spectroscopy for all adsorbate/substrate combinations was performed for different temperatures ranging from 5.8 K to 10 K. $F_x^{\rightarrow}$ as a function of temperature is shown in Fig. 6.7 **a**. A linear fit of the data reveals a decrease of $F_x^{\rightarrow}$ with T for all combinations (Fig. 6.7 **b**). This observation is supported by observations during STM imaging. Single Pb adatoms on Pb(111) remain stable during scanning up to ≈9 K. Above 9 K, the atoms occasionally move while scanning even at currents below 10 pA. This observation is in agreement with the linear extension of $F_x^{\rightarrow}$ (T) data, which intersects $F_x^{\rightarrow} = 0$ at 9.6 K (Tab. 6.4).

Fig. 6.7 **a** reveals data scattering especially for Au/Au(111), Co/Au(111), and Co/Cu(111) data. Recently reported lateral manipulation forces of CO/Cu(111) varied between 46 and 84 pN around 64 ± 10 pN (ref. 245) indicating a stochastic nature of the manipulation process. In the present experiment, scattering may be enhanced by experimental conditions. Lateral spectroscopy for Pb/Pb(111) and Cu/Cu(111) was performed on a pristine sample surface, whereas Au/Au(111) was studied with Co present at the surface. On Au (Cu), Co atoms were evaporated yielding a Co density of 0.05 nm^{-2} (0.04 nm^{-2}) and nearest-neighbor distance 2.5 ± 1.2 nm (2.2 ± 1.2 nm). Previously, a surface state-mediated long-range interaction of adjacent Cu atoms on Cu(111) has been reported for distances up to ≈6 nm (refs. 277,278). This observation is corroborated by DFT calculations of Cu atoms on Cu(111) that exhibit a modification of the migration barrier of isolated adatoms (50 meV) due to adjacent atoms in the range 41 to 69 meV (ref. 279). Although special care was given to ensure a distance to surrounding atoms of $\gtrsim$ 5 nm, the unavoidable presence of several atoms in the vicinity most likely modifies the fcc–hcp energy barrier and hence contributes to the data scattering. Moreover, the tip termination was shown to significantly

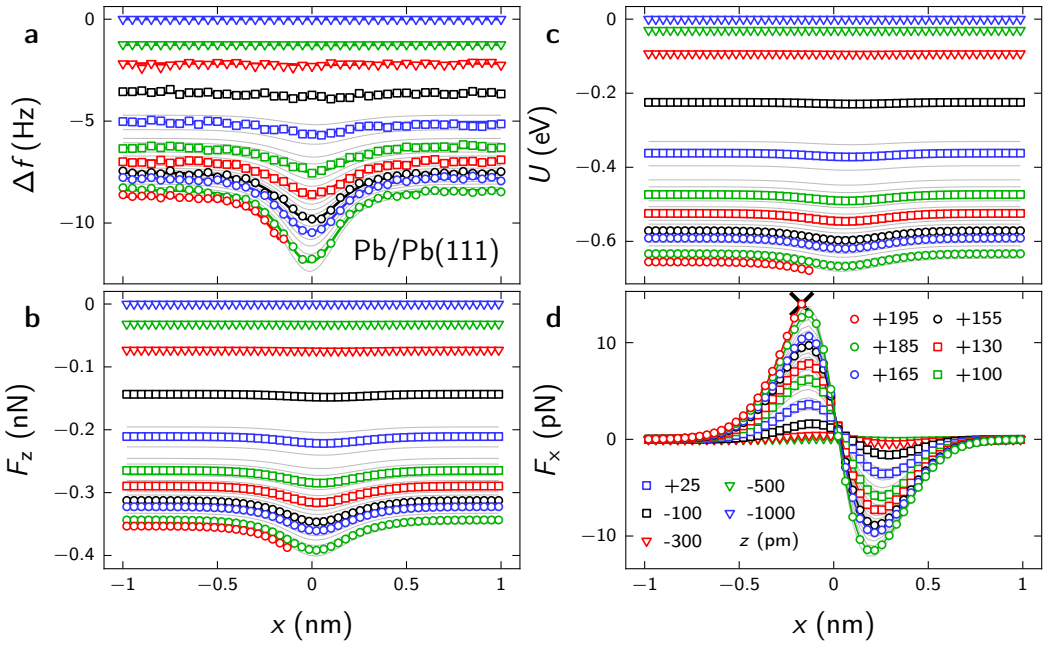

Figure 6.6. **a**, Δf, **b**, F_z, **c**, U, and **d**, F_x before manipulating a Pb atom on Pb(111) at $T = 5.9$ K. Circles, squares, and triangles in **a** denote experimental data for different z according to the legend in **d**. $z = 0$ corresponds to 0.1 V, 56 pA. Solid lines in **a** represent smoothed and interpolated data that serves as basis for the calculations shown in **b**-**d**. The cross in **d** indicates the manipulation. The force sensor was operated at $f_0 = 29.9$ kHz, $A = 30$ pm.

impact the lateral manipulation force. The lateral force of CO/Cu(111) measured using Cu(100), W(100), and Ir tips was reported as 61 ± 6 pN, 76 ± 2 pN, and 160 ± 30 pN, respectively[11,245]. The present experiments were performed with a bulk PtIr tip which may be coated with substrate material due to substrate-immersion prior to the experiments. Additionally, the presence of trace amounts of Pb, Au, and/or Cu cannot be excluded.

Previously, the lateral force required to move a single Co atom on Cu(111) was reported as 17 ± 3 pN at 5 K (ref. 11). A linear extension of the present data leads to a value of 15.9 pN at 5 K in close agreement with Ternes *et al.*[11]. Temperate-dependent lateral force spectroscopy of single CO molecules on Cu(111) exhibited a force decreasing by -1.7 pN/K (ref. 245) matching the magnitude observed in this work (cf. Tab. 6.4).

Lateral manipulation forces obtained in the present experiments are lower by one order of magnitude than previously reported for Co on Pt(111)[11]. Pb, Au, Cu, and Pt are fcc metals. Single metal adatoms adsorb to a threefold coordinated hollow site on fcc(111) surfaces. Chemical bonding between a metal and a single adatom occurs due to the interaction of electronic states of the metal with states of the atom. New hybrid states are formed that can be divided into bonding and antibonding states. The binding strength decreases with increasing occupation of antibonding states. Metal states close to the Fermi level are relevant for the determination of the binding strength since they permit occupied bonding and unoccupied antibonding hybrid states. Previously, the enhanced stability of single Co adatoms on Pt(111) compared to Cu(111) has been assigned to the orbital character of the metal bonds[11]. Spatially localized Pt d-orbitals were

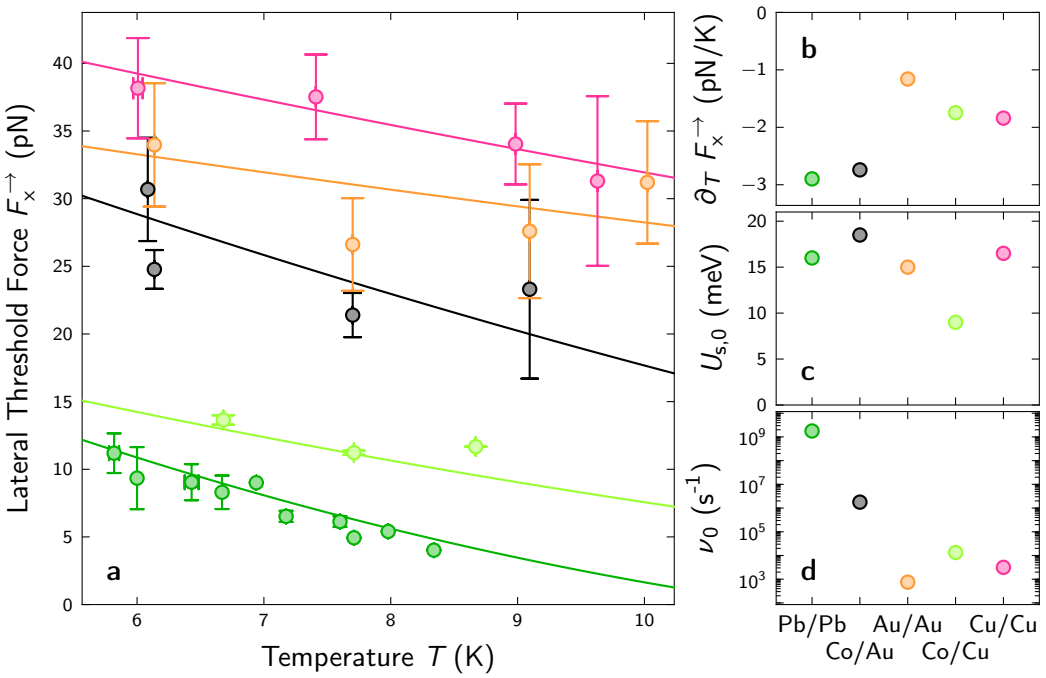

Figure 6.7. **a**, Lateral force $F_x^{\rightarrow}$ at the manipulation threshold as a function of temperature T (circles). Squares (error bars) denote mean values (standard deviations) of several data sets. Solid lines denote fits according to the lateral force model for variable attempt frequency ν_0 and potential amplitude $U_{s,0}$. **b**, Linear slope of $F_x^{\rightarrow}$. **c**, Amplitude of the sinusoidal sample potential $U_{s,0}$ and **d**, attempt frequency ν_0 obtained by matching the experimental data to the lateral force model.

expected to strengthen the adatom-substrate bond compared to delocalized Cu s-orbitals.

This argument is in agreement with the present observations. Pb, Cu, and Au exhibit a low density of states of d-wave (e_g, t_{2g}) character at the Fermi level in stark contrast to Pt (cf. Tab. 6.2). Moreover, Pt d-bands are only partially filled permitting a high bonding/antibonding filling ratio[280,281]. Pb has virtually no density of d-states at the Fermi level[280]. Bonding of Pb atoms to the Pb(111) surface occurs primarily via weak sp^3 bonds[268] whereas Cu–Cu and Au–Au bonding is dominated by more robust s-d hybrid bonds[282]. The significantly lower $F_x^{\rightarrow}$ of Pb/Pb(111) compared to Au/Au(111) and Cu/Cu(111) observed in the present experiments corroborates the argument presented above. The increased stability of Cu/Cu(111) compared to Au/Au(111) is consistent with the higher elasticity of Au chains[161,165] assigned to relativistic corrections important for 5d elements[283].

	s	p	e_g	t_{2g}
Cu	0.06	0.09	0.10	0.04
Au	0.07	0.04	0.13	0.05
Pb	0.05	0.44	0.00	0.00
Pt	0.02	0.03	1.65	0.51

Table 6.2. Density of states at the Fermi level (in units of states per eV) derived from tight-binding calculations[280] separated by orbital character.

The manipulation force for Co/Au(111) exceeds that for Co/Cu(111) by a factor of ≈2. This result is contrary to expectations based on the enhanced nobleness of Au compared to Cu[281] as well as approximations of the d-state occupation of Co on Au(111) and Cu(111) consistent with the measured Kondo temperatures[284]. The behavior is most likely caused by a variation of the adsorbate-induced shift of the states near the Fermi level due to different hybridization with the substrate. DFT calculations of the total binding energies for Co/Cu(111) and Co/Au(111) yielded higher values for Co/Au(111) [∼4 eV, ref. 285] compared to Co/Cu(111) [∼3.2 eV, ref. 286] matching the experimentally observed trend.

The temperature-dependence of the lateral manipulation force is reminiscent of the process of surface diffusion. Thermally activated diffusion is commonly described using transition state theory[287–289]. The temperature-dependence of the event or hopping rate ν between two sites separated by a migration barrier E_m is expressed as $\nu = \nu_0 \exp\left(-E_m k_B^{-1} T^{-1}\right)$ with Boltzmann constant k_b and temperature-independent[288] attempt frequency ν_0. ν increases with temperature representing thermal activation of the diffusion process. A decrease of the lateral force required to manipulate single atoms with increasing temperature concurs with increased thermal activation.

Lateral force measurements at the sub-nm range commonly termed atomic scale friction are usually analyzed within the Prandtl-Tomlinson[290,291] (PT) model[292–297] or modified versions thereof[298–304]. The conventional setup of this model consists of two electrodes and a small probe. The probe is coupled to the top electrode by a spring and perpetually moved through the periodic potential of the bottom electrode, performing repeated manipulation events between local potential minima. Commonly, the PT model is applied in order to analyze the friction force, which is defined as time-averaged lateral force $\langle F_x \rangle$. An analytical expression for $\langle F_x \rangle$ exists, which predicts a decline proportional to $-T^{2/3}$ (ref. 293). In the present experiments however, the determined quantity is the maximum lateral force prior to the manipulation $F_x^{\rightarrow} = \max F_x$. No analytical expression for $F_x^{\rightarrow}$ exists to date.

Alternatively, the PT model may be evaluated numerically[305]. Commonly, the PT model is applied for a probe mass of the order $m \sim 10^{-12}$ kg, amplitude of the periodic potential $U_0 \sim 1$ eV,

and sliding speeds $1\,\mathrm{nm/s} \leq v \leq 1\,\mathrm{m/s}$ (ref. 293–297). However, the values appropriate for the description of the present experiment differ significantly. The mass of the adatom is of the order $\sim 100\,u$ (u - atomic mass; $m_{\mathrm{Cu}} = 63.5\,u$, $m_{\mathrm{Au}} = 196.7\,u$, $m_{\mathrm{Pb}} = 207.2\,u$). Moreover, $U_0 \sim 10\,\mathrm{meV}$ and $v = 20\,\mathrm{pm/s}$.

For the numerical implementation of the model, several time scales have to be considered. The PT probe is subjected to the periodic sample potential, which results in an oscillation period $\hat{t}_{\mathrm{o}} = \sqrt{ma^2U_0^{-1}}$ (ref. 293, a - periodicity of the potential). Additionally, the coupling of the probe to the top electrode with a spring of stiffness k yields a resonance period $\hat{t}_{\mathrm{r}} = \sqrt{mk^{-1}}$ (ref. 293).

A numerical implementation requires time steps δt lower than the relevant time scales, usually of the order $0.001 \cdot \hat{t}_{\mathrm{o}} \leqslant \delta t \leqslant 0.01 \cdot \hat{t}_{\mathrm{o}}$ (ref. 293). The second column in Tab. 6.3 presents evaluated values applicable for common friction experiments. Relevant time scales are of the order $10^{-6}\,\mathrm{s}$. In contrast, values appropriate for the present experiments yield significantly lower $\hat{t}$ of the order $10^{-12}\,\mathrm{s}$ (thir d column).

Table 6.3. Evaluation of time scales pertinent for a numerical implementation of the PT model for different input parameters. v - speed of the top electrode. a - periodicity of the potential. m - mass of the probe. U_0 - amplitude of the potential. k - spring constant. $\hat{t}_{\mathrm{o}}$ - oscillation period of m in the periodic potential. $\hat{t}_{\mathrm{r}}$ - resonance period of k coupled to the top electrode with a spring of stiffness k.

Variable	Value 1	Value 2
v	$10\,\mathrm{nm/s}$	$20\,\mathrm{pm/s}$
a	$200\,\mathrm{pm}$	$200\,\mathrm{pm}$
m	$10^{-12}\,\mathrm{kg}$	$100\,u$
U_0	$1\,\mathrm{eV}$	$10\,\mathrm{meV}$
k	$1\,\mathrm{N/m}$	$1\,\mathrm{N/m}$
$\hat{t}_{\mathrm{o}}$	$5 \cdot 10^{-7}\,\mathrm{s}$	$2 \cdot 10^{-12}\,\mathrm{s}$
$\hat{t}_{\mathrm{r}}$	$1 \cdot 10^{-6}\,\mathrm{s}$	$4 \cdot 10^{-13}\,\mathrm{s}$

A single manipulation event between fcc and hcp sites ($\Delta x \sim 200\,\mathrm{pm}$) at a tip velocity $v = 20\,\mathrm{pm/s}$ has a duration of $t_{\mathrm{ges}} = 10\,\mathrm{s}$. With $\delta t = 0.01 \cdot \hat{t}_{\mathrm{r}} = 4 \cdot 10^{-15}\,\mathrm{s}$ a total of $N = t_{\mathrm{ges}}/\delta t = 2.5 \cdot 10^{15}$ simulation steps are required for the numerical implementation of a single manipulation event. With the available computational infrastructure, evaluating a single step requires $\sim 10^{-7}\,\mathrm{s}$, which corresponds to a total duration for the simulation of a single manipulation event of 7.8 years. And, statistical analysis of multiple manipulation events and the evaluation for several input parameter sets is required in order to compare the model to the experimental data. Hence, a numerical approach applying the PT model to the present experiment is not feasible.

In the following, a simple microscopic model for the lateral manipulation of single atoms termed "lateral force model" is developed.

6.3. Lateral Force Model

The model system considered here is outlined in Fig. 6.1. Two dimensions, $\vec{e}_x$ parallel and $\vec{e}_z$ perpendicular to the surface, are regarded. The periodic crystal surface is represented by a sinusoidal potential U_{s} with peak-peak amplitude $U_{\mathrm{s},0}$ and periodicity a_{s} featuring a minimum at $x = 0$.

$$U_{\mathrm{s}} = -U_{\mathrm{s},0}/2 \cdot \cos(2\pi x/a_{\mathrm{s}}) \tag{6.1}$$

The tip-induced potential is modeled as a gaussian of amplitude $U_{t,0}$ and width a_t centered at the tip position x_t.

$$U_t = -U_{t,0} \cdot \exp\left(-[(x - x_t)/a_t]^2\right) \tag{6.2}$$

The total potential U_{tot} consists of the linear superposition of both contributions.

$$U_{tot} = U_s + U_t \tag{6.3}$$

As visualized in Fig. 6.1, the initial adsorption site of the atom $x_{ad} = 0$ is separated from the energetically most favorable adsorption site below the tip apex ($x_{ad} \approx x_t = -a$) by an energy barrier U_b. Thermal activation of the hopping process is incorporated via the event rate ν, which is proportional to the constant attempt frequency ν_0 following the approach common in transition state theory[287–289].

$$\nu = \nu_0 \cdot \exp\left(-U_b/k_b T\right) \tag{6.4}$$

The expression can be rewritten in order to calculate a mean duration between hopping events, $\Delta\tilde{t}$.

$$\Delta\tilde{t} = \nu^{-1} = \nu_0^{-1} \cdot \exp\left(+U_b/k_b T\right) \tag{6.5}$$

For the model calculations, a discretization of lateral step width $\Delta x = 1\,\mathrm{pm}$ was chosen. The tip is located within Δx for the duration Δt.

$$\Delta t = \frac{\Delta x}{v_x} \tag{6.6}$$

On average, one jump over a barrier $U_b^{(min)}$ occurs during $\Delta t = \Delta\tilde{t}$.

$$U_b^{(min)} = k_b T \cdot \ln\left(\nu_0 \frac{\Delta x}{v_x}\right) \tag{6.7}$$

$U_b^{(min)}$ represents the temperature-dependent threshold barrier that yields the termination condition for the model iteration

$$U_b^{(min)} \geqslant U_b \tag{6.8}$$

Due to the arbitrary choice of Δx, ν_0 has qualitative rather than quantitative physical meaning. Eq. (6.7) reveals a linear relation between the minimum barrier height $U_b^{(min)}$ and the thermal energy $k_b T$. The magnitude of thermal activation depends on the attempt frequency ν_0 as well as the lateral velocity v_x. The iteration process for calculating the lateral manipulation force within the lateral force model is outlined in Fig. 6.8. Upon reaching the termination condition [eq. (6.8)], the lateral force between tip and adatom is calculated as lateral derivative of the tip-induced potential U_t evaluated at the position of the adatom x_{ad} that resides in the local energy minimum at $x_{ad} \approx 0$.

Exemplary results obtained within the lateral force model are shown in Fig. 6.9 (temperature- and velocity-dependences are shown in Fig. A.18, the temperature-dependence is also visible in

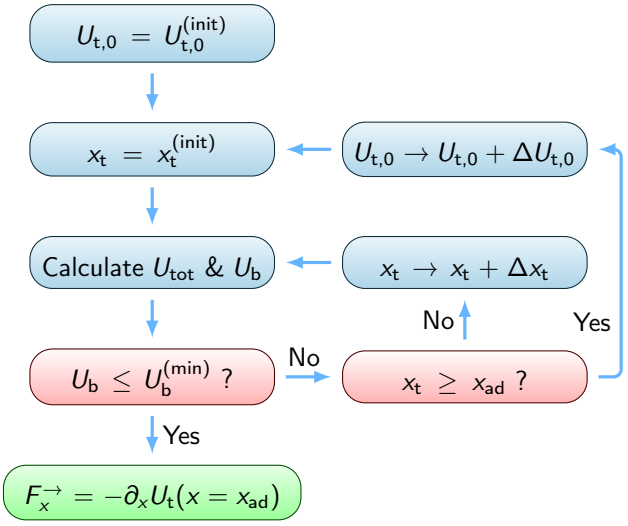

Figure 6.8. Flowchart illustrating the lateral force model iteration process. The iteration is initialized with $U_{t,0} = U_{t,0}^{(init)}$. The tip position x_t is then increased from $x_t^{(init)}$ to $x_t = x_{ad}$ in steps of Δx_t. During each step, the total potential U_{tot} is calculated and the energy barrier U_b evaluated. Then, the tip potential amplitude is increased by $\Delta U_{t,0}$. The process is successfully terminated when $U_b^{(min)}$ exceeds U_b. Finally, $F_x^{\rightarrow}$ is evaluated as lateral derivative of the tip–induced potential at the position of the adatom x_{ad}.

Fig. 6.7). Fig. 6.9 **a** reveals the impact of the sample potential periodicity on $F_x^{\rightarrow}$. Recently, the lateral force threshold for moving CO on Cu(111) was estimated using a simple approximation [245]. A sinusoidal potential $U_s^{(sin)} = U_{s,0}/2 \sin(2\pi x/a_s)$ was employed to estimate the lateral force $F_x^{(sin)} = -\partial_x U_s^{(sin)} = -\pi U_{s,0} a_s^{-1} \cos(2\pi x/a_s)$ that exhibits a maximum of $\left|F_{x,max}^{(sin)}\right| = \pi U_{s,0} a_s^{-1}$. At $T = 0$, the lateral force model matches the hyperbolic behavior $F_x^{\rightarrow} \propto a_s^{-1}$ obtained using this estimate. With rising temperature, thermal activation increasingly assists the manipulation process and the required force declines. The linear relationship between $F_x^{\rightarrow}$ and the sample potential amplitude is shown in Fig. 6.9 **b**. A linear increase of $F_x^{\rightarrow}$ for $F_x^{\rightarrow} > 0$ is compatible with the generally linear connection of force and potential. The magnitude of thermal activation depends on the attempt frequency ν_0 (Fig. 6.9 **c**). Hence, the decline of $F_x^{\rightarrow}(T)$ increases with ν_0, which is in agreement with transition-state theory (TST). TST predicts an increasing diffusion rate for higher attempt frequencies ν_0 (ref. 288). Moreover, the lateral manipulation force is virtually independent of the tip radius which enters the model via a_t (Fig. 6.9 **d**). This result is consistent with the previously reported insensitivity of the manipulation threshold to the vertical force [11]. The

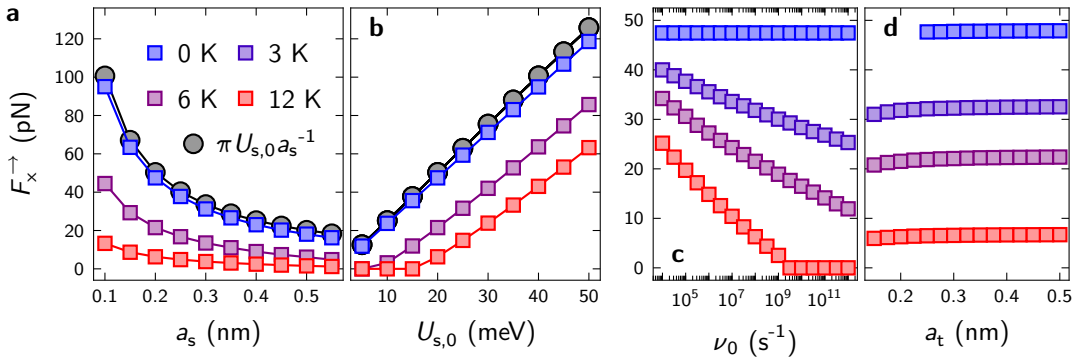

Figure 6.9. Lateral forces evaluated within the lateral force model. Input parameters are $v = 20\,\mathrm{pm/s}$, $U_{s,0} = 20\,\mathrm{meV}$, $a_{s,t} = 200\,\mathrm{pm}$, and $\nu_0 = 10^8\,\mathrm{s}^{-1}$ unless indicated otherwise on the x axes. Different temperatures 0 K, 3 K, 6 K, and 12 K were employed and colored according to the description in **a**. Black corresponds to the maximum force induced by a sinusoidal potential of peak-peak amplitude $U_{s,0}$ and periodicity a_s.

vertical force increases with the tip radius r_t due to the linear dependence of electrostatic and van-der-Waals forces on r_t. Fig. 6.9 **a-d** reveal the general trend of decreasing $F_x^{\rightarrow}$ with increasing temperature which is in agreement with increasing thermal activation.

	$\partial_T F_x^{\rightarrow}$ (pN/K)	$F_{x,0}^{\rightarrow}$ (pN)	T_0 (K)	a_m (pm)	ν_0 (s^{-1})	$U_{s,0}$ (meV)
Pb/Pb(111)	-2.9 ± 0.5	28 ± 3	9.6	202	$2 \cdot 10^9$	16.0
Co/Au(111)	-2.7 ± 2.3	45 ± 16	16	167	$2 \cdot 10^6$	18.5
Au/Au(111)	-1.2 ± 1.7	40 ± 13	34	167	$7 \cdot 10^2$	15.0
Co/Cu(111)	-1.7 ± 2.2	25 ± 16	14	147	$1 \cdot 10^4$	9.0
Cu/Cu(111)	-1.8 ± 1.8	50 ± 15	27	147	$3 \cdot 10^3$	16.5
CO/Cu(111)[245]	-1.7	84	50	255		

Table 6.4. Evaluation of the temperature-dependence of the lateral force spectroscopy. $\partial_T F_x^{\rightarrow}$ represents the linear slope of $F_x^{\rightarrow}(T)$. $F_{x,0}^{\rightarrow}$ [T_0] equals $F_x^{\rightarrow}(T=0)$ [$T(F_x^{\rightarrow}=0)$] obtained from a linear fit. a_m denotes the manipulation distance, i.e., fcc-hcp distance for metal atoms, top-top distance for CO/Cu(111). $U_{s,0}$ and ν_0 are obtained from a fit to the lateral force model.

The lateral force model was evaluated for

$$U_{s,0} \in [5, 30]\,\text{meV} \quad \text{in steps} \quad \Delta U_{s,0} = 0.5\,\text{meV and}$$
$$\lg\left[\nu_0(s^{-1})\right] \in [2, 12] \quad \text{in steps} \quad \Delta \lg\left[\nu_0(s^{-1})\right] = 0.125$$

using the fcc-hcp distance for a_s (Pb: 202 pm, Au: 167 pm, Cu: 147 pm). The resulting $F_x^{\rightarrow}(T)$ data was matched to the experimental data minimizing the mean square deviation χ^2 (lines in Fig. 6.7 **a**). The sample potential amplitude $U_{s,0}$ and attempt frequency ν_0 obtained in this manner are displayed in Fig. 6.7 **c,d** and listed in Tab. 6.4. Due to the limited temperature range, there is no unambiguous minimum but a trench of low χ^2 values (Fig. 6.10).

Values for $U_{s,0}$ (10 to 20 meV) are of the same order of magnitude as diffusion migration barriers E_m previously reported for Co and Cu on Cu(111) in theoretical[265,279,306,307] and experimental[11,277,278] investigations (35 to 50 meV). ν_0 differs by more than six orders of magnitude for different adsorbate–substrate combinations. This result is not surprising, since ν_0 for different systems and obtained with the same method may vary by 10 orders of magnitude[308].

Table 6.5. Comparison of migration barrier E_m for Cu and Co on Cu(111) obtained with different experimental and theoretical methods. The temperature (range) present in the experiments is indicated. [a] Tracer diffusion analysis using STM images. [b] Embedded atom method. [c] Second moment approximation of the tight binding theory. [d] Molecular static method.

	E_m (meV)		T (K)	Ref.
Cu	37 ± 5	STM[a]	[9,21]	277
	40 ± 1	STM[a]	[13,14]	278
	41	EAM[b]		306
	50	DFT		279
Co	35 ± 5	AFM	5	11
	37	2M[c]		265
	40	MS[d]		307

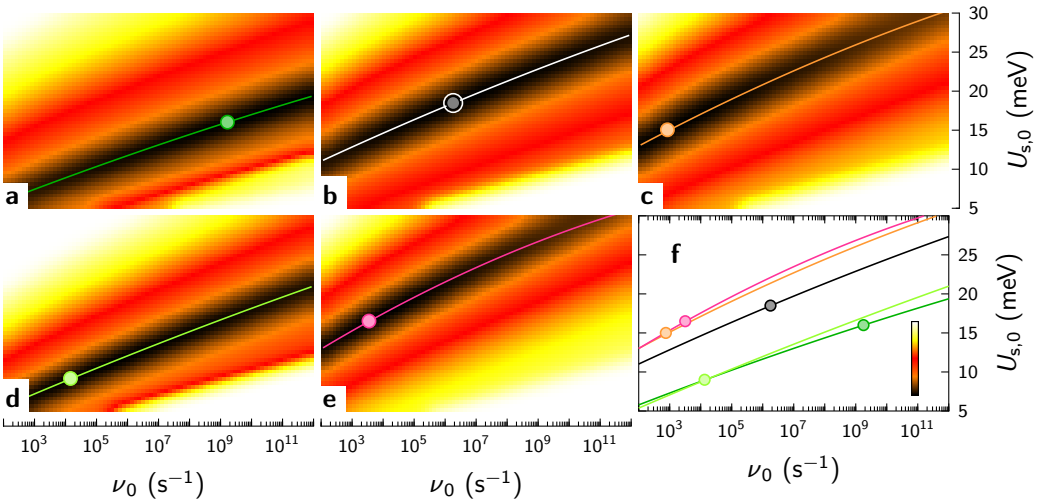

Figure 6.10. **a**-**e**, $\sqrt{\chi^2}$ maps for the data presented in Fig. 6.7. **a**, Pb/Pb(111), **b**, Co/Au(111), **c**, Au/Au(111), **d**, Cu/Cu(111), **e**, Co/Cu(111). Solid lines in **a**-**f** denote the best match as a function of ν_0. The absolute χ^2 minimum for each adsorbate–substrate combination is indicated as circle. The colorbar is shown as inset of **f** and ranges from 0 pN (black) to 50 pN (white).

Barriers for Co/Cu(111) and Cu/Cu(111) obtained using the lateral force model are lower than those reported for diffusion obtained theoretically[265,279,306,307] as well as experimentally[11,277,278] at low temperatures (cf. Tab. 6.5). Several aspects may contribute to this deviation. First, the sample potential acting on a single atom is not perfectly described by a sinusoidal[11]. However, replacing the sinusoidal potential by a periodic potential with either reduced or increased barrier width within the model only increases the lateral threshold force. Second, the presence of the tip influences the bonding of the atom to the substrate, in addition to the modification of the substrate potential. Due to the tip-induced electric and dipole fields as well as the increased atom-surface distance caused by attraction to the tip, charge reorientation and consequently variation of the bond strength occurs. Third, recent experiments exposed the influence of the chemical composition as well as shape of the tip on the lateral force required to move CO/Cu(111)[245]. In addition to the atom-substrate bonding, the bonding between atom and tip evidently impacts the lateral threshold force. Fourth, athermal excitations due to instrumental noise contributions[38] such as mechanical vibrations, acoustic noise, and electromagnetic interference provide additional energy reducing the effective barrier. A model calculation studying atomic friction revealed a plateau of the friction force at low temperatures[309].

6.4. Influence of the Density of States at the Fermi Level

In order to examine the impact of the density of states at the Fermi level $\varrho(E_F)$ on $F_x^{\rightarrow}$, additional experiments were performed for different magnetic fields. Within the experimental uncertainty, $F_x^{\rightarrow}$ is insensitive to B (Fig. 6.11 **a**). The critical field of Pb at 6 K is evaluated according to[23,310]

$$B_c(T) = 80.3\,\mathrm{mT} \cdot \left[1 - \left(\frac{T}{T_c}\right)^2\right] = 24.6\,\mathrm{mT} \tag{6.9}$$

(cf. Fig. 6.11 **b**) and indicated by orange lines in Fig. 6.11 **a,b**. Across B_c, no evolution comparable to the variation of the dissipation across T_c observed in a previous pendulum AFM experiment[21] occurs. Moreover, temperature-dependent measurements (Fig. 6.7) show a linear decrease without features around $T_c = 7.2\,\mathrm{K}$, comparable for superconducting Pb as well as non-superconducting Au and Cu substrates. Consequently, the present data imply the absence of any significant impact of the density of states on the lateral manipulation force of single atoms.

This finding is in stark contradiction to the significant drop of the friction across the transition into the superconducting state reported for QCM experiments examining N_2 films on Pb[19,20] and the dissipation measured in a macroscopic pendulum AFM experiment above a Nb sample[21]. The main difference to the present examination consists of the continuous nature of the previous experiments. The QCM as well as the AFM pendulum are continuously excited thus probing dynamic friction. In the present case, a single atom is displaced from its initial binding site and moved to the closest adjacent binding site. Hence, the present experiment bears closer resemblance to *static friction* phenomena. In aforementioned dynamic friction experiments, the dynamic interaction between film/tip and substrate causes dissipative drag forces that are not relevant in the present experiment. The oscillating electromagnetic potential caused by the multipole moments present in N_2 films induces oscillating electric currents in the Pb substrate[20,311,312]. Electric currents are subject to Ohmic losses that vanish for $T < T_c$. In the normal state, the induced charge cloud does not follow the adsorbate motion instantaneously thus exerting a damping force on the film motion. In the case of the pendulum experiment, the oscillating electromagnetic field interacts with the ion cores thus exciting surface acoustic phonons that interact only with normal electrons near the Fermi level[21,248]. The density of normal electrons decreases significantly below T_c, which entails a decreasing electron-phonon scattering and consequently phonon excitation energy. The latter is provided by the electromagnetic field of the pendulum leading to damping

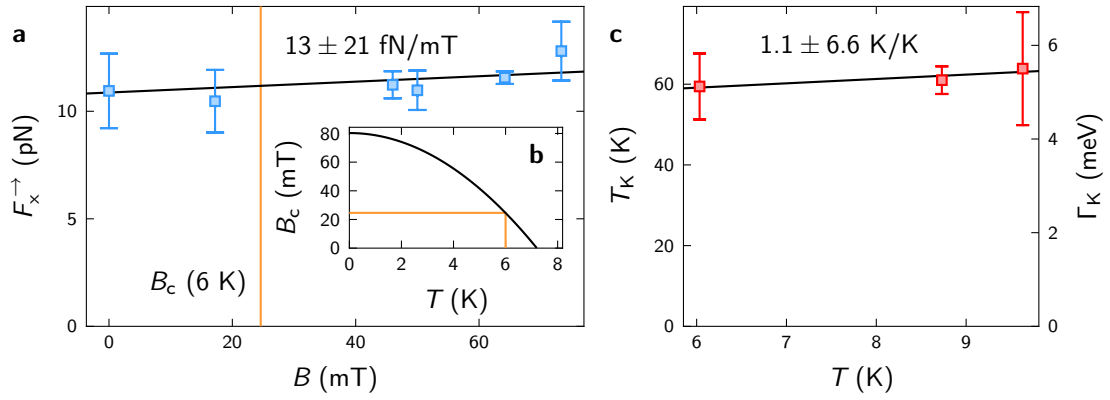

Figure 6.11. **a**, Lateral threshold force (blue squares) as a function of magnetic field B. A slope of $13 \pm 21\,\mathrm{fN/mT}$ is obtained from a linear fit of the data (black line). The critical field at 6 K is indicated as orange line. **b**, Temperate-dependence of the critical field B_c using $B_{c,0} = 80.3\,\mathrm{mT}$ valid for Pb[310]. The construction for the critical field at 6 K is indicated as orange line. **c**, Temperate-dependence of the Kondo temperature $T_K = k_B^{-1}\Gamma_K$ extracted from Fano fits (red squares) for Co/Cu(111). A slope of $1.1 \pm 6.6\,\mathrm{K/K}$ is obtained from a linear fit of the data (black). The data in **a** [**c**] present mean value (squares) and standard deviation (error bars) for several measurements at each B [T].

of the pendulum motion. In the present case, the atom moves to the nearest local potential minimum virtually instantaneously far exceeding the time and length scales required to experience the retroactive effects necessary for the observations of refs. 19–21.

The temperature range accessible in the current experimental setup proofed insufficient for the determination of the impact of the Kondo effect on the lateral force. The Kondo temperature, which represents a measure of the width of the Kondo resonance and thus the presumed impact of the Kondo effect on $\varrho(E_F)$, varies only weakly between 6 K and 10 K (Fig. 6.11 **c**). The increase of 1.1 K/K is of the same order of magnitude as theoretically expected for $T_K = 65.2$ K, which amounts to 0.8 K/K between 6 and 10 K (ref. 260,261). Comparing Pb/Pb(111), Au/Au(111), and Cu/Cu(111) to Co/Au(111) and Co/Cu(111) data suggests a dominant contribution of the temperature to the variation of $F_x^{\rightarrow}$. Hence, no impact of the Kondo effect is observed within this temperature range.

6.5. Investigation of Additional Effects

Special care was given to ensure that the observations reported above do not originate from effects introduced or masked by changes induced by variation of the temperature and the magnetic field. The temperature affects the resonance frequency f_0 of the tuning fork[313]. In the present experiments, a change of -0.12 ± 0.04 Hz/K occurred in the measurement range, 5.8 to 10 K, in close agreement with recently reported variations at low temperatures[314]. The f_0 shift was compensated thus accounting for the thermal impact on f_0.

No variation of the measured oscillation amplitude at fixed excitation, the quality factor Q, and the excitation energy was observed between 5.8 and 10 K as well as in magnetic fields up to 100 mT. Recently, the tuning fork calibration was found independent of temperature below ∼10 K as well[314].

An additional effect might arise due to changes of the piezo constant $\mathfrak{c}$. Since determination of the lateral force in the present case requires spatial integration as well as derivation, $\mathfrak{c}$ modifications alter the magnitude of F_x. Variations of $\mathfrak{c}$ were tracked by analyzing constant-current images and evaluating line profiles of the atoms during the variation of T and B. While the FWHM and height of single atoms scattered by ±0.5%, no statistical deviations were observed between 5.8 and 10 K and in magnetic fields up to 100 mT.

6.6. Conclusion

The lateral force required to move single atoms was examined on Pb(111), Au(111), and Cu(111). The character of the substrate–atom bond was related to the binding strength. The lateral manipulation force is reduced by thermal activation. A simple model calculation of temperature-dependent manipulation reproduces the experimental results. No influence of the density of states at the Fermi level on the lateral force could be observed with the tuning fork sensor.

Chapter 7

Conclusions and Prospects

The present thesis is devoted to the optimization of a combined scanning tunneling and atomic force microscope. While the initial setup featured considerable athermal disturbances, operation of the microscope with significantly enhanced performance was achieved by substantially improving the thermal anchoring of the microscope to the bath cryostat and reducing mechanical as well as electric noise. Specifically, the base and effective temperatures were reduced by 17% and 52%, respectively. The present state of the system provides an energy resolution which corresponds to the thermal limit. The tuning fork signal noise was lowered by 86%. Stable operation of the tuning fork at oscillation amplitudes as low as 20 pm and piconewton resolution is now feasible, which compares to state-of-the-art atomic force microscopes.

The experimental part of the present thesis explores Andreev reflection and atomic forces at the single–atom and single–molecule level. The formation of controlled contacts to single C_{60} molecules on a Nb(110) surface is accompanied by the gradual transformation of the superconducting energy gap into a zero–bias peak. Spectroscopic measurements are consistent with the presence of Andreev reflection in atomic–scale junctions. The conventional, single–channel BTK model is in excellent agreement with data obtained for single–atom and single–molecule contacts. Careful analysis of the differential and total conductances enables the detection of subtle variations attributed to the C_{60} orientation and the termination of the tip apex. The results present a novel approach for the determination of the minimum number of transport channels contributing to charge transport across a $\mathcal{NS}$ interface. Theoretical modeling revealed the impact of transport channels with varying transmission on the results obtained from a single-channel BTK analysis.

Furthermore, vertical forces during the formation of C_{60}–C_{60} contacts in the presence of an electric field were examined. For the first time, the impact of an externally applied bias voltage on force characteristics during the formation of single-molecule contacts was observed. The data evidence the presence of hitherto unexplored phenomena. Several possible contributions to the observations were outlined and discussed. Further experimental and/or theoretical work is required in order to capture the relevant physics. Experimentally, the examination of certain molecules could provide deeper insights. The impact of inhomogeneous electric fields on atomic–scale dipoles can be probed by measuring forces during contacts to polar molecules such as carbon monoxide. Current–induced forces may be explored in detail by modifying the C_{60} density of states via the manipulation-induced incorporation of dopant atoms into the molecule[154]. Since

the magnitude of such non-equilibrium forces depends on the density of states weighted overlap population, density of states variations should alter current–induced forces.

Finally, the lateral force required to move single metal adatoms on three metal surfaces was quantified. Pb/Pb(111), Au/Au(111), Co/Au(111), Cu/Cu(111), and Co/Cu(111) served as experimental platforms to determine the temperature dependence of the lateral threshold forces. Variations between different adatom/substrate combinations were worked out and related to the character of the adatom–surface bonds. A simple model calculation considering thermal activation reproduces the experimental data. The absence of the impact of the density of states at the Fermi level on the lateral threshold forces of single atoms was unveiled by varying the phase of the substrate across the superconducting transition via temperature as well as magnetic field strength. Further experiments might provide more insight into single–atom manipulation forces. While the proposed model predicts a velocity–dependence of the lateral threshold force, all experiments were performed at identical velocity. In order to test the validity of the analytical approach and gain further insight into lateral forces at the atomic level, it will be interesting to determine the lateral threshold force as a function of tip velocity. Moreover, spin friction was previously explored with a scanning tunneling microscope[315]. Here, the impact of magnetic interactions on the lateral threshold force deserves further investigation. Finally, lower temperatures can provide further information concerning the microscope performance, in the following sense. Below a given temperature, thermal activation vanishes and the athermal contribution to the activation of single–atom manipulation dominates, leading to the development of a plateau of the lateral manipulation force[309]. Consequently, the magnitude of this force at $T \to 0\,\mathrm{K}$ yields an estimate of the residual instrumental noise relevant for the operation of the atomic force microscope.

Bibliography

[1] G. Binnig, H. Rohrer, C. Gerber, and E. Weibel, Phys. Rev. Lett. **49**, 57 (1982).

[2] G. Binnig, C. F. Quate, and C. Gerber, Phys. Rev. Lett. **56**, 930 (1986).

[3] J. Li, W.-D. Schneider, R. Berndt, and B. Delley, Phys. Rev. Lett. **80**, 2893 (1998).

[4] V. Madhavan, W. Chen, T. Jamneala, M. Crommie, and N. Wingreen, Science **280**, 567 (1998).

[5] B. Stipe, M. Rezaei, and W. Ho, Science **280**, 1732 (1998).

[6] S. Nadj-Perge, I. K. Drozdov, J. Li, H. Chen, S. Jeon, J. Seo, A. H. MacDonald, B. A. Bernevig, and A. Yazdani, Science **346**, 602 (2014).

[7] R. Pawlak, M. Kisiel, J. Klinovaja, T. Meier, S. Kawai, T. Glatzel, D. Loss, and E. Meyer, npj Quantum Inf. **2**, 16035 (2016).

[8] L. Gross, F. Mohn, N. Moll, P. Liljeroth, and G. Meyer, Science **325**, 1110 (2009).

[9] L. Gross, F. Mohn, P. Liljeroth, J. Repp, F. J. Giessibl, and G. Meyer, Science **324**, 1428 (2009).

[10] L. Gross, F. Mohn, N. Moll, B. Schuler, A. Criado, E. Guitián, D. Peña, A. Gourdon, and G. Meyer, Science **337**, 1326 (2012).

[11] M. Ternes, C. P. Lutz, C. F. Hirjibehedin, F. J. Giessibl, and A. J. Heinrich, Science **319**, 1066 (2008).

[12] R. M. Overney, H. Takano, M. Fujihira, W. Paulus, and H. Ringsdorf, Phys. Rev. Lett. **72**, 3546 (1994).

[13] S. Fujisawa, E. Kishi, Y. Sugawara, and S. Morita, Phys. Rev. B **51**, 7849 (1995).

[14] G. Gao, R. J. Cannara, R. W. Carpick, and J. A. Harrison, Langmuir **23**, 5394 (2007).

[15] A. J. Weymouth, D. Meuer, P. Mutombo, T. Wutscher, M. Ondracek, P. Jelinek, and F. J. Giessibl, Phys. Rev. Lett. **111**, 126103 (2013).

[16] J. Y. Park, D. Ogletree, P. Thiel, and M. Salmeron, Science **313**, 186 (2006).

[17] N. Hauptmann, F. Mohn, L. Gross, G. Meyer, T. Frederiksen, and R. Berndt, New J. Phys. **14**, 073032 (2012).

[18] N. Néel, private communication.

[19] A. Dayo, W. Alnasrallah, and J. Krim, Phys. Rev. Lett. **80**, 1690 (1998).

[20] M. Highland and J. Krim, Phys. Rev. Lett. **96**, 226107 (2006).

[21] M. Kisiel, E. Gnecco, U. Gysin, L. Marot, S. Rast, and E. Meyer, Nature Mater. **10**, 119 (2011).

[22] J. Bardeen, L. N. Cooper, and J. R. Schrieffer, Phys. Rev. **108**, 1175 (1957).

[23] R. Gross and A. Marx, *Festkörperphysik* (Walter de Gruyter GmbH & Co KG, 2014).

[24] J. Bardeen, Phys. Rev. Lett. **6**, 57 (1961).

[25] D. Bohm, *Quantum Theory* (Dover Publications, New York, 1951).

[26] D. Bonnell, *Scanning Probe Microscopy and Spectroscopy - Theory, Techniques, and Applications* (Wiley, New York, 2000).

[27] I. Giaever and K. Megerle, Phys. Rev. **122**, 1101 (1961).

[28] V. A. Ukraintsev, Phys. Rev. B **53**, 11176 (1996).

[29] R. M. Feenstra, J. A. Stroscio, and A. P. Fein, Surf. Sci. **181**, 295 (1987).

[30] B. Koslowski, C. Dietrich, A. Tschetschetkin, and P. Ziemann, Phys. Rev. B **75**, 035421 (2007).

[31] C. Wagner, R. Franke, and T. Fritz, Phys. Rev. B **75**, 235432 (2007).

[32] M. Ziegler, N. Néel, A. Sperl, J. Kröger, and R. Berndt, Phys. Rev. B **80**, 125402 (2009).

[33] J. Lambe and R. Jaklevic, Phys. Rev. **165**, 821 (1968).

[34] J. Klein, A. Léger, M. Belin, D. Défourneau, and M. J. L. Sangster, Phys. Rev. B **7**, 2336 (1973).
[35] P. K. Hansma, Phys. Rev. **30**, 145 (1977).
[36] A. F. Andreev, Sov. Phys. JETP **19**, 1228 (1964).
[37] G. E. Blonder, M. Tinkham, and T. M. Klapwijk, Phys. Rev. B **25**, 4515 (1982).
[38] F. J. Gießibl, Rev. Mod. Phys. **75**, 949 (2003).
[39] F. J. Gießibl, Phys. Rev. B **56**, 16010 (1997).
[40] F. J. Gießibl, Appl. Phys. Lett. **78**, 123 (2001).
[41] F. J. Gießibl, Appl. Phys. Lett. **78**, 123 (2001).
[42] J. E. Sader and S. P. Jarvis, Appl. Phys. Lett. **84**, 1801 (2004).
[43] J. E. Sader and Y. Sugimoto, Appl. Phys. Lett. **97**, 043502 (2010).
[44] F. Gießibl, Offenlegungsschrift German Patent Office DE **196**, 546 (1996).
[45] H. Le Sueur, *Cryogenic AFM-STM for Mesoscopic Phys.*, Ph.D. thesis, Université Pierre et Marie Curie-Paris VI (2007).
[46] F. J. Gießibl, "Sensor for noncontact profiling of a surface," (2013), US Patent 8,393,009.
[47] G. H. Simon, M. Heyde, and H.-P. Rust, Nanotechnology **18**, 255503 (2007).
[48] H. Hamaker, Phys. **4**, 1058 (1937).
[49] J. N. Israelachvili, *Intermolecular and Surface Forces* (Academic press, London, 1992).
[50] L. Olsson, N. Lin, V. Yakimov, and R. Erlandsson, J. Appl. Phys. **84**, 4060 (1998).
[51] F. J. Gießibl, S. Hembacher, H. Bielefeldt, and J. Mannhart, Science **289**, 422 (2000).
[52] F. H. Stillinger and T. A. Weber, Phys. Rev. B **31**, 5262 (1985).
[53] K. Pearson, Philos. Trans. R. Soc. London, Ser. A **187**, 253 (1896).
[54] R. Taylor, J. Diagn. Med. Sonogr. **6**, 35 (1990).
[55] J. B. Johnson, Phys. Rev. **32**, 97 (1928).
[56] H. Nyquist, Phys. Rev. **32**, 110 (1928).
[57] T. Albrecht, P. Grütter, D. Horne, and D. Rugar, J. Appl. Phys. **69**, 668 (1991).
[58] B. Voigtländer, *Scanning Probe Microscopy* (Springer, 2015).
[59] H. Suderow, P. Martinez-Samper, N. Luchier, J. Brison, S. Vieira, and P. Canfield, Phys. Rev. B **64**, 020503 (2001).
[60] H. Le Sueur and P. Joyez, Rev. Sci. Instrum. **77**, 123701 (2006).
[61] I.-P. Hong, *Quantum Size Effects in Ultrathin Metallic Islands*, Ph.D. thesis, École Polytechnique Fédérale de Lausanne (2009).
[62] J. Kim, *Low Temp. scanning tunneling microscope study of low-dimensional superconductivity on metallic nanostructures*, Ph.D. thesis, University of Texas (2010).
[63] B. B. Zhou, *A Scanning Tunneling Microscope at the Milli-Kelvin, High Magnetic Field Frontier*, Ph.D. thesis, Princeton University (2014).
[64] A. Roychowdhury, M. A. Gubrud, R. Dana, J. R. Anderson, C. J. Lobb, F. C. Wellstood, and M. Dreyer, Rev. Sci. Ins. **85**, 043706 (2014).
[65] J. Brand, *Andreev Reflections in Single C_{60} Junctions*, Master's thesis, Technische Universität Ilmenau (2015).
[66] S. Pan, E. Hudson, and J. Davis, Rev. Sci. Instrum. **70**, 1459 (1999).
[67] R. Dynes, V. Narayanamurti, and J. Garno, Phys. Rev. Lett. **41**, 1509 (1978).
[68] B. Mitrović and L. A. Rozema, J. Phys. Condens. Matter **20**, 015215 (2008).
[69] C. R. Ast, B. Jäck, J. Senkpiel, M. Eltschka, M. Etzkorn, J. Ankerhold, and K. Kern, Nat. Commun. **7**, 13009 (2016).
[70] Y. Qin and R. Reifenberger, Rev. Sci. Instrum. **78**, 063704 (2007).
[71] E. Scheer, N. Agraït, J. C. Cuevas, A. L. Yeyati, B. Ludoph, A. Martin-Rodero, G. R. Bollinger, J. M. van Ruitenbeek, and C. Urbina, Nature **394**, 154 (1998).
[72] Y.-J. Doh, J. A. van Dam, A. L. Roest, E. P. A. M. Bakkers, L. P. Kouwenhoven, and S. De Franceschi, Science **309**, 272 (2005).

[73] T. Dirks, T. L. Hughes, S. Lal, B. Uchoa, Y.-F. Chen, C. Chialvo, P. M. Goldbart, and N. Mason, Nat. Phys. **7**, 386 (2011).
[74] J. J. He, J. Wu, T.-P. Choy, X.-J. Liu, Y. Tanaka, and K. T. Law, Nature communications **5**, 3232 (2014).
[75] P. G. de Gennes, Rev. Mod. Phys. **36**, 225 (1964).
[76] B. Pannetier and H. Courtois, J. Low Temp. Phys. **118**, 599 (2000).
[77] R. Holm and W. Meissner, Z. Physik **74**, 715 (1932).
[78] C. J. Adkins and B. W. Kington, Philos. Mag. **13**, 971 (1966).
[79] C. J. Adkins and B. W. Kington, Phys. Rev. **177**, 777 (1969).
[80] R. D. Parks, *Superconductivity* (Taylor & Francis, 1969).
[81] T. T. Chen and L. Kiang, Chin. J. Phys. **12**, 53 (1974).
[82] W. Silvert, Solid State Commun. **14**, 635 (1974).
[83] J. Toplicar and D. Finnemore, Phys. Rev. B **16**, 2072 (1977).
[84] E. Wolf, J. Zasadzinski, J. Osmun, and G. Arnold, J. Low Temp. Phys. **40**, 19 (1980).
[85] P. C. van Son, H. van Kempen, and P. Wyder, Phys. Rev. Lett. **59**, 2226 (1987).
[86] S. Guéron, H. Pothier, N. Birge, D. Esteve, and M. Devoret, Phys. Rev. Lett. **77**, 3025 (1996).
[87] S. Tessmer, M. Tarlie, D. Van Harlingen, D. Maslov, and P. Goldbart, Phys. Rev. Lett. **77**, 924 (1996).
[88] A. Truscott, R. Dynes, and L. Schneemeyer, Phys. Rev. Lett. **83**, 1014 (1999).
[89] I. Kulik, Sov. Phys. JETP **30**, 944 (1969).
[90] J. Bar-Sagi and O. Entin-Wohlman, Solid State Commun. **22**, 29 (1977).
[91] G. B. Arnold and E. L. Wolf, Phys. Rev. B **25**, 1541 (1982).
[92] A. D'yachenko and I. Kochergin, J. Low Temp. Phys. **84**, 197 (1991).
[93] T. Klapwijk, J. Superc. **17**, 593 (2004).
[94] A. Y. Kasumov, R. Deblock, M. Kociak, B. Reulet, H. Bouchiat, I. I. Khodos, Y. B. Gorbatov, V. T. Volkov, C. Journet, and M. Burghard, Science **284**, 1508 (1999).
[95] A. Y. Kasumov, M. Kociak, S. Guéron, B. Reulet, V. T. Volkov, D. V. Klinov, and H. Bouchiat, Science **291**, 280 (2001).
[96] P. Jarillo-Herrero, J. A. van Dam, and L. P. Kouwenhoven, Nature **439**, 953 (2006).
[97] A. Kasumov, M. Kociak, M. Ferrier, R. Deblock, S. Guéron, B. Reulet, I. Khodos, O. Stéphan, and H. Bouchiat, Phys. Rev. B **68**, 214521 (2003).
[98] C. B. Winkelmann, N. Roch, W. Wernsdorfer, V. Bouchiat, and F. Balestro, Nature Phys. **5**, 876 (2009).
[99] K. J. Franke, G. Schulze, and J. I. Pascual, Science **332**, 940 (2011).
[100] G. E. Blonder and M. Tinkham, Phys. Rev. B **27**, 112 (1983).
[101] R. J. Soulen, J. M. Byers, M. S. Osofsky, B. Nadgorny, T. Ambrose, S. F. Cheng, P. R. Broussard, C. T. Tanaka, J. Nowak, J. S. Moodera, A. Barry, and J. M. D. Coey, Science **282**, 85 (1998).
[102] J. Y. T. Wei, N.-C. Yeh, D. F. Garrigus, and M. Strasik, Phys. Rev. Lett. **81**, 2542 (1998).
[103] G. J. Strijkers, Y. Ji, F. Y. Yang, C. L. Chien, and J. M. Byers, Phys. Rev. B **63**, 104510 (2001).
[104] N. Agraït, A. L. Yeyati, and J. M. van Ruitenbeek, Phys. Rep. **377**, 81 (2003).
[105] N. Auth, G. Jakob, T. Block, and C. Felser, Phys. Rev. B **68**, 024403 (2003).
[106] G. T. Woods, R. J. Soulen, I. Mazin, B. Nadgorny, M. S. Osofsky, J. Sanders, H. Srikanth, W. F. Egelhoff, and R. Datla, Phys. Rev. B **70**, 054416 (2004).
[107] R. S. Gonnelli, M. Tortello, D. Daghero, R. K. Kremer, Z. Bukowski, N. D. Zhigadlo, and J. Karpinski, Supercond. Sci. Technol. **25**, 065007 (2012).
[108] N. Agraït, J. G. Rodrigo, and S. Vieira, Phys. Rev. B **46**, 5814 (1992).
[109] N. Hauptmann, M. Becker, J. Kröger, and R. Berndt, Phys. Rev. B **79**, 144522 (2009).
[110] J. Brand, P. Ribeiro, N. Néel, S. Kirchner, and J. Kröger, Phys. Rev. Lett. **118**, 107001 (2017).
[111] L. Y. L. Shen, N. M. Senozan, and N. E. Phillips, Phys. Rev. Lett. **14**, 1025 (1965).

[112] D. K. Finnemore, T. F. Stromberg, and C. A. Swenson, Phys. Rev. **149**, 231 (1966).
[113] C. C. Koch, J. O. Scarbrough, and D. M. Kroeger, Phys. Rev. B **9**, 888 (1974).
[114] M. Peiniger and H. Piel, IEEE Trans. Nucl. Sci. **32**, 3610 (1985).
[115] H. W. Weber, E. Seidl, C. Laa, E. Schachinger, M. Prohammer, A. Junod, and D. Eckert, Phys. Rev. B **44**, 7585 (1991).
[116] M. D. Sherrill and H. H. Edwards, Phys. Rev. Lett. **6**, 460 (1961).
[117] P. Townsend and J. Sutton, Phys. Rev. **128**, 591 (1962).
[118] C. Chou, D. White, and H. L. Johnston, Phys. Rev. **109**, 788 (1958).
[119] R. French, Cryogenics **8**, 301 (1968).
[120] A. Das Gupta, J. Appl. Phys. **47**, 2146 (1976).
[121] R. Pantel, M. Bujor, and J. Bardolle, Surf. Sci. **62**, 589 (1977).
[122] C. Sürgers and H. v. Löhneysen, Appl. Phys. A **54**, 350 (1992).
[123] C. Sürgers, M. Schöck, and H. v. Löhneysen, Surf. Sci. **471**, 209 (2001).
[124] I. Arfaoui, J. Cousty, and H. Safa, Phys. Rev. B **65**, 115413 (2002).
[125] C. Dietrich, H.-G. Boyen, and B. Koslowski, J. App. Phys. **94**, 1478 (2003).
[126] I. Arfaoui, J. Cousty, and C. Guillot, Surf. Sci. **557**, 119 (2004).
[127] C. Wolf and U. Köhler, Thin Solid Films **500**, 347 (2006).
[128] A. S. Razinkin, E. V. Shalaeva, and M. V. Kuznetsov, Phys. Met. Metall. **106**, 56 (2008).
[129] A. Razinkin and M. Kuznetsov, Phys. Met. Metall. **110**, 531 (2010).
[130] T. Tomanic, *Untersuchung des elektronischen Oberflächenzustands von Ag-Inseln auf supraleitendem Niob(110)*, Ph.D. thesis (2012).
[131] W. DeSorbo, Phys. Rev. **132**, 107 (1963).
[132] G. Schull, T. Frederiksen, M. Brandbyge, and R. Berndt, Phys. Rev. Lett. **103**, 206803 (2009).
[133] G. Schull, T. Frederiksen, A. Arnau, D. Sanchez-Portal, and R. Berndt, Nature Nanotechnol. **6**, 23 (2011).
[134] I. D. Hands, J. L. Dunn, and C. A. Bates, Phys. Rev. B **81**, 205440 (2010).
[135] M. Grobis, X. Lu, and M. Crommie, Phys. Rev. B **66**, 161408 (2002).
[136] N. A. Pradhan, N. Liu, and W. Ho, J. Phys. Chem. B **109**, 8513 (2005).
[137] G. Schull and R. Berndt, Phys. Rev. Lett. **99**, 226105 (2007).
[138] N. Néel, J. Kröger, L. Limot, and R. Berndt, Nano Lett. **8**, 1291 (2008).
[139] N. Néel, L. Limot, J. Kröger, and R. Berndt, Phys. Rev. B **77**, 125431 (2008).
[140] G. Géranton, C. Seiler, A. Bagrets, L. Venkataraman, and F. Evers, J. Chem. Phys. **139**, 234701 (2013).
[141] K. J. Franke, G. Schulze, N. Henningsen, I. Fernández-Torrente, J. I. Pascual, S. Zarwell, K. Rück-Braun, M. Cobian, and N. Lorente, Phys. Rev. Lett. **100**, 036807 (2008).
[142] I. F. Torrente, K. J. Franke, and J. I. Pascual, J. Phys. Condens. Matter **20**, 184001 (2008).
[143] K. J. Franke and J. I. Pascual, J. Phys. Condens. Matter **24**, 394002 (2012).
[144] B. Stadtmüller, *Study of intermolecular interactions in hetero-organic thin films*, Vol. 61 (Forschungszentrum Jülich, 2013).
[145] R. Hesper, L. Tjeng, and G. Sawatzky, Europhys. Lett. **40**, 177 (1997).
[146] D. L. Lichtenberger, K. W. Nebesny, C. D. Ray, D. R. Huffman, and L. D. Lamb, Chem. Phys. Lett. **176**, 203 (1991).
[147] J. De Vries, H. Steger, B. Kamke, C. Menzel, B. Weisser, W. Kamke, and I. Hertel, Chem. Phys. Lett. **188**, 159 (1992).
[148] I. Hertel, H. Steger, J. De Vries, B. Weisser, C. Menzel, B. Kamke, and W. Kamke, Phys. Rev. Lett. **68**, 784 (1992).
[149] R. Yoo, B. Ruscic, and J. Berkowitz, J. Chem. Phys. **96**, 911 (1992).
[150] S. Yang, C. L. Pettiette, J. Conceicao, O. Cheshnovsky, and R. Smalley, Chem. Phys. Lett. **139**, 233 (1987).

[151] T. Ohno, Y. Chen, S. Harvey, G. Kroll, J. Weaver, R. Haufler, and R. Smalley, Phys. Rev. B **44**, 13747 (1991).
[152] X. Lu, M. Grobis, K. H. Khoo, S. G. Louie, and M. F. Crommie, Phys. Rev. Lett. **90**, 096802 (2003).
[153] C. Silien, N. Pradhan, W. Ho, and P. Thiry, Phys. Rev. B **69**, 115434 (2004).
[154] R. Yamachika, M. Grobis, A. Wachowiak, and M. F. Crommie, Science **304**, 281 (2004).
[155] X. Lu, M. Grobis, K. Khoo, S. Louie, and M. Crommie, Phys. Rev. B **70**, 115418 (2004).
[156] F. Schiller, M. Ruiz-Osés, J. E. Ortega, P. Segovia, J. Martínez-Blanco, B. P. Doyle, V. Pérez-Dieste, J. Lobo, N. Néel, R. Berndt, and J. Kröger, J. Chem. Phys. **125**, 144719 (2006).
[157] G. Schulze, K. J. Franke, A. Gagliardi, G. Romano, C. S. Lin, A. L. Rosa, T. A. Niehaus, T. Frauenheim, A. Di Carlo, A. Pecchia, and J. I. Pascual, Phys. Rev. Lett. **100**, 136801 (2008).
[158] G. Schulze, K. J. Franke, and J. I. Pascual, New J. Phys. **10**, 065005 (2008).
[159] T. Frederiksen, K. J. Franke, A. Arnau, G. Schulze, J. I. Pascual, and N. Lorente, Phys. Rev. B **78**, 233401 (2008).
[160] J. A. Larsson, S. D. Elliott, J. C. Greer, J. Repp, G. Meyer, and R. Allenspach, Phys. Rev. B **77**, 115434 (2008).
[161] L. Limot, J. Kröger, R. Berndt, A. Garcia-Lekue, and W. Hofer, Phys. Rev. Lett. **94**, 126102 (2005).
[162] N. Néel, J. Kröger, L. Limot, and R. Berndt, Nanotechnology **18**, 044027 (2007).
[163] J. Kröger, H. Jensen, and R. Berndt, New J. Phys. **9**, 153 (2007).
[164] J. Kröger, N. Néel, and L. Limot, J. Phys.: Condens. Matter **20**, 223001 (2008).
[165] J. Kröger, N. Néel, A. Sperl, Y. F. Wang, and R. Berndt, New J. Phys. **11**, 125006 (2009).
[166] V. Lukic, *Conductance of superconductor-normal metal contact junction beyond quasiclassical approximation*, Ph.D. thesis, University of Illinois at Urbana-Champaign (2005).
[167] D. Gall, J. Appl. Phys. **119**, 085101 (2016).
[168] N. W. Ashcroft and N. D. Mermin, *Solid state Phys.* (Holt, Rinehart and Winston, New York, 1976).
[169] R. Hiraoka, R. Arafune, N. Tsukahara, M. Kawai, and N. Takagi, Phys. Rev. B **90**, 241405 (2014).
[170] R. Landauer, J. Phys.: Condens. Matter **1**, 8099 (1989).
[171] S. Datta, *Electronic transport in mesoscopic systems* (Cambridge university press, 1997).
[172] Y. Imry and R. Landauer, Rev. Mod. Phys. **71**, S306 (1999).
[173] J. Brand, S. Gozdzik, N. Néel, J. L. Lado, J. Fernández-Rossier, and J. Kröger, Phys. Rev. B **97**, 195429 (2018).
[174] G. Rubio, N. Agrait, and S. Vieira, Phys. Rev. Lett. **76**, 2302 (1996).
[175] G. Cross, A. Schirmeisen, A. Stalder, P. Grütter, M. Tschudy, and U. Dürig, Phys. Rev. Lett. **80**, 4685 (1998).
[176] M. Lantz, S. O'Shea, and M. Welland, Surf. Sci. **437**, 99 (1999).
[177] A. Schirmeisen, G. Cross, A. Stalder, P. Grütter, and U. Dürig, New J. Phys. **2**, 29 (2000).
[178] B. Gotsmann and H. Fuchs, Phys. Rev. Lett. **86**, 2597 (2001).
[179] Y. Sun, H. Mortensen, S. Schär, A.-S. Lucier, Y. Miyahara, P. Grütter, and W. Hofer, Phys. Rev. B **71**, 193407 (2005).
[180] N. Néel, J. Kröger, L. Limot, K. Palotas, W. A. Hofer, and R. Berndt, Phys. Rev. Lett. **98**, 016801 (2007).
[181] N. Néel, J. Kröger, and R. Berndt, Phys. Rev. Lett. **102**, 086805 (2009).
[182] D. Sawada, Y. Sugimoto, K.-i. Morita, M. Abe, and S. Morita, Appl. Phys. Lett. **94**, 173117 (2009).
[183] N. Néel, J. Kröger, and R. Berndt, Nano Lett. **11**, 3593 (2011).
[184] M. Ternes, C. González, C. P. Lutz, P. Hapala, F. J. Giessibl, P. Jelínek, and A. J. Heinrich, Phys. Rev. Lett. **106**, 016802 (2011).
[185] N. Hauptmann and R. Berndt, Phys. Status Solidi B (b) **250**, 2403 (2013).
[186] N. L. Schneider, N. Néel, N. P. Andersen, J. T. Lü, M. Brandbyge, J. Kröger, and R. Berndt, J. Phys.: Condens. Matter **27**, 015001 (2015).

[187] W. W. Pai, H. Jeng, C.-M. Cheng, C.-H. Lin, X. Xiao, A. Zhao, X. Zhang, G. Xu, X. Shi, M. Van Hove, *et al.*, Phys. Rev. Lett. **104**, 036103 (2010).
[188] N. Hauptmann, C. González, F. Mohn, L. Gross, G. Meyer, and R. Berndt, Nanotechnology **26**, 445703 (2015).
[189] A. J. Lakin, C. Chiutu, A. M. Sweetman, P. Moriarty, and J. L. Dunn, Phys. Rev. B **88**, 035447 (2013).
[190] A. Sweetman, M. A. Rashid, S. P. Jarvis, J. L. Dunn, P. Rahe, and P. Moriarty, Nature Communications **7**, 10621 (2016).
[191] J. Garnaes, F. Kragh, K. Mørch, and A. Thölén, J. Vac. Sci. Technol., A **8**, 441 (1990).
[192] M. J. Vasile, D. Grigg, J. E. Griffith, E. Fitzgerald, and P. E. Russell, J. Vac. Sci. Technol. B **9**, 3569 (1991).
[193] M. J. Vasile, D. A. Grigg, J. E. Griffith, E. A. Fitzgerald, and P. E. Russell, Rev. Sci. Instrum. **62**, 2167 (1991).
[194] I. H. Musselman and P. E. Russell, J. Vac. Sci. Technol., A **8**, 3558 (1990).
[195] A. Sørensen, U. Hvid, M. Mortensen, and K. Mørch, Rev. Sci. Instr. **70**, 3059 (1999).
[196] M. Araidai and K. Watanabe, e-J. Surf. Sci. and Nanotechnology **5**, 106 (2007).
[197] T. Soga, *Nanostructured Mater. for Solar Energy Conversion* (Elsevier Science, 2006).
[198] J. L. Hutter and J. Bechhoefer, Rev. Sci. Instrum. **64**, 1868 (1993).
[199] L. Bergström, Adv. Colloid Interface Sci. **70**, 125 (1997).
[200] R. H. French, J. Am. Ceram. Soc. **83**, 2117 (2000).
[201] J. Jackson, *Classical Electrodynamics* (John Wiley & Sons, New York, 1962).
[202] L. Bergmann, W. Raith, and C. Schaefer, *Elektromagnetismus*, Vol. 2 (Walter de Gruyter, 2006).
[203] R. Antoine, P. Dugourd, D. Rayane, E. Benichou, M. Broyer, F. Chandezon, and C. Guet, J. Chem. Phys. **110**, 9771 (1999).
[204] A. Ballard, K. Bonin, and J. Louderback, J. Chem. Phys. **113**, 5732 (2000).
[205] C. Rackson, A. Watt, and W. Kim, Phys. Lett. A **379** (2015).
[206] S. E. Pollack, S. Schlamminger, and J. H. Gundlach, Phys. Rev. Lett. **101**, 071101 (2008).
[207] W. J. Kim, A. O. Sushkov, D. A. R. Dalvit, and S. K. Lamoreaux, Phys. Rev. Lett. **103**, 060401 (2009).
[208] S. de Man, K. Heeck, and D. Iannuzzi, Phys. Rev. A **79**, 024102 (2009).
[209] G. Torricelli, I. Pirozhenko, S. Thornton, A. Lambrecht, and C. Binns, Europhys. Lett. **93**, 51001 (2011).
[210] J. Laurent, H. Sellier, A. Mosset, S. Huant, and J. Chevrier, Phys. Rev. B **85**, 035426 (2012).
[211] L. Gross, B. Schuler, F. Mohn, N. Moll, N. Pavliček, W. Steurer, I. Scivetti, K. Kotsis, M. Persson, and G. Meyer, Phys. Rev. B **90**, 155455 (2014).
[212] A. Yurtsever, D. Fernández-Torre, J. Onoda, M. Abe, S. Morita, Y. Sugimoto, and R. Pérez, Nanoscale **9**, 5812 (2017).
[213] L. Nony, A. S. Foster, F. Bocquet, and C. Loppacher, Phys. Rev. Lett. **103**, 036802 (2009).
[214] S. Burke, J. LeDue, Y. Miyahara, J. Topple, S. Fostner, and P. Grütter, Nanotechnology **20**, 264012 (2009).
[215] A. Yurtsever, Y. Sugimoto, M. Fukumoto, M. Abe, and S. Morita, Appl. Phys. Lett. **101**, 083119 (2012).
[216] E. Inami and Y. Sugimoto, Phys. Rev. Lett. **114**, 246102 (2015).
[217] S. Sadewasser, P. Jelinek, C.-K. Fang, O. Custance, Y. Yamada, Y. Sugimoto, M. Abe, and S. Morita, Phys. Rev. Lett. **103**, 266103 (2009).
[218] E. Inami and Y. Sugimoto, Jpn. J. Appl. Phys. **55**, 08NB05 (2016).
[219] A. J. Weymouth, T. Wutscher, J. Welker, T. Hofmann, and F. J. Giessibl, Phys. Rev. Lett. **106**, 226801 (2011).
[220] A. J. Weymouth and F. J. Giessibl, Appl. Phys. Lett. **101**, 213105 (2012).

[221] S. Ulstrup, T. Frederiksen, and M. Brandbyge, Phys. Rev. B **86**, 245417 (2012).
[222] R. Mulliken, J. Chem. Phys. **23**, 1841 (1955).
[223] T. Hughbanks and R. Hoffmann, J. Am. Chem. Soc. **105**, 3528 (1983).
[224] R. Hoffmann, Rev. Mod. Phys. **60**, 601 (1988).
[225] M. Brandbyge, K. Stokbro, J. Taylor, J.-L. Mozos, and P. Ordejón, Phys. Rev. B **67**, 193104 (2003).
[226] J. Brand, S. Leitherer, N. P. Rübner, N. Néel, M. Brandbyge, and J. Kröger, "Exploring the analogue to electron wind forces in single-molecule junctions," (2019), *in preparation*.
[227] D. M. Eigler and E. K. Schweizer, Nature **344**, 524 (1990).
[228] J. A. Stroscio and D. Eigler, Science **254**, 1319 (1991).
[229] P. Zeppenfeld, C. Lutz, and D. Eigler, Ultramicroscopy **42**, 128 (1992).
[230] M. F. Crommie, C. P. Lutz, and D. M. Eigler, Science **262**, 218 (1993).
[231] G. Meyer and K.-H. Rieder, Surf. Sci. **377**, 1087 (1997).
[232] L. Bartels, G. Meyer, and K.-H. Rieder, Phys. Rev. Lett. **79**, 697 (1997).
[233] J. A. Stroscio and R. J. Celotta, Science **306**, 242 (2004).
[234] Y. Sugimoto, M. Abe, S. Hirayama, N. Oyabu, Ó. Custance, and S. Morita, Nat. Mater. **4**, 156 (2005).
[235] A. A. Khajetoorians, J. Wiebe, B. Chilian, and R. Wiesendanger, Science **332**, 1062 (2011).
[236] S. Loth, S. Baumann, C. P. Lutz, D. Eigler, and A. J. Heinrich, Science **335**, 196 (2012).
[237] K. K. Gomes, W. Mar, W. Ko, F. Guinea, and H. C. Manoharan, Nature **483**, 306 (2012).
[238] A. A. Khajetoorians, B. Baxevanis, C. Hübner, T. Schlenk, S. Krause, T. O. Wehling, S. Lounis, A. Lichtenstein, D. Pfannkuche, J. Wiebe, *et al.*, Science **339**, 55 (2013).
[239] S. Jarvis, H. Yamada, K. Kobayashi, A. Toda, and H. Tokumoto, Appl. Surf. Sci. **157**, 314 (2000).
[240] O. Pfeiffer, R. Bennewitz, A. Baratoff, E. Meyer, and P. Grütter, Phys. Rev. B **65**, 161403 (2002).
[241] F. J. Giessibl, M. Herz, and J. Mannhart, Proc. Natl. Acad. Sci. **99**, 12006 (2002).
[242] A. J. Weymouth, T. Hofmann, and F. J. Giessibl, Science , 1249502 (2014).
[243] H.-Q. Mao, N. Li, X. Chen, and Q.-K. Xue, J. Phys.: Condens. Matter **24**, 084004 (2012).
[244] G. Langewisch, J. Falter, H. Fuchs, and A. Schirmeisen, Phys. Rev. Lett. **110**, 036101 (2013).
[245] M. Emmrich, M. Schneiderbauer, F. Huber, A. J. Weymouth, N. Okabayashi, and F. J. Giessibl, Phys. Rev. Lett. **114**, 146101 (2015).
[246] S. P. Jarvis, S. Taylor, J. D. Baran, N. R. Champness, J. Larsson, and P. Moriarty, Nat. Commun. **6**, 8338 (2015).
[247] J. Berwanger, F. Huber, and F. J. Giessibl, arXiv preprint arXiv:1804.04382 (2018).
[248] B. Persson, *Sliding Friction, Phys. Properties and Applications* (2000).
[249] B. Mason, S. Winder, and J. Krim, Tribol. Lett. **10**, 59 (2001).
[250] A. Socoliuc, E. Gnecco, S. Maier, O. Pfeiffer, A. Baratoff, R. Bennewitz, and E. Meyer, Science **313**, 207 (2006).
[251] R. Meservey, P. Tedrow, and P. Fulde, Phys. Rev. Lett. **25**, 1270 (1970).
[252] G. Karapetrov, M. Iavarone, W. Kwok, G. Crabtree, and D. Hinks, Phys. Rev. Lett. **86**, 4374 (2001).
[253] A. Anthore, H. Pothier, and D. Esteve, Phys. Rev. Lett. **90**, 127001 (2003).
[254] N. Levy, T. Zhang, J. Ha, F. Sharifi, A. A. Talin, Y. Kuk, and J. A. Stroscio, Phys. Rev. Lett. **110**, 117001 (2013).
[255] J. Kondo, Prog. Theor. Phys. **32**, 37 (1964).
[256] A. A. Abrikosov, Phys. Phys. Fiz. **2**, 5 (1965).
[257] A. A. Abrikosov, Phys. Phys. Fiz. **2**, 61 (1965).
[258] D. Goldhaber-Gordon, H. Shtrikman, D. Mahalu, D. Abusch-Magder, U. Meirav, and M. Kastner, Nature **391**, 156 (1998).
[259] S. M. Cronenwett, T. H. Oosterkamp, and L. P. Kouwenhoven, Science **281**, 540 (1998).
[260] K. Nagaoka, T. Jamneala, M. Grobis, and M. Crommie, Phys. Rev. Lett. **88**, 077205 (2002).
[261] A. F. Otte, M. Ternes, K. Von Bergmann, S. Loth, H. Brune, C. P. Lutz, C. F. Hirjibehedin, and

A. J. Heinrich, Nat. Phys. **4**, 847 (2008).
[262] R. Renner, J. Rutledge, and P. Taborek, Phys. Rev. Lett. **83**, 1261 (1999).
[263] J. Krim, Phys. Rev. Lett. **83**, 1262 (1999).
[264] R. Renner, P. Taborek, and J. Rutledge, Phys. Rev. B **63**, 233405 (2001).
[265] D. Tsivlin, V. Stepanyuk, W. Hergert, and J. Kirschner, Phys. Rev. B **68**, 205411 (2003).
[266] V. Stepanyuk, A. Baranov, D. Tsivlin, W. Hergert, P. Bruno, N. Knorr, M. Schneider, and K. Kern, Phys. Rev. B **68**, 205410 (2003).
[267] N. Takeuchi, C. T. Chan, and K. Ho, Phys. Rev. B **43**, 13899 (1991).
[268] J. Lian, Z. Cheng, Y. Jiang, Y. Zhang, L. Liu, W. Ji, W. Xiao, S. Du, W. Hofer, and H.-J. Gao, Phys. Rev. B **81**, 195411 (2010).
[269] H. Kim and Y. Hasegawa, Phys. Rev. Lett. **114**, 206801 (2015).
[270] V. Madhavan, W. Chen, T. Jamneala, M. Crommie, and N. S. Wingreen, Phys. Rev. B **64**, 165412 (2001).
[271] N. Knorr, *Electronic Interactions at Noble Metal Surfaces Studied by Scanning Tunneling Microscopy*, Ph.D. thesis, PhD thesis, EPFL, Lausanne (2002).
[272] H. Manoharan, C. Lutz, and D. Eigler, Nature **403**, 512 (2000).
[273] N. Knorr, H. Brune, M. Epple, A. Hirstein, M. Schneider, and K. Kern, Phys. Rev. B **65**, 115420 (2002).
[274] N. Néel, J. Kröger, R. Berndt, T. Wehling, A. Lichtenstein, and M. Katsnelson, Phys. Rev. Lett. **101**, 266803 (2008).
[275] J. Barth, H. Brune, G. Ertl, and R. Behm, Phys. Rev. B **42**, 9307 (1990).
[276] S. Narasimhan and D. Vanderbilt, Phys. Rev. Lett. **69**, 1564 (1992).
[277] J. Repp, F. Moresco, G. Meyer, K.-H. Rieder, P. Hyldgaard, and M. Persson, Phys. Rev. Lett. **85**, 2981 (2000).
[278] N. Knorr, H. Brune, M. Epple, A. Hirstein, M. Schneider, and K. Kern, Phys. Rev. B **65**, 115420 (2002).
[279] A. Bogicevic, S. Ovesson, P. Hyldgaard, B. Lundqvist, H. Brune, and D. Jennison, Phys. Rev. Lett. **85**, 1910 (2000).
[280] D. A. Papaconstantopoulos *et al.*, *Handbook of the Band Structure of Elemental Solids: From Z* (Springer, 2016).
[281] B. Hammer and J. Norskov, Nature **376**, 238 (1995).
[282] C.-G. Zhan, L. Fan, F. Liu, and Z.-M. Hu, Int. J. Quantum Chem. **32**, 13 (1987).
[283] M. Calvo, C. Sabater, W. Dednam, E. B. Lombardi, M. J. Caturla, and C. Untiedt, Phys. Rev. Lett. **120**, 076802 (2018).
[284] P. Wahl, L. Diekhöner, M. Schneider, L. Vitali, G. Wittich, and K. Kern, Phys. Rev. Lett. **93**, 176603 (2004).
[285] P. Yang, D. Li, V. Repain, C. Chacon, Y. Girard, S. Rousset, A. Smogunov, Y. J. Dappe, C. Barreteau, and J. Lagoute, J. Phys. Chem. C **119**, 6873 (2015).
[286] E. Zupanič, H. J. van Midden, I. Muševič, A. Prodan, *et al.*, Phys. Rev. Lett. **104**, 196102 (2010).
[287] S. Glasstone, K. Laidler, and H. Eyring, *The Theory of Rate Processes* (McGraw-Hill, New York, 1941).
[288] H. Brune, Surf. Sci. Rep. **31**, 125 (1998).
[289] J. V. Barth, Surf. Sci. Rep. **40**, 75 (2000).
[290] L. Prandtl, Z. Angew. Math. Mech. **8**, 85 (1928).
[291] G. Tomlinson, Philos. Mag. **7**, 905 (1929).
[292] E. Gnecco, R. Bennewitz, T. Gyalog, C. Loppacher, M. Bammerlin, E. Meyer, and H.-J. Güntherodt, Phys. Rev. Lett. **84**, 1172 (2000).
[293] Y. Sang, M. Dubé, and M. Grant, Phys. Rev. Lett. **87**, 174301 (2001).
[294] E. Riedo, E. Gnecco, R. Bennewitz, E. Meyer, and H. Brune, Phys. Rev. Lett. **91**, 084502 (2003).

[295] M. Igarashi, A. Natori, and J. Nakamura, Phys. Rev. B **78**, 165427 (2008).
[296] P. Steiner, R. Roth, E. Gnecco, A. Baratoff, S. Maier, T. Glatzel, and E. Meyer, Phys. Rev. B **79**, 045414 (2009).
[297] L. Jansen, H. Hölscher, H. Fuchs, and A. Schirmeisen, Phys. Rev. Lett. **104**, 256101 (2010).
[298] S. Maier, Y. Sang, T. Filleter, M. Grant, R. Bennewitz, E. Gnecco, and E. Meyer, Phys. Rev. B **72**, 245418 (2005).
[299] S. Y. Krylov and J. W. Frenken, New J. Phys. **9**, 398 (2007).
[300] H. Hölscher, A. Schirmeisen, and U. D. Schwarz, Phil. Trans. R. Soc. A **366**, 1383 (2008).
[301] O. J. Furlong, S. J. Manzi, V. D. Pereyra, V. Bustos, and W. T. Tysoe, Phys. Rev. B **80**, 153408 (2009).
[302] O. M. Braun and Y. S. Kivshar, *The Frenkel-Kontorova Model: Concepts, Methods, and Applications* (Springer Science & Business Media, 2013).
[303] E. Jagla, J. Stat. Mech. **2018**, 013401 (2018).
[304] K. Tian, D. L. Goldsby, and R. W. Carpick, Phys. Rev. Lett. **120**, 186101 (2018).
[305] Y. Dong, A. Vadakkepatt, and A. Martini, Tribol. Lett. **44**, 367 (2011).
[306] M.-C. Marinica, C. Barreteau, M.-C. Desjonquères, and D. Spanjaard, Phys. Rev. B **70**, 075415 (2004).
[307] N. Negulyaev, V. Stepanyuk, P. Bruno, L. Diekhöner, P. Wahl, and K. Kern, Phys. Rev. B **77**, 125437 (2008).
[308] J. Barth, H. Brune, B. Fischer, J. Weckesser, and K. Kern, Phys. Rev. Lett. **84**, 1732 (2000).
[309] Y. Dong, H. Gao, and A. Martini, Europhys. Lett. **98**, 16002 (2012).
[310] C. P. Poole, H. A. Farach, R. J. Creswick, and R. Prozorov, *Superconductivity* (Elsevier Science, 2014).
[311] L. Bruch, Phys. Rev. B **61**, 16201 (2000).
[312] J. Sokoloff, M. Tomassone, and A. Widom, Phys. Rev. Lett. **84**, 515 (2000).
[313] F. Pielmeier, D. Meuer, D. Schmid, C. Strunk, and F. J. Giessibl, Beilstein J. Nanotechnol. **5**, 407 (2014).
[314] A. Peronio and F. J. Giessibl, Phys. Rev. B **94**, 094503 (2016).
[315] B. Wolter, Y. Yoshida, A. Kubetzka, S.-W. Hla, K. von Bergmann, and R. Wiesendanger, Phys. Rev. Lett. **109**, 116102 (2012).
[316] D. Serrate, M. Moro-Lagares, M. Piantek, J. I. Pascual, and M. R. Ibarra, J. Phys. Chem. C **118**, 5827 (2014).
[317] L. Lauhon and W. Ho, Phys. Rev. Lett. **85**, 4566 (2000).
[318] T. Mitsui, M. Rose, E. Fomin, D. Ogletree, and M. Salmeron, Surf. Sci. **540**, 5 (2003).
[319] R. Smit, Y. Noat, C. Untiedt, N. Lang, M. v. van Hemert, and J. Van Ruitenbeek, Nature **419**, 906 (2002).
[320] Q. Dubout, F. Donati, C. Wäckerlin, F. Calleja, M. Etzkorn, A. Lehnert, L. Claude, P. Gambardella, and H. Brune, Phys. Rev. Lett. **114**, 106807 (2015).
[321] F. Donati, Q. Dubout, G. Autès, F. Patthey, F. Calleja, P. Gambardella, O. Yazyev, and H. Brune, Phys. Rev. Lett. **111**, 236801 (2013).
[322] B. Kiraly, A. N. Rudenko, W. M. van Weerdenburg, D. Wegner, M. I. Katsnelson, and A. A. Khajetoorians, arXiv preprint arXiv:1807.01668 (2018).
[323] B. N. Persson, O. Albohr, F. Mancosu, V. Peveri, V. Samoilov, and I. M. Sivebæk, Wear **254**, 835 (2003).

List of Figures

List of Tables

List of Peer-Reviewed Publications

- J. Brand, P. Ribeiro, N. Néel, S. Kirchner, and J. Kröger
  Impact of Atomic-Scale Contact Geometry on Andreev Reflection
  Phys. Rev. Lett. **118**, 107001 (2017)

- J. Brand, S. Gozdzik, N. Néel, J. L. Lado, J. Fernández-Rossier, and J. Kröger
  Electron and Cooper-pair Transport Across a Single Magnetic Molecule Explored with a Scanning Tunneling Microscope
  Phys. Rev. B. **97**, 195429 (2018)

- J. Brand, N. Néel, and J. Kröger
  Moving Atoms on Surfaces: Impact of External Parameters on Required Lateral Force
  Phys. Rev. B **98**, 235420 (2018)

Frequently used Abbreviations and Symbols

AR	Andreev reflection	AFM	Atomic force microscope/microscopy
BCS	Bardeen-Cooper-Schrieffer	BTK	Blonder-Tinkham-Klapwijk
DOS	Density of states	HOMO	Highest occupied molecular orbital
LUMO	Lowest unoccupied molecular orbital	LUMO+1	Next-to-lowest unoccupied molecular orbital
QP	Quasi particle	SC	Superconductor / superconducting
SPE	Superconducting proximity effect	STM	Scanning tunneling microscope/microscopy
STS	Scanning tunneling spectroscopy	UHV	Ultra-high vacuum

$\mathcal{N}$	Normal conductor	$\mathcal{S}$	Superconductor

A	AFM oscillation amplitude	e	Elementary charge
E	Energy	E_F	Fermi energy
f	Frequency	f_0	Resonance frequency
Δf	Frequency shift $f_0 - f_0(F_\mathrm{ts} = 0)$	F	Force
F_ts	Force between tip and sample	F_x	Lateral force
F_z	Vertical force	G	Conductance, I/V
G_0	Quantum of conductance, $2\mathrm{e}^2/\mathrm{h}$	G^∂	Differential conductance, $\mathrm{d}I/\mathrm{d}V$
$\hbar$	Reduced Planck constant, $\mathrm{h}/2\pi$	I	Current
k	Spring constant, stiffness	$\mathrm{k_B}$	Boltzmann constant
m	Mass	Q	Quality factor
T	Temperature	V	Voltage
V_m	Modulation voltage amplitude	V_cp	Contact potential difference
z	Tip piezo displacement	Z	BTK barrier height, $Z \in [0, \infty]$

β	Boltzmann factor, $\beta = 1/k_B T$	∂_x^n	n^{th} derivative, $\partial_x^n \equiv d^n/dx^n$
Δ	Half width of the SC energy gap / order parameter	Γ	Coupling strength / hybridization parameter
γ	Coupling ratio between two channels $\Gamma^{\alpha,\beta}$, $\gamma = \Gamma^{\beta}/\Gamma^{\alpha}$	μ	Chemical potential
∇	Nabla operator	ω	Angular frequency
Φ	Work function	ϱ	Density of states
τ	BTK transmission, $\tau = (1 + Z^2)^{-1}$, $\tau \in [0, 1]$		
$\mathcal{A}$	Probability of Andreev reflection	$\mathcal{B}$	Probability of normal reflection
$\mathfrak{f}$	Fermi-Dirac distribution function	$\mathcal{H}$	Hamiltonian

A Appendix

A.1. Optimization of an Atomic Force Microscope

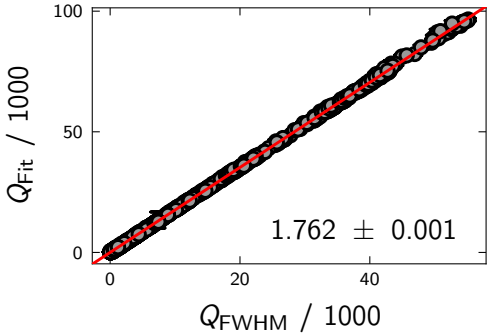

Figure A.1. $\hat{Q} = Q_{Fit}$ obtained from fits of experimental $A(f)$ data to eq. (2.43) as a function of Q_{FWHM} calculated according to eq. (2.42) (black). The red line denotes a linear fit to the data yielding a slope of 1.762 ± 0.001.

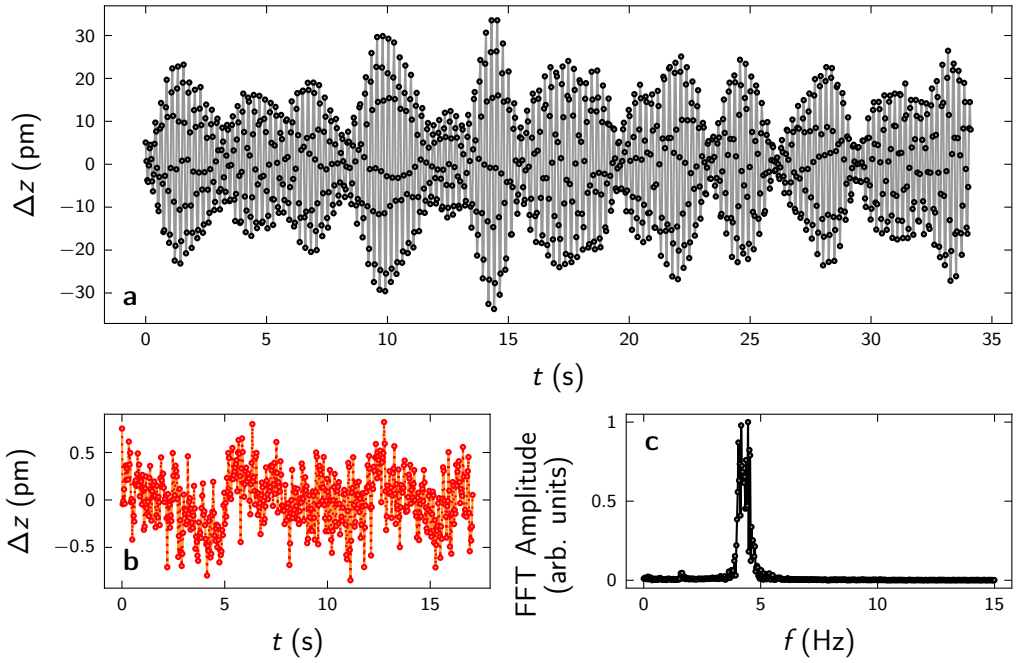

Figure A.2. **a,b**, z variation in constant current mode obtained at 100 mV, 55 pA (**a**) and 52 mV, 110 pA (**b**). The data are representative for an open (**a**) and closed (**b**) cryostat input. **c**, FFT amplitude of the data presented in **a**. Two maxima are visible at ∼4.2 Hz and ∼4.5 Hz.

A.2. Superconductivity of Single C_{60} Molecules on Nb(110)

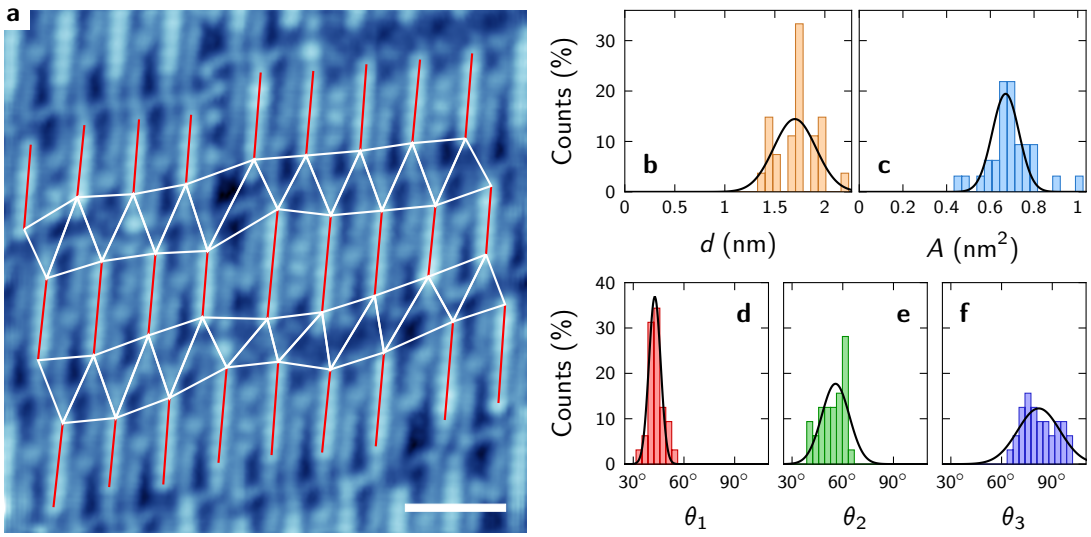

Figure A.3. Quantitative analysis of the heterogeneity of the NbO surface and consequently the C_{60} adsorption sites. **a**, Constant-current topography (0.1 V, 0.5 μA, scale bar 2 nm) of Nb atomic chains (highlighted by red lines) on a NbO(111) monolayer on Nb(110). The triangles formed by the chains are indicated in white. **b-d**, Distribution of chain lengths (**b**), triangle areas (**c**), and angles enclosed by the sides of triangles (**d-f**). θ_1, θ_2, and θ_3 denote the smallest, middle, and largest angle of each triangle, respectively. Solid lines are Gaussian fits to the data with peak positions $d_0 = 1.7 \pm 0.1$ nm, $A_0 = 0.67 \pm 0.01$ nm^2, $\theta_1^{(0)} = 42.7 \pm 0.4°$, $\theta_2^{(0)} = 55.7 \pm 2.4°$, and $\theta_3^{(0)} = 82.0 \pm 2.4°$ as well as square root of the variance (variance σ^2) $\sigma_d = 0.2 \pm 0.1$ nm, $\sigma_A = 0.06 \pm 0.01$ nm^2, $\sigma_{\theta_1} = 3.5 \pm 0.4°$, $\sigma_{\theta_2} = 8.1 \pm 2.4°$, and $\sigma_{\theta_3} = 12.5 \pm 2.7°$ respectively.

Sample	Type	Orientation	V_{HOMO} (V)	V_{LUMO} (V)	V_{LUMO+1} (V)	Υ (V)	Ref.
Ag(100)	layer	5–6	-1.8	0.15, 0.55	1.75	1.95	135
	layer	6–6	-1.7	0.11, 0.49	1.62	1.8	135
	isolated	6–6	-1.7	0.02, 0.41	1.62	1.7	135,152
	isolated	6–6		0.05, 0.5	1.7		154
Au(111)	layer	5–6	-1.7	1.0	2.2	2.7	155
	layer		-1.8	0.8	2.2	2.6	158
	single	6–6	-1.8	0.9	2.2	2.7	132
	single	6–6	-1.7	1.1		2.8	142
	island	6–6	-1.7	0.7	1.8	2.4	142
Au(887)	0.5 ML		-1.77	0.91	2.15	2.68	156
	1.0 ML		-1.89	0.82	2.02	2.71	156

Sample	Type	Orientation	V_{HOMO} (V)	V_{LUMO} (V)	V_{LUMO+1} (V)	Υ (V)	Ref.
Cu(100)	layer	all	-1.9	0.4	1.8	2.3	138
Cu(110)	layer	5–6	-1.75	0.2	1.5	1.95	157,158
Cu(111)	layer	6^{u}	-1.65	0.19, 0.77	1.66	1.84	153
	layer	6^{l}	-1.65	0.19, 0.77	1.50	1.84	153
	single	6	-1.9	0.8	1.5	2.7	160
	layer	6	-1.8	0.1	1.4	1.9	132
Pb(111)	layer		-1.9	0.2, 0.45	1.55, 1.7	2.1	158

Table A.2. Compilation of previously reported G^{∂} peak positions.

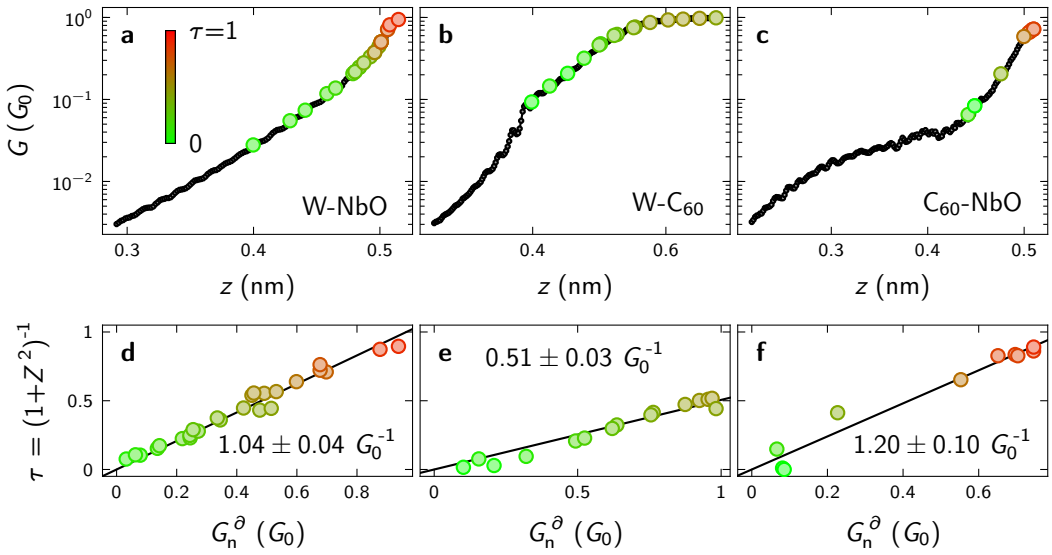

Figure A.4. Conductance-versus-distance data depicting the transition from tunneling to contact. **a-c**, Conductance (black) for W-NbO (**a**), C_{60}-NbO (**b**), and W-C_{60} (**c**) contacts as a function of tip displacement z. The feedback loop was disabled at 0.1 V, 0.1 nA. **d-f**, BTK transmission τ as a function of normal-state differential conductance $G_n^{\partial} = G^{\partial}(|eV| \gg \Delta)$ (colored circles). The black line depicts a linear fit crossing ($G_n^{\partial} = 0, \tau = 0$) with the slope indicated in each panel. Colored circles in **a-c** correspond to those shown in **d-f**. The color of the circles depicts the value of the BTK transmission τ according to the color scale on the top left of **a**.

A.3. Vertical Force Spectroscopy of Single-C_{60} Contacts

The evolution of the contact potential as a function of measurement time is presented in Fig. A.5. The vertical dash line indicates the only time, field emission on Cu(111) was performed. Between data points, indentations of ∼1–5 nm into the substrate as well as soft contacts resulting in the transfer of single atoms are small cluster from tip to surface or surface to tip were carried out. While the former most likely results in coating of the tip with substrate material, the latter predominantly leads to a removal of matter from the tip apex. The data evidences the impact of *in-situ* tip preparation on the contact potential V_{cp}. V_{cp} is influenced by the chemical composition as well as the microscopic tip geometry, both of which are modified by indentations and soft contacts. Here, field emission did not significantly impact V_{cp}. Most likely, no considerable modification of the tip geometry and chemical composition of the apex occurred.

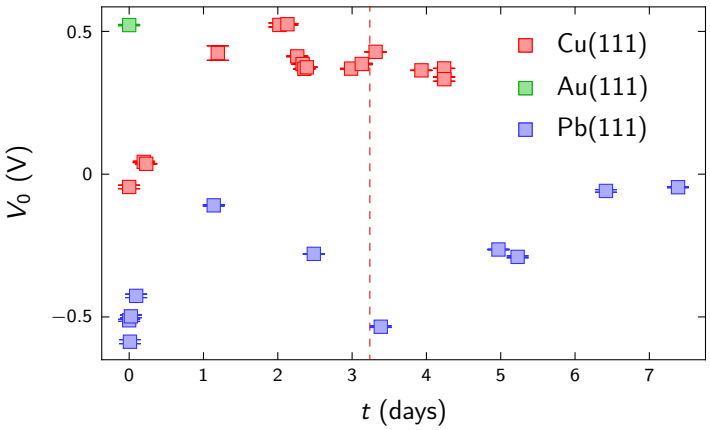

Figure A.5. Evolution of the contact potential V_0 inferred from quadratic fits to Δf (V) data as a function of measurement time for tip $\mathfrak{B}$. The dashed vertical line indicates field emission on Cu(111) relevant for the Cu(111) data.

In total, 15 data sets of C_{60}–C_{60} contacts on Cu(111) were obtained. In order to quantitatively characterize the data, additional variables were calculated for each set. $\hat{G}_c$ denotes the mean conductance at contact $G_c = G(z = z_c)$. Since the transmission factor for electron tunneling increases rapidly for $V \gtrsim 0.5\,\mathrm{V}$, only data obtained at voltages $V \leqslant 0.5\,\mathrm{V}$ were included in the calculation of $\hat{G}_c$ thus enabling the comparison of data sets obtained within different bias ranges.

$$\hat{G}_c := \langle G(z = z_c,\, V \leqslant 0.5\,\mathrm{V}) \rangle \tag{A.1}$$

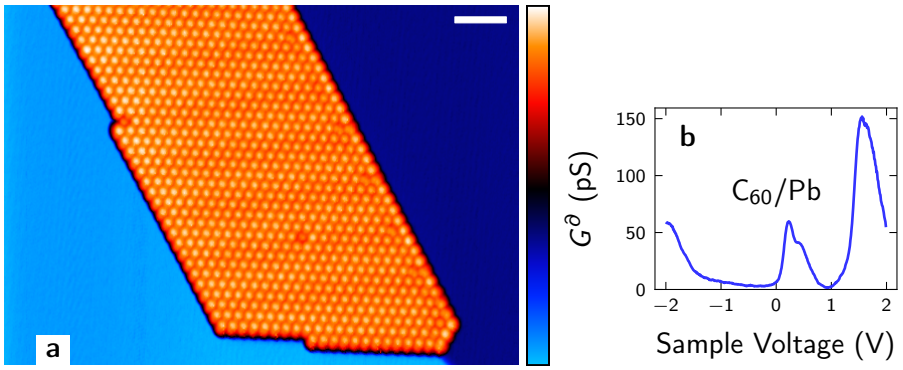

Figure A.6. **a**, Constant-current topography of C_{60}/Pb(111) acquired at 2 V, 0.1 nA. Scale bar: 5 nm. **b**, Differential conductance of a C_{60} on Pb(111). The feedback loop was opened at 2 V, 0.1 nA prior to spectroscopy. A Lock-In modulation $V_m = 5\,\mathrm{mV_{RMS}}$ was applied.

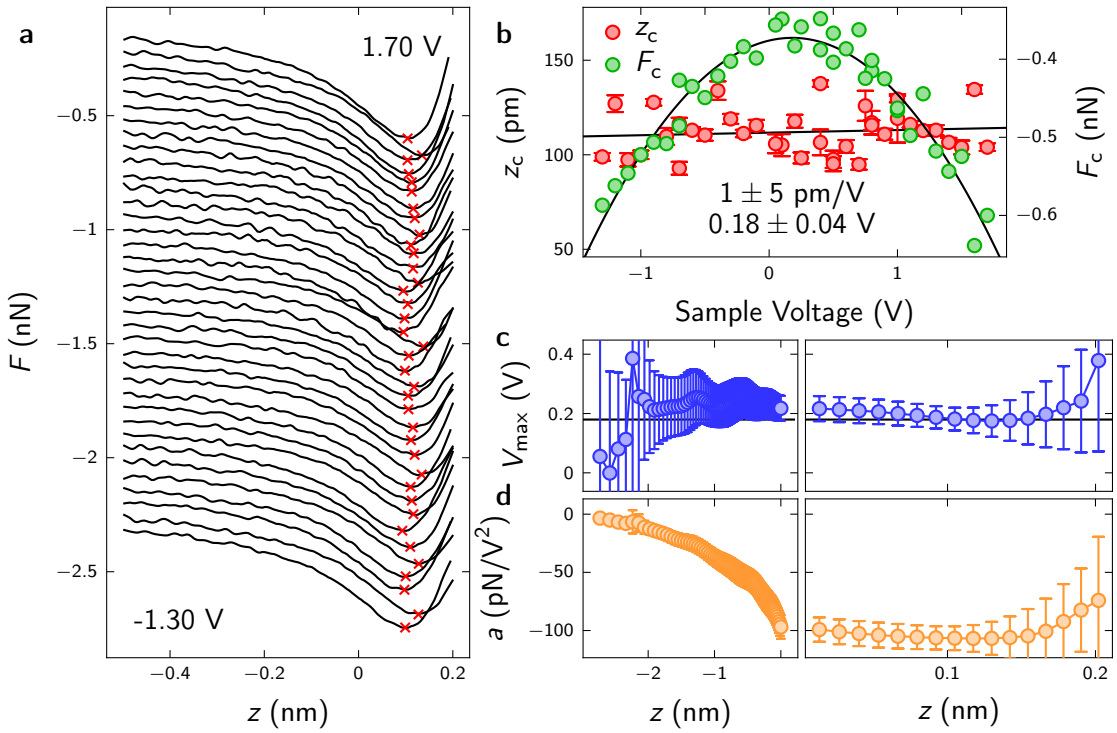

Figure A.7. Force spectroscopy for a C_{60}-C_{60} contact on Cu(111) analogous to Fig. 5.3. $z = 0$ corresponds to 0.1 V, 0.1 nA.

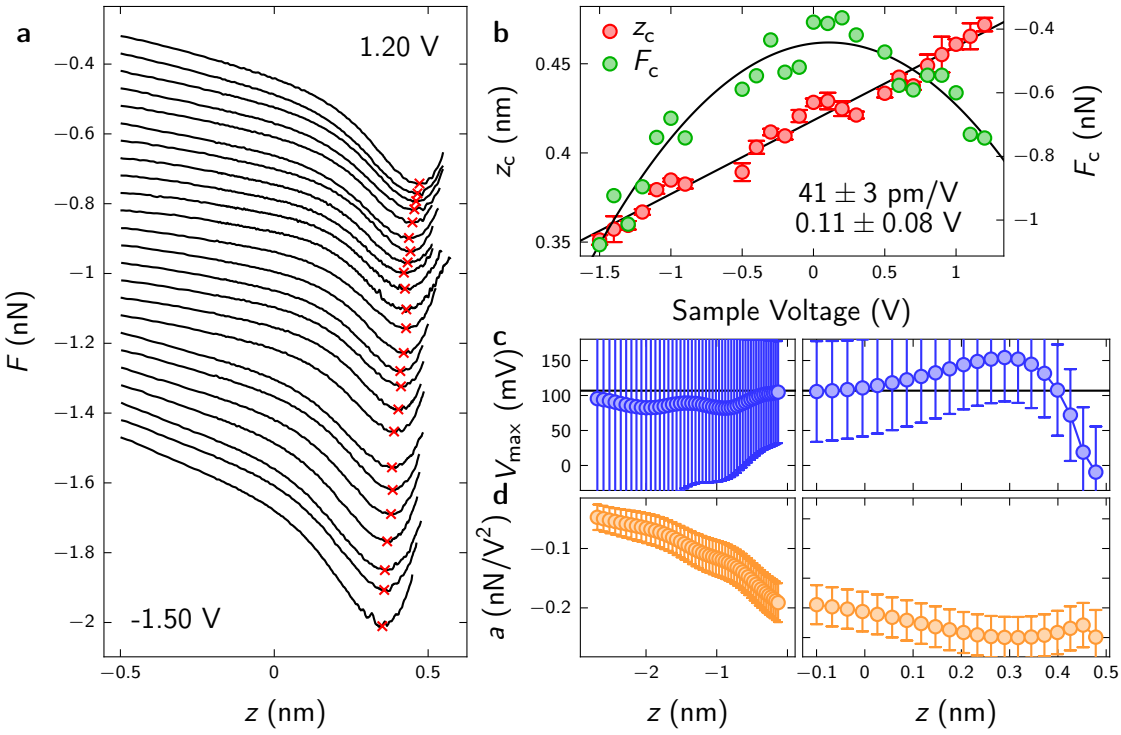

Figure A.8. Force spectroscopy for a metal-C_{60} contact on Pb(111) analogous to Fig. 5.3. $z = 0$ corresponds to 0.1 V, 0.1 nA.

Moreover, fits to $F_c\,(V)$ data were performed using the equation

$$F_c(V) = \hat{a} \cdot (V - V_{c,max})^2 + F_{c,max} \tag{A.2}$$

for each data set. The quantity $F_{c,max}$ represents a measure of the bias-independent background force. In the conventional picture, i.e., considering only van-der-Waals, electrostatic, and Pauli interaction, $V_{c,max}$ is equal to the contact potential difference. $\hat{G}_c$, $F_{c,max}$, $V_{c,max}$, and $\partial_V z_c$ are related to each other in Fig. A.9.

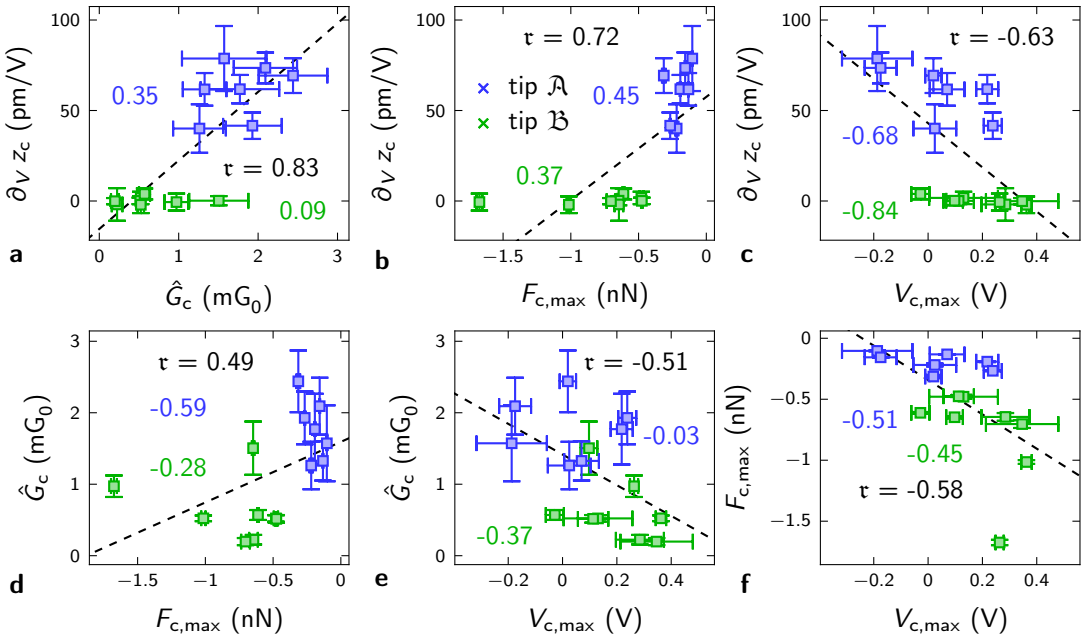

Figure A.9. Evaluation of force spectroscopy data for 15 C_{60}-C_{60} contacts on Cu(111). $\partial_V z_c$ denotes the linear slope of $z_c(V)$. $\hat{G}_c$ is the average conductance at contact, G_c, for $|V| \leqslant 0.5\,V$. The F_c (V) parabola has a maximum $F_{c,max}$ at $V_{c,max}$. The correlation coefficients $\mathfrak{r}$ are indicated in each panel. Partial correlation coefficients $\mathfrak{r}$ for each tip are given with the corresponding color. The black dashed lines are linear fits to the data acting as guides to the eye.

Tip	Contact	Sample		
$\mathfrak{A}$	C_{60}-C_{60}	Cu(111)	$\oplus$	Fig. 5.3
	M-C_{60}	Pb(111)	$\oplus$	Fig. A.8
$\mathfrak{B}$	C_{60}-C_{60}	Cu(111)	$\ominus$	Fig. A.7
	M-C_{60}	Cu(111)	$\oplus$	
	M-C_{60}	Cu(111)	$\ominus$	

Table A.3. Compilation of the observed behavior of tips $\mathfrak{A}$ and $\mathfrak{B}$ for different contacts.

Variables		$\mathfrak{r}$ all	$\mathfrak{r}$ tip $\mathfrak{A}$	$\mathfrak{r}$ tip $\mathfrak{B}$
$\hat{G}_c$	$\partial_V z_c$	+0.83	+0.35	+0.09
$F_{c,max}$	$\partial_V z_c$	+0.72	+0.45	+0.37
$V_{c,max}$	$\partial_V z_c$	−0.63	−0.68	−0.84
$F_{c,max}$	$\hat{G}_c$	+0.49	−0.59	−0.28
$V_{c,max}$	$\hat{G}_c$	−0.51	−0.03	−0.37
$V_{c,max}$	$F_{c,max}$	−0.58	−0.51	−0.45

Table A.4. Correlation coefficients for the data shown in Fig. A.9.

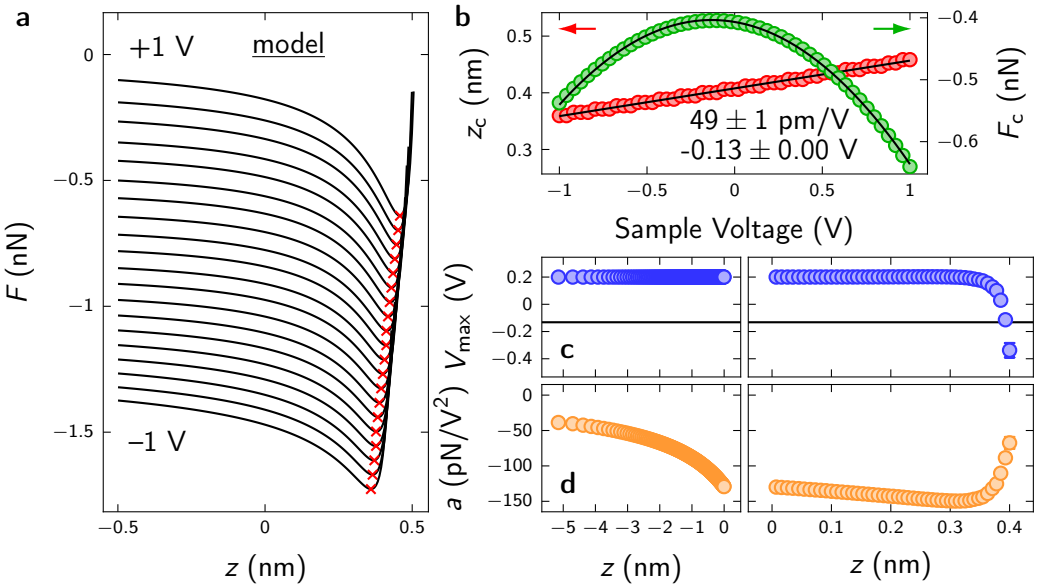

Figure A.10. Evaluation of force data obtained from a simple model calculation using analytic expressions for van-der-Waals, Lennard-Jones, and electrostatic forces analogous to Fig. 5.3. Model parameters are $\mathscr{H} = 0.2\,\mathrm{eV}$, $\varepsilon = 2.5\,\mathrm{meV}$, $V_{\mathrm{cp}} = 0.2\,\mathrm{V}$, $z_{\mathrm{eq}} = 0.4\,\mathrm{nm}$, $r_{\mathrm{t}} = 10\,\mathrm{nm}$, and $\alpha = 40\,\mathrm{pm/V}$.

A.4. Lateral Force Spectroscopy of Single Atoms

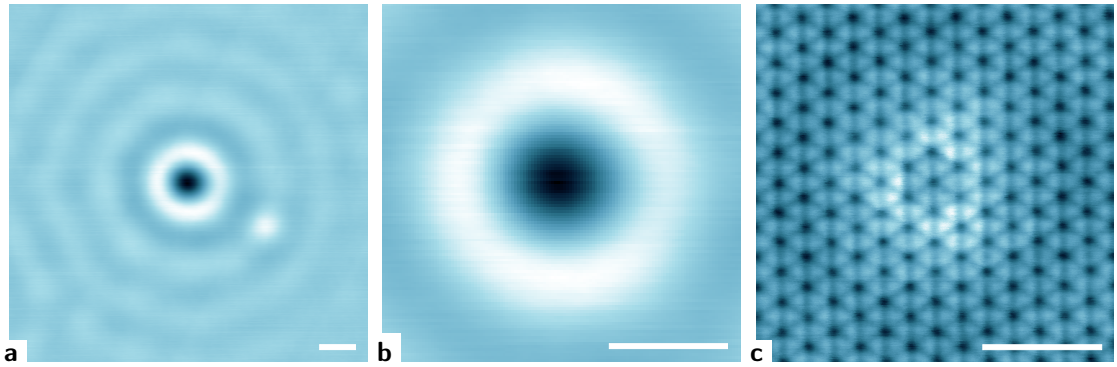

Figure A.11. Bulk atomic defect on Cu(111). **a,b**, Constant-current STM topography obtained in the tunneling regime (91 mV, 32 pA). **c**, Atomic resolution image (2 mV, 85 nA) acquired by dragging a single Cu atom across the atomic defect shown in **a,b**. Scale bars: 1 nm.

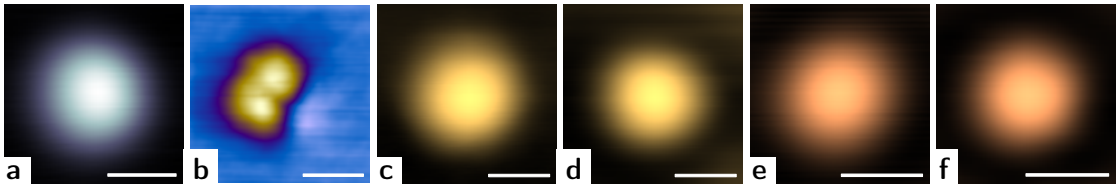

Figure A.12. Constant-current topography of **a**, Pb/Pb(111), **b**, a signature observed after Co evaporation on Pb(111), **c**, Au/Au(111), **d**, Co/Au(111), **e**, Cu/Cu(111), and **f**, Co/Cu(111). Imaging parameters are **a**, 0.1 V, 53 pA, **b**, 2 mV, 0.1 nA, **c**, 0.1 V, 52 pA, **d**, 52 mV, 52 pA, **e**, 0.1 V, 52 pA, and **f**, 0.1 V, 84 pA. Scale bars: 0.5 nm.

After evaporation of Co onto the Pb(111) substrate at 6 K, distinct topographic signatures were observed (Fig. A.12 **b**). At voltages $\leq$100 mV, a triangular structural motif consisting of a 33$\pm$2 pm high double protrusion accompanied by a 4$\pm$1 pm deep depression is visible (Fig. A.13 **a-e**). At higher bias, only a single [18, 33] pm high protrusion appears next to the depression (Fig. A.13 **f**). The orientation of the triangle can be switched by lateral manipulation. Its edges are exclusively oriented along $\langle 1\,1\,\bar{2}\rangle$. Co-derived entities on Pb(111) exhibit a lateral stability comparable to single Pb atoms in conjunction with enhanced electronic noise (cf. Fig. A.14 **a,b**). No electronic signatures are observed between $\pm$2 V (Fig. A.14), except for the superconducting energy gap at zero voltage (Fig. A.14 **a**).

The observations are not characteristic of single metal atoms adsorbed to a metal. A possible explanation consists of the formation of cobalt hydrides CoH_x formed using H_2 molecules present in the residual gas. Previously, the spontaneous formation of CoH on Ag(111) was observed at temperatures as low as 5 K (ref. 316). The presence of one or more flexibly bonded and hence fluctuating H atoms might explain the enhanced current noise occurring at Co-derived entities on Pb(111) compared to Pb/Pb(111) and the pristine surface. STM imaging of CoH_3/Ag exhibits three depressions separated symmetrically by 120° caused by H atoms vertically located between the surface plane and the Co atom[316]. H/Cu(001) and H/Pd(111) likewise appear as depression[317,318]. Conductance fluctuations observed in a break junction experiment were

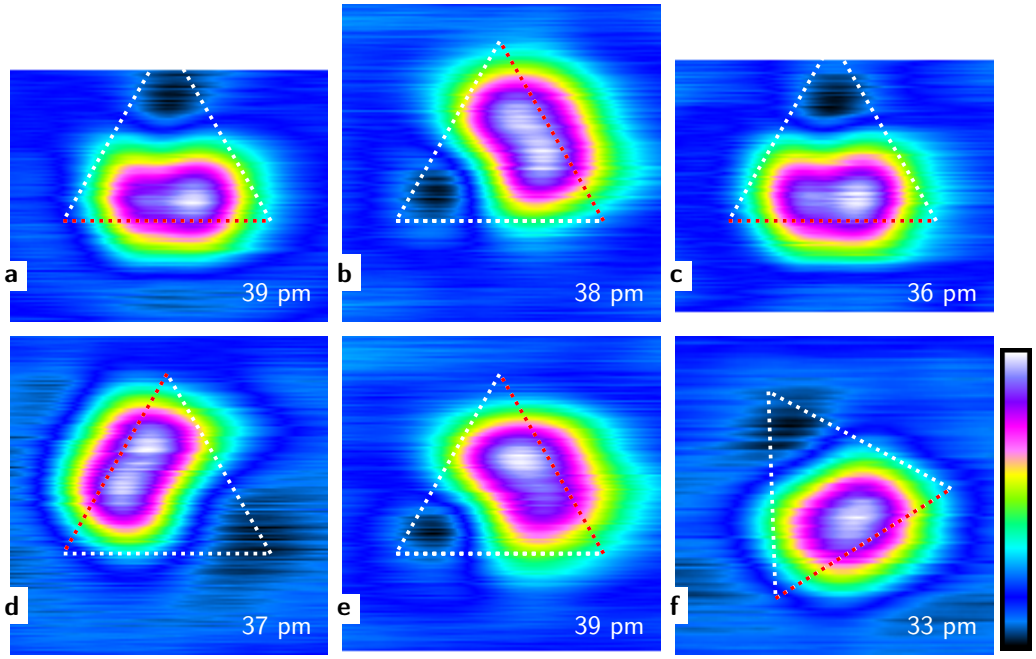

Figure A.13. Topographic signatures observed after Co evaporation on Pb(111). Scan parameters are **a**-**e**, 2 mV, 0.1 nA, and **f**, 0.1 V, 50 pA. The height of the color scale is indicated at the bottom right of each image. The image width is 1.6 nm. Triangles are guides to the eye. The rotated triangle of **f** reflects the different scan direction compared to **a**-**e**. Between **a**-**e**, lateral manipulation yielded rotation of the topographic features. While at low voltage (**a**-**e**) a double protrusion is visible, only a single protrusion appears at higher bias (**f**).

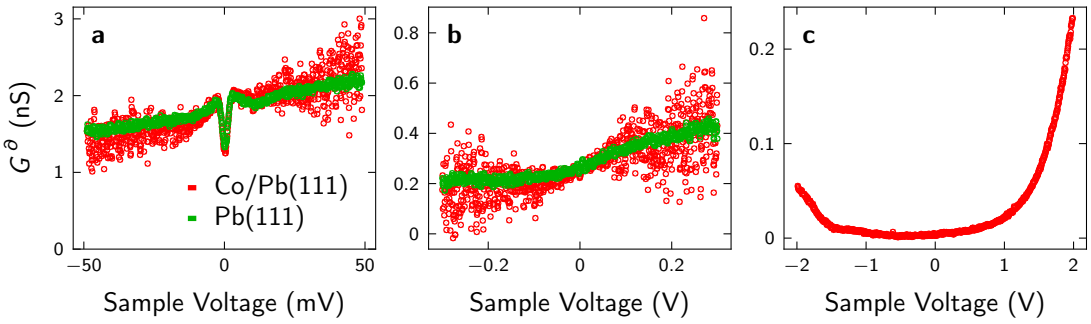

Figure A.14. Differential conductance acquired atop a Co-derived entity on Pb(111) (red, cf. Fig. A.13) and comparison to the pristine Pb(111) surface (green). The feedback loop was opened at 0.1 nA and **a**, 50 mV, **b**, 0.3 V, and **c**, 2 V prior to data acquisition. A modulation voltage of 150 μV_{RMS} (**a**), 1 mV_{RMS} (**b**), and 5 mV_{RMS} (**c**) was applied during spectroscopy. Enhanced noise is visible for data of Co-derived entities. Except for the superconducting energy gap at $V = 0$, no electronic feature is visible.

assigned to the presence of H_2 bonding to the Pt electrodes[319].

For the present data, the most intuitive explanation consists of the formation of a Co_2H_n cluster, where the two Co atoms are responsible for the two protrusions while hydrogen vertically located between the Co atoms and the surface plane causes the single depression due to a local reduction of the conductivity. The difference of the full width at half maximum in the direction parallel to both protrusions (845 ± 3 pm) and perpendicular to it (656 ± 5 pm) amounts to 190 ± 9 pm. The

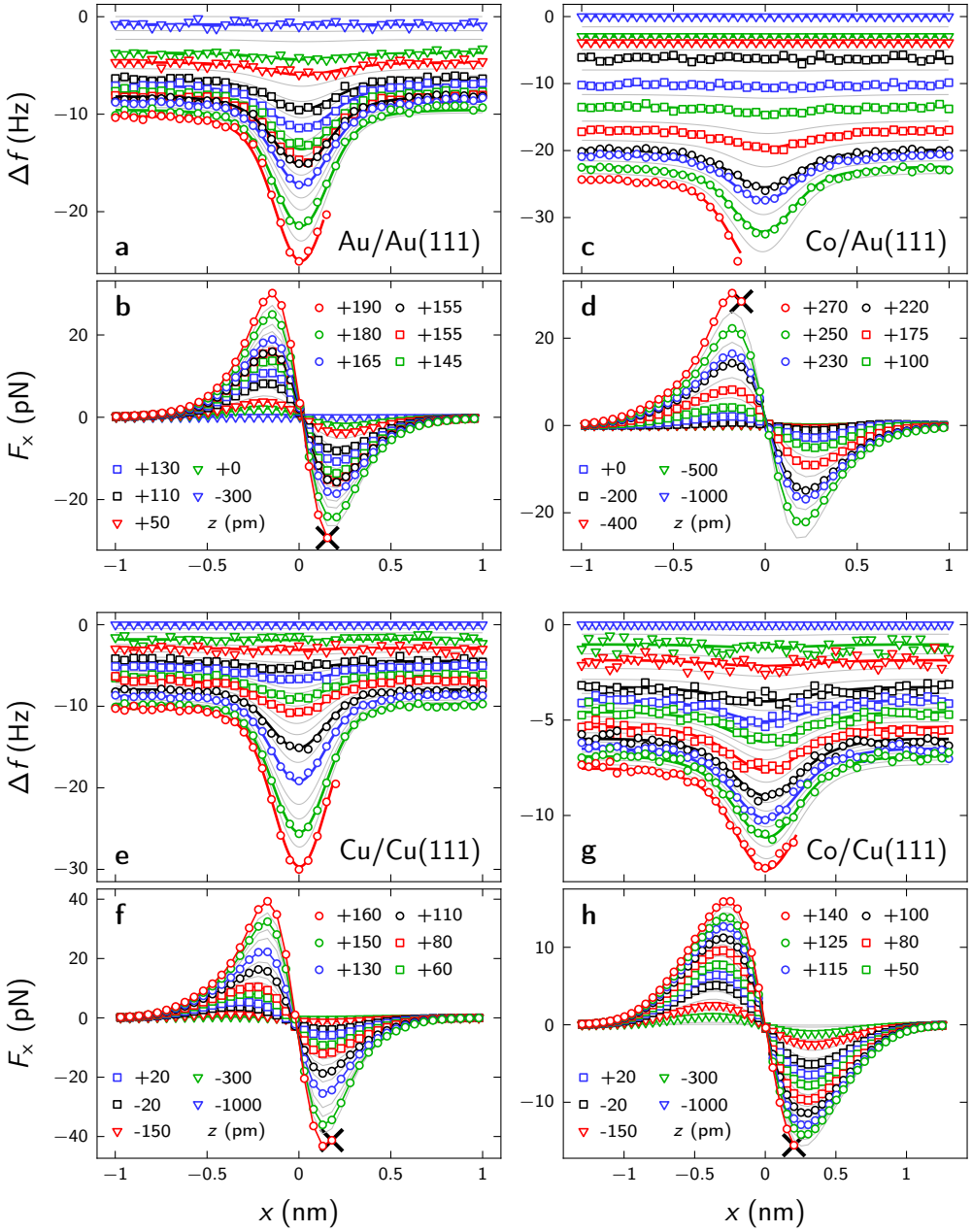

Figure A.15. **a,c,e,g**, Δf and **b,d,f,h**, F_x for **a,b** Au/Au(111), **c,d** Co/Au(111), **e,f** Cu/Cu(111), and **g,h** Co/Cu(111). Markers and colors are consistent with Fig. 6.6. The data were obtained at 6.1 K (**a,c**), 7.4 K (**e**), and 6.7 K (**g**). $z = 0$ corresponds to 50 mV, 0.1 nA (**a,b**), 0.1 V, 50 pA (**c,d**), and 10 mV, 0.1 nA (**e-h**).

value is close to the fcc-hcp distance of Pb(111) (202 pm) indicating Co occupation of adjacent fcc and hcp sites. A higher mobility of single Co compared to Pb atoms is required for the observed exclusive occurrence of presumed Co clusters.

Previously, a bi-lobed structural motif was observed for CoH_2 on Pt(111)[320] and on graphene on Pt(111)[321]. However, a distribution of $CoH_{[0,3]}$ occurred featuring distinct topographic signatures for each species. The application of voltage pulses of 150, 180, and 450 mV allowed a successive dehydrogenation. In the present experiments, only a single type occurred. Voltage pulses did not transform the topographic features but resulted in jumps to adjacent binding sites. Recently,

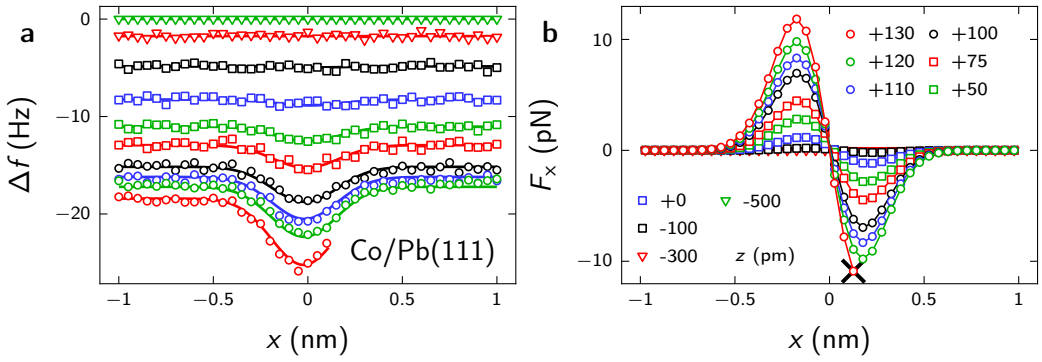

Figure A.16. **a**, Δf and **b**, F_x for a Co-derived entity Pb(111) at $T = 5.8\,\mathrm{K}$. Markers and colors are consistent with Fig. 6.6. $z = 0$ corresponds to 2 mV, 0.1 nA.

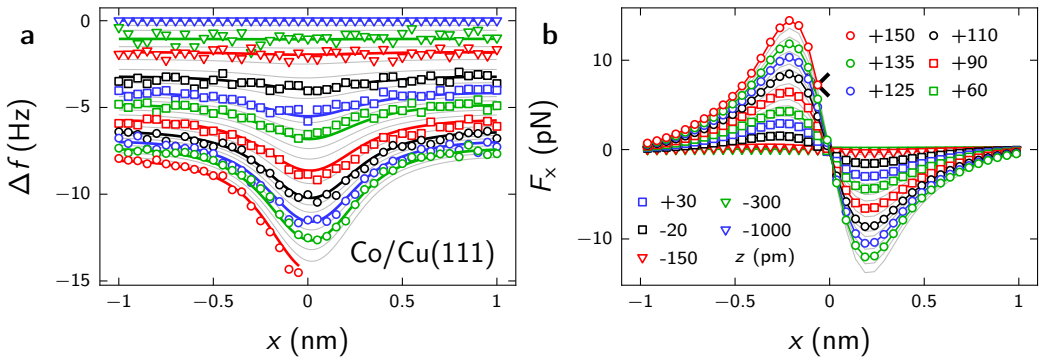

Figure A.17. **a**, Δf and **b**, F_x for Co/Cu(111) at $T = 6.0\,\mathrm{K}$. Markers and colors are consistent with Fig. 6.6. $z = 0$ corresponds to 10 mV, 0.1 nA. Here, the atom moves at $F_x^{\rightarrow} = -7.2\,\mathrm{pN}$, which is only half of the maximum $\max|F_x| = 14.4\,\mathrm{pN}$. The data evidence the stochastical nature of the manipulation process. The maximum $\max|F_x| = 14.4\,\mathrm{pN}$ is consistent with temperature-dependence of the threshold manipulation force for Co/Cu(111), $F_x^{\rightarrow}$, presented in Fig. 6.7 **a**.

single Co atoms deposited on black phosphorus exhibited a similar bi-lobed structural motif[322] without accompanying depression. Adsorption of hydrogen increased with time and destroyed the bi-lobed feature which was not observed in the present experiments.

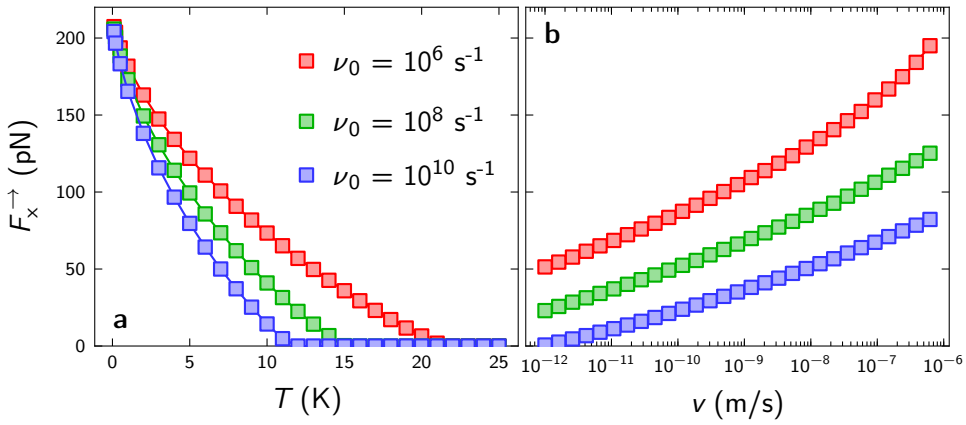

Figure A.18. Lateral forces evaluated within the lateral force model. Input parameters are $a_{s,t} = 200\,\mathrm{pm}$, $U_{s,0} = 20\,\mathrm{meV}$, **a**, $v = 20\,\mathrm{pm/s}$, and **b**, $T = 10\,\mathrm{K}$. Different attempt frequencies $\nu_0 \in [10^6, 10^8, 10^{10}]\,\mathrm{s}^{-1}$ were employed and colored according to the description in **a**.

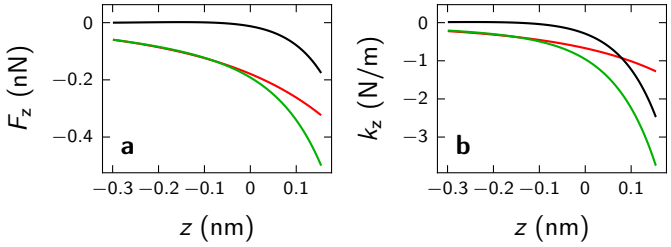

Figure A.19. **a**, Vertical force and **b**, corresponding vertical stiffness k_z recovered from lateral force spectroscopy data of Cu/Cu(111). Green and red data correspond to the Cu(111) substrate (background) and the center of the Cu adatom, respectively. Black represents the background-subtracted data at the center of the Cu adatom.

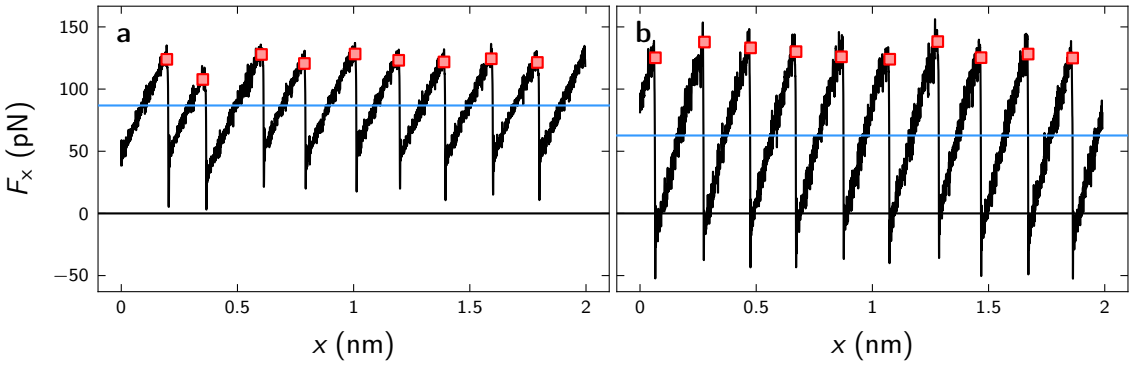

Figure A.20. Results of the numerical implementation of the PT model, using a modified version of a previously published algorithm[305]. The lateral force F_x is presented as a function of the lateral position x of the top electrode (black). Model parameters are $a = 200\,\text{pm}$, $U = 0.1\,\text{eV}$, $m = 10^{-12}\,\text{kg}$, $v = 10^{-6}\,\text{m/s}$, $T = 10\,\text{K}$, $k = 0.5\,\text{N/m}$ (**a**), and $k = 1\,\text{N/m}$ (**b**). The modified spring constant reduces the mean lateral force (blue dashed line) from $\langle F_x \rangle = 87\,\text{pN}$ (**a**) to $\langle F_x \rangle = 63\,\text{pN}$ (**b**), while the maximum force prior to each manipulation event (red squares) increases from $F_x^{\rightarrow} = 122 \pm 6\,\text{pN}$ (**a**) to $F_x^{\rightarrow} = 129 \pm 5\,\text{pN}$ (**b**). These values represent mean and standard deviation of the squares shown in **a** and **b**. $F_x^{\rightarrow}$ is estimated as average of F_x within 30 pm prior to the manipulation. These data highlight the sensitivity of the ratio between $\langle F_x \rangle$ and $F_x^{\rightarrow}$ on the system parameters.

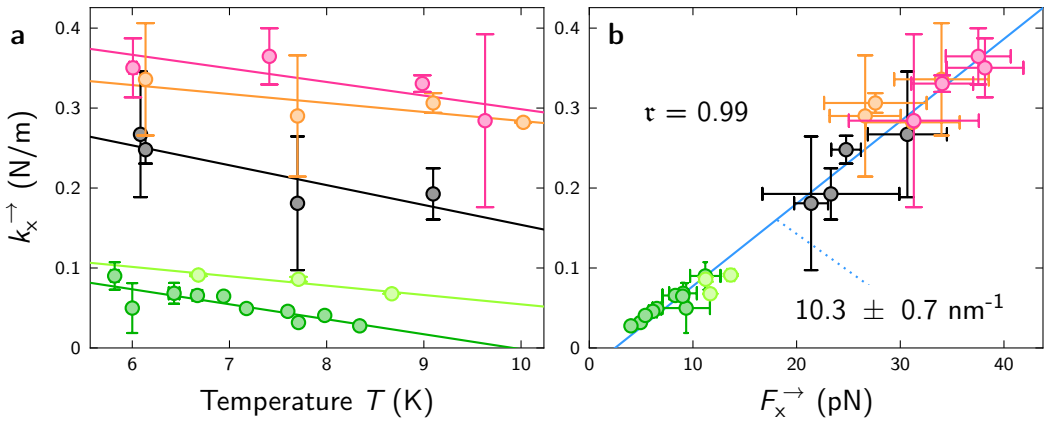

Figure A.21. **a**, Temperature-dependence of the lateral spring constant at the manipulation threshold $k_x^{\rightarrow} = \partial_x F_x(x = 0, z = z^{\rightarrow})$. **b**, $k_x^{\rightarrow}$ as a function of the threshold manipulation force. The blue line represents a linear fit of slope $10.3 \pm 0.7\,\mathrm{nm}^{-1}$. The correlation coefficient amounts to $\mathfrak{r} = 0.99$.

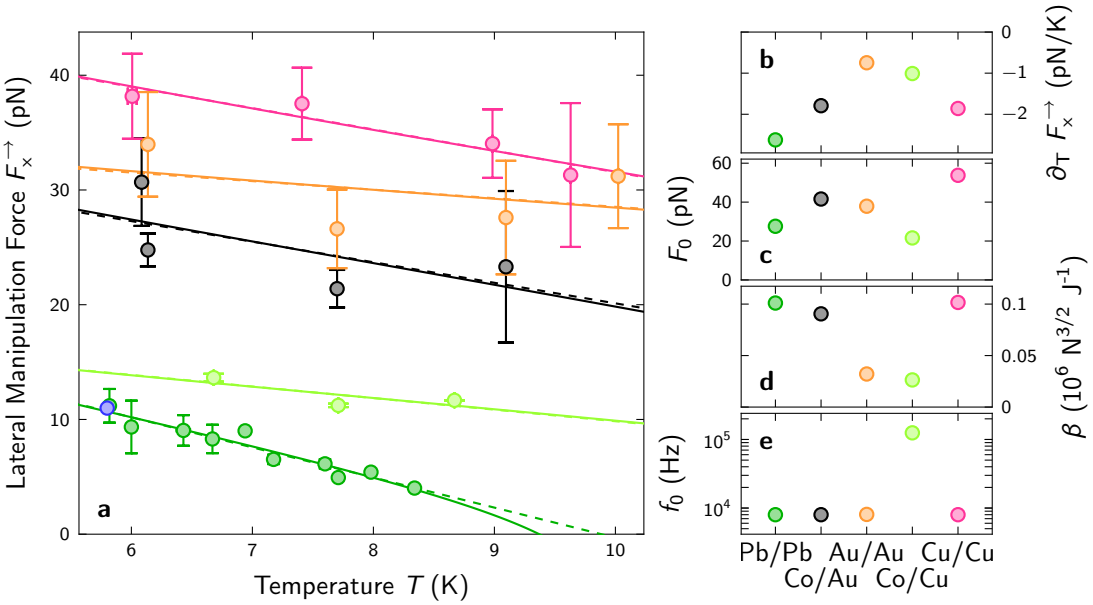

Figure A.22. Evaluation of the fit of the prediction of the mean lateral force of the PT model, $\langle F_x \rangle$, to the experimental $F_x^{\rightarrow}$ data. **a**, Experimental $F_x^{\rightarrow}$ data (circles) as a function of temperature T. Circles and error bars represent mean value and standard deviation of the data for each T Solid lines denote fits to $\langle F_x \rangle$ within the PT model, dashed lines are linear fits. **b**, Linear slope of $F_x^{\rightarrow}(T)$. The analytic expression at the basis of the fit is $\langle F_x \rangle = F_0 - [\beta k_B T \ln(v_c/v_x)]^{2/3}$ with $v_c = (2 f_0 \beta k_B T)/(3k\sqrt{F_0})$ (ref. 297,300,323). F_0 - friction force at 0 K. v_x - manipulation velocity. f_0 - attempt frequency. k - spring constant between probe and top electrode. β - corrugation parameter, equal to the curvature of U for a sinusoidal potential U. Since the threshold manipulation force $F_x^{\rightarrow}$ decreases with increasing temperature (cf. Fig. 6.7 **a,b**), the z value and consequently the spring constant between tip and atom at the manipulation threshold decreases (cf. Fig. A.19). Hence, the temperature-dependent lateral spring constants at the manipulation threshold $k_x^{\rightarrow}$ obtained experimentally (Fig. A.21) were used for k in the PT fit. **c-e**, Fit parameters F_0 (**c**), β (**d**), and f_0 (**e**).